Modeling and Simulations of Molybdenum Diselenide ($MoSe_2$) Phototransistors

by

Gyu Chull Han

A thesis
presented to the University of Waterloo
in fulfillment of the
thesis requirement for the degree of
Doctor of Philosophy
in
Electrical and Computer Engineering - Nanotechnology

Waterloo, Ontario, Canada, 2019

Examining Committee Membership

The following served on the Examining Committee for this thesis. The decision of the Examining Committee is by majority vote.

External Examiner:	Dr. Gap Soo Chang Professor, Dept. of Physics and Engineering Physics University of Saskatchewan
Supervisor:	Dr. Youngki Yoon Associate Professor, Dept. of Electrical and Computer Engineering University of Waterloo
Internal Member:	Dr. Zbig Wasilewski Professor, Dept. of Electrical and Computer Engineering University of Waterloo
Internal Member:	Dr. Irene A. Goldthorpe Associate Professor, Dept. of Electrical and Computer Engineering University of Waterloo
Internal-external Member:	Dr. Ting Tsui Professor, Dept. of Chemical Engineering University of Waterloo

Author's Declaration

This thesis consists of material all of which I authored or co-authored: see Statement of Contributions included in the thesis. This is a true copy of the thesis, including any required final revisions, as accepted by my examiners.

I understand that my thesis may be made electronically available to the public.

Statement of Contributions

The material in Chapter 3 is published in the following with the permission of Nature Publishing Group:

Reference: Chulseung Jung, Seung Min Kim, Hyunseong Moon, Gyuchull Han, Junyeon Kwon, Young Ki Hong, Inturu Omkaram, Youngki Yoon, Sunkook Kim, Jozeph Park, "Highly Crystalline CVD-grown Multilayer $MoSe_2$ Thin Film Transistor for Fast Photodetector," *Scientific Reports*, vol. 5, pp. 15313, 2015. doi: 10.1038/srep15313. URL https://www.nature.com/articles/srep15313

Contributions: S. K. and J. P. designed the experiments. C. J., H. M., Y. K. H., J. P. and S. K. synthesized $MoSe_2$ film and fabricated the devices, and S. M. K., J. K. and I. O. characterized the quality of $MoSe_2$ film, and G. H. and Y. Y. conducted the theoretical analysis. S. K., C. J., S. M. K., Y. Y. and J. P. wrote the manuscript. All authors reviewed the manuscript. C. J., H. M. and S. M. K. contributed equally to this work.

The material in Chapter 4 is published in the following with the permission of Wiley Publishing:

Reference: Sunkook Kim, Jesse Maassen, Jiyoul Lee, Seung Min Kim, Gyuchull Han, Junyeon Kwon, Seongin Hong, Jozeph Park, Na Liu, Yun Chang Park, Inturu Omkaram, Jong Soo Rhyee, Young Ki Hong, and Youngki Yoon, "Interstitial Mo-Assisted Photovoltaic Effect in Multilayer $MoSe_2$ Phototransistors," *Advanced Materials*, vol. 30, pp. 1705542, 2018. doi: 10.1002/adma.201705542. URL https://onlinelibrary.wiley.com/doi/full/10.1002/adma.201705542

Contributions: S. K., J. K., S. H., J. P., N. L., I. O., and Y. K. H. provided experimental fabrication, measurements, and characterizations. G. H. and Y. Y. provided analytical modeling and fitting to experimental results. J. M. provided material simulations. S.K., J. M., J. L., G. H., and Y. Y., wrote and edited the paper. All authors discussed the results and commented on the manuscript at all stages.

Abstract

Since the first demonstration of graphene, two-dimensional (2D) materials have attracted gigantic attentions from the electronic device community. Various 2D materials showing metallic, semiconducting, and insulating properties have been reported. Among them, transition metal dichalcogenide (TMDs) is one of the most latent 2D materials, having excellent semiconducting properties with electronical, optical, and mechanical advantages. Due to their intriguing properties, TMD devices have been investigated for various applications such as switching devices or sensing applications. In particular, 2D TMD phototransistors exhibit high optical device performance, demonstrating their potential for future wearable devices and health monitoring systems.

In this thesis, to investigate optical properties of the 2D TMDs phototransistors, comprehensive theoretical studies are performed based on analytical modeling and numerical simulation. I introduce overall simulation schemes showing self-consistent iterative calculations between transport and electrostatics. Non-equilibrium Green's function (NEGF) transport method is mainly used for device simulations in this study. I discuss two major methods to calculate electronic states of channel materials in the devices: effective mass and tight-binding approximations. I develop new method, modified effective mass approximation, for maintaining rigorous calculation and having low computational cost. Following that, the Poisson's equation solver is presented to calculate electrostatics.

I first analyze unique device performance of fabricated 2D TMDs phototransistors. To confirm origin of uncommon *p*-type behavior and large photoresponsivity of chemical vapor deposition (CVD) grown multilayer $MoSe_2$ phototransistors, density-of-states in the band gap is extracted by temperature-dependent analysis. Next, physical models for optical behaviors of $MoSe_2$ phototransistors under illumination are developed, considering two key mechanisms: photoconductive (PC) and photogating (PG) effects. The models are used to analyze large photoresponsivity of multilayer $MoSe_2$ phototransistors fabricated by CVD under Mo-rich condition, where it turns out that observed Mo interstitials on the materials are critical factor of large optical response. Then, the $MoSe_2$ phototransistor is computationally simulated based on NEGF method with trap models. PG effect is deeply examined from the microscopic perspectives. I also simulate optical device performance such as photoresponsivity and detectivity. After that, for further improvement of the device performance, dependence of photoresponsivity on material properties is investigated.

The simulation methods can be extended to other phototransistors based on new materials to strengthen the photoresponsivity or PG effect. A phototransistor with hexagonal nano-patterned multilayer MoS_2 as channel layer is simulated to scrutinize high photoresponsivity of it. Material and device simulations are carried on to specify energy level of a trap state mainly contributing to the large photogain. We study dependence of photocurrent on energy level of trap states with realistic capture cross sections.

Overall, $MoSe_2$ phototransistors are physically modeled and numerically simulated. Those trends of models and simulation results successfully reproduce those by experiments, providing in-depth understanding of underlying photoillumination effects. The proposed modeling and simulators can not only accurately predict the photoelectric performances of the future 2D phototransistors but also deeply quantify and analyze the internal physical mechanisms, providing a useful framework for the improvement and optimal design of popular 2D phototransistors for a wide range of applications.

Acknowledgements

My unreserved gratitude and praises are for God, the most gracious and the most merciful. He has blessed me with his bounties, and he has given me the strength and courage to reach my goals during the course of this research.

I would like to express my deepest and sincerest gratitude to my supervisor, Professor Youngki Yoon, for his continuous guidance, inspiration, deep insight, invaluable advice, and support during my graduate studies at the University of Waterloo. His guidance and encouragement have inspired and motivated me throughout the completion of this thesis, and he has made my experience at our research group worthwhile and enjoyable.

I would also like to thank the examining committee members of this thesis, Professor Zbig Wasilewski, Professor Irene A. Goldthorpe, and Professor Ting Tsui. Their insightful comments have significantly improved the quality and presentation of my work. In addition, I would like to thank Professor Gap Soo Chang for serving as my thesis external examiner and for his insights on my thesis with me.

Special thanks are due to my friends and colleagues at our group for their support and kindness, and for making my stay memorable. I would like to express special gratitude to Demin Yin, AbdulAziz AlMutairi, Yiju Zhao, Hyunjae Lee, Manasa Kaniselvan, and Robert Bennett. I specially appreciate JuHyeong Ryu's support and collaboration for multiple public events in Korean Graduate Students Association.

With great appreciation, I acknowledge the scholarship and financial support from Natural Sciences and Engineering Research Council (NSERC), Ontario Student Assistance Program (OSAP), and University of Waterloo, for granting me the scholarship and giving me the opportunity to enhance my experience and education.

Finally, my greatest thanks to my devoted parents, Choonhwan Han, Wonae Lee, all of whom have constantly given me love, support, motivation, and sincere prayers. Last, but certainly not least, I would like to thank my beloved wife, Ahreum Han, for her love, patience, and continued encouragement she has provided me during my graduate study. Nothing would have been possible without God, the Creator and Lord of the universe, and my family support.

Table of Contents

List of Figures

List of Tables

Chapter 1 Introduction

1.1 2D Materials

1.1.1 Semi-metallic Graphene

Since the first reports on graphene in around 1970 [1], [2], there had not been significant scientific and engineering breakthrough in two-dimensional (2D) materials for decades until Andre Geim and Konstantin Novoselov demonstrated novel 2D nanoelectronic devices using a simple mechanical exfoliation technique [3], which evoked gigantic interests in 2D materials. Graphene has a planar structure, composed of the honeycomb shape as shown in Figure 1.1 with a carbon atom at each corner.

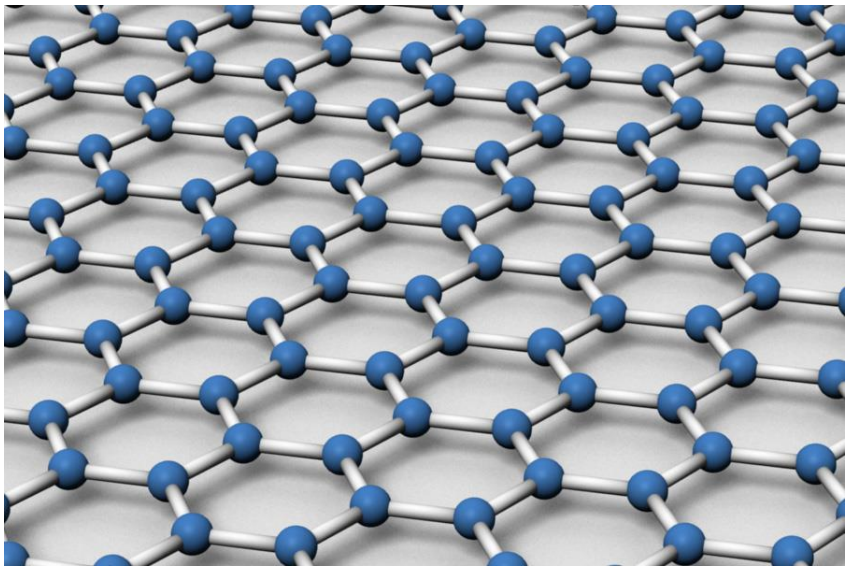

Figure 1.1 Atomistic structure of graphene [4].

This abrupt increase of interest in graphene is partly due to the possibility to grow on metal and transfer it to insulating substrates [5], [6] as well as mechanical exfoliation [3]. Epitaxial graphene on top of SiC wafers is another way to obtain graphene which is produced by thermal deposition of SiC [7], [8]. Since exfoliation is not suitable for mass production in practice, the other two methods are widely used to obtain large-scale graphene towards the fabrication of future graphene-based electronics.

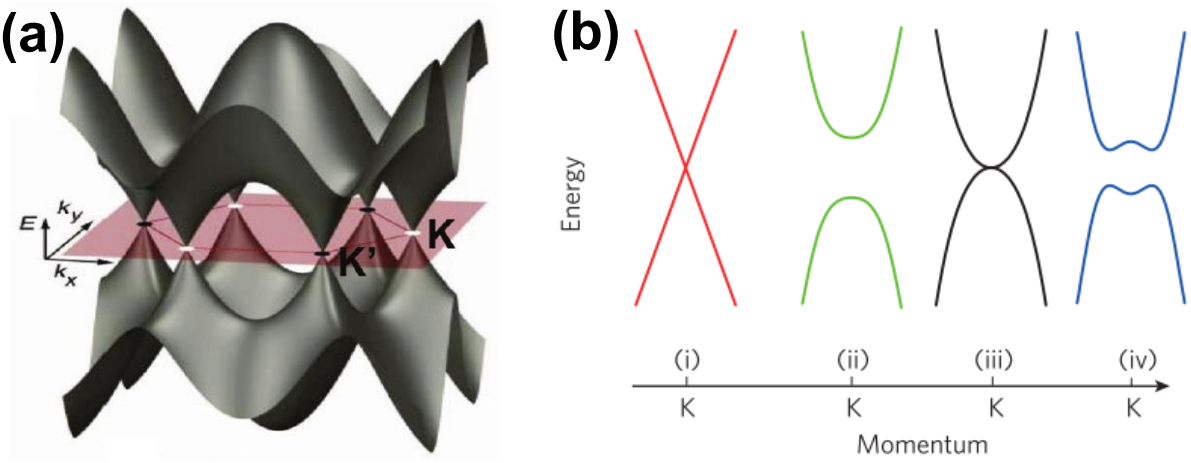

Figure 1.2 (a) Band structure of graphene. (b) Band structure at the K point of: (i) pure graphene (no band gap), (ii) graphene nanoribbons, (iii) bilayer graphene without applied field (no band gap), and (iv) bilayer graphene with an perpendicular applied field. Figures reprinted with permission from: (a) reference 9, © 2010 American Chemical Society; (b) reference 10, © 2010 Springer Nature.

These days, many high-tech companies like Samsung and Intel as well as innumerable research groups are investigating the electronical, optical, mechanical, and chemical properties of graphene for device applications. Graphene has extremely high electron mobility at room temperature, which make it very unique and attractive over other materials. Exfoliated graphene on SiO_2-covered silicon wafer gives mobility of 40,000 $cm^2/V \cdot s$ and up to 70,000 $cm^2/V \cdot s$ [11], [12]. Furthermore, graphene without charged impurities and ripples [13] and suspended graphene exhibited the mobility of 200,000 $cm^2/V \cdot s$ and 10^6 $cm^2/V \cdot s$, respectively [14].

Even with the high mobility, graphene has no band gap, which can be seen at the K point in the band structure, where valence and conduction bands meet (see Figure 1.2(b)(i)); therefore, it has semi-metallic properties. However, a non-zero band gap is required for switching applications, and several methods have been proposed to open the band gap [15]–[34]. The most common way is to create a graphene nanoribbon (GNR), which is a confined one-dimensional (1D) graphene, where the band gap is, in general, inversely proportional to the width of ribbon. However, it is practically hard to achieve a desired band gap from GNRs due to the roughness of edges and the variability of the GNR width. In addition, even with a wide band gap opening, the conduction and valence bands cannot maintain the shape of the original Dirac cone, leading to the performance degradation of graphene devices due to increase of the effective mass [35]. Another method to open a band gap is to apply vertical field across

bilayer graphene (see Figure 1.2(b)(iv)). A couple of papers reported that opening band gap by 200–250 meV was achieved using the electric field of (1–3) × 10^7 V/cm [31], [32].

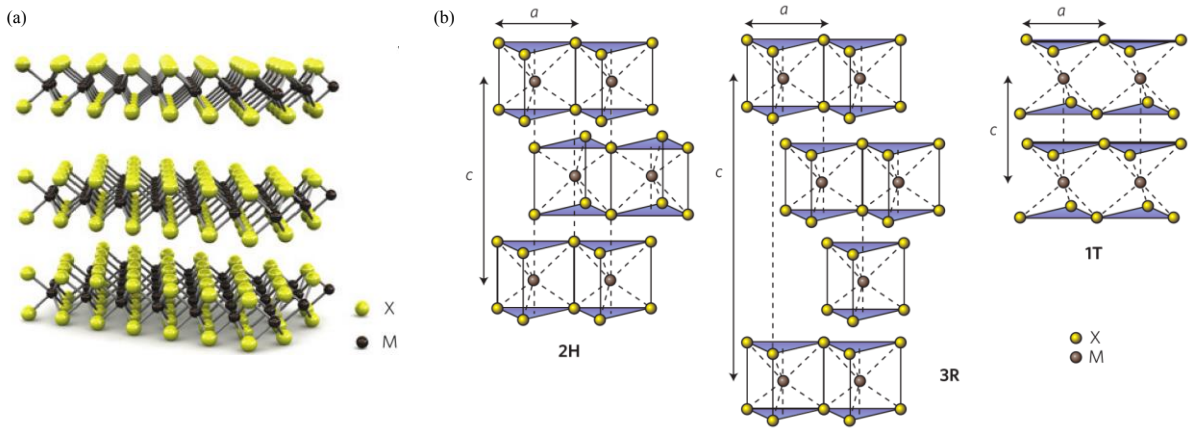

Figure 1.3 (a) Atomically schematic representation of a typical MX_2 structure, with the chalcogenide atoms (X) in yellow and the transition metal atoms (M) in grey. (b) Schematics TMDs in three different structural polytypes. Figures reprinted with permission from reference 37, © 2012 Springer Nature.

	-S_2		-Se_2		-Te_2	
	Electronic characteristics	**References**	**Electronic characteristics**	**References**	**Electronic characteristics**	**References**
Nb	Metal; superconducting; CDW	138 (E)	Metal; superconducting; CDW	138,164 (E)	Metal	83 (T)
Ta	Metal; superconducting; CDW	138,164 (E)	Metal; superconducting; CDW	138,164 (E)	Metal	83 (T)
Mo	Semiconducting 1L: 1.8 eV	31 (E)	Semiconducting 1L: 1.5 eV	82 (T)	Semiconducting 1L: 1.1 eV	82 (T)
	Bulk: 1.2 eV	88 (E)	Bulk: 1.1 eV	88 (E)	Bulk: 1.0 eV	165 (E)
W	Semiconducting 1L: 2.1 eV	25 (T)	Semiconducting 1L: 1.7 eV	83 (T)	Semiconducting 1L: 1.1 eV	83 (T)
	1L: 1.9 eV	82 (T)				
	Bulk: 1.4 eV	88 (E)	Bulk: 1.2 eV	88 (E)		

Table 1.1 Electronic characteristics of TMDs. Table reprinted with permission from reference 37, © 2012 Springer Nature.

1.1.2 2D Semiconductors

1.1.2.1 Transition Metal Dichalcogenides (TMDs)

Among many 2D materials, transition metal dichalcogenides (TMDs) are the emerging and promising materials, which have attracted a number of researchers' attention within the last decade. They have chemical forms of MX_2 where M indicates transition metal (Mo, W, Nb, Ta, Ti, or Re) and X stands for chalcogenide materials (Se, S, or Te). Each unit cell consists of one M atom sandwiched between two X atoms, building a trigonal prismatic structure as shown Figure 1.3. Stacked layers of TMDs have an overall symmetry as hexagonal, rhombohedral, or tetragonal. Electronic characteristics are listed in Table 1.1. MoS_2 is the most widely investigated and used TMD as channel materials in FETs [37], exhibiting its high ON/OFF switching ratio, which is possible due to the thinness of the active material. Another benefit of the material is its handful extraction methods such as micromechanical cleavage technique [38], [39] or a mild solvent-based exfoliation technique [40]. Large-area MoS_2 can be obtained by chemical vapor deposition (CVD), suggesting its potential for high scalability and degree of morphological control [41], [42].

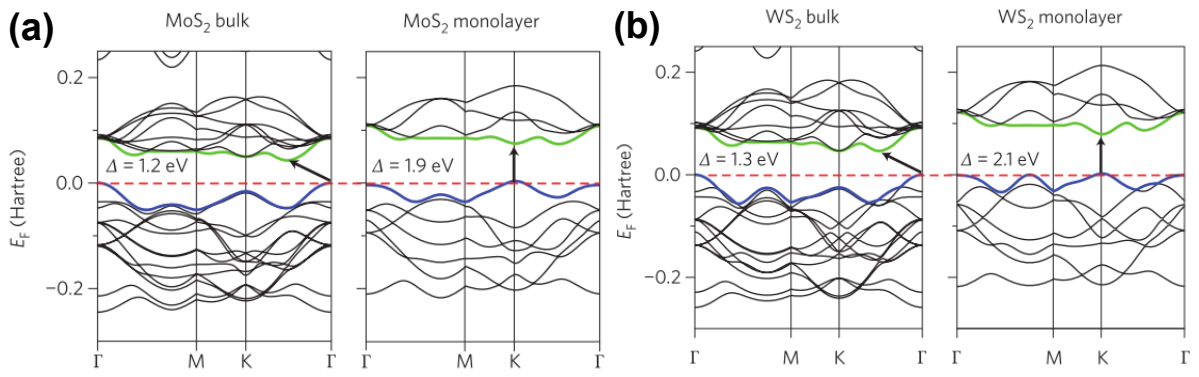

Figure 1.4 Band structure plotted by density functional theory (DFT) for bulk and monolayer of (a) MoS_2 and (b) WS_2. Figures reprinted with permission from reference 43, © 2011 American Physical Society.

Figure 1.4 shows the band structures of bulk and monolayer MoS_2 and WS_2. Monolayer TMDs such as MoS_2 and WS_2 have direct band gap and multilayer counterparts have indirect band gap with a smaller energy gap. Direct band gap in monolayer MoS_2 can produce significant photoluminescence, which can be employed in various optoelectronic applications [43]. Band gap of MoS_2 is ranged from ~1.2 eV for bulk [44] to ~1.8 eV for monolayer [45], [46]. Quantum-mechanical confinement in the vertical direction [43], and the resulting variation in hybridization in p_z orbitals on X atoms and *d* orbitals on M atoms cause this transition of the band gap [45], [47]. Band gaps can also be tuned by applying external electric field. Theoretical studies reported that band gap of few-layer MoS_2 was efficiently engineered by vertical electric field [48], [49]. Electric field as much as 1.0–1.5 V/Å is able to tune the band gap of bilayer MoS_2 to zero [50]. Mechanical deformation can also be used to tune a band gap. Researchers investigated nanotube made up of group-IV 2H MX_2 for their tribological properties. It is shown that WS_2 is resistible up to 10% of elongation strain [51]. Deformation is also utilized with strong electronic effects (straintronics). The band gap is almost linearly decreased under isotropic and unidirectional strain until a semiconductor–metal transition is observed at about 10% isotropic strain [52]. Defects which are often formed by synthesis procedures make a critical impact on the electronic properties of TMDs. One of them is the point defect which results in new photoemission peaks and enhances photoluminescence intensity in monolayer MoS_2 [53]. This is due to localized excitons and the trapping potential of free charge carriers. A simulation work revealed that localized mid-gap states are observed in MoS_2 which does not enhance conductivity but scatter the current [54]. H. Qiu *et al.* exhibited that, due to single atomic vacancies, the average conductance is significantly reduced and large anisotropy of electron transfer is occurred in monolayer with grain boundaries [55].

2D TMD materials are also very promising for photonics applications due to their significant exciton binding energies and their latent capabilities for engineering exciton dynamics. For example, the exciton binding energy of monolayer MoS_2 is ranged from 0.4 to 1.1 eV, which is higher than conventional semiconductor materials by one order of magnitude [56]–[61]. Notably, present active investigation on the optical properties of TMDs is attributed to their strong exciton binding energy. High excitonic absorption and emission of TMDs along with its thinness, flexibility and transparency can lead to the future optoelectronics in mobile devices.

1.1.2.2 Group-IV 2D-Xenes: Silicene, Germanene, Stanene, and Phosphorene

Recently, there are a group of other fundamental 2D materials that have also emerged. Silicene, germanene, stanene, and phosphorene are members of the group, which are the monolayer of silicon, germanium, tin, and black phosphorus, respectively. Generally, thin versions of these materials are not stable and cannot be observed in nature. Nevertheless, stable 2D, slightly buckled (beta-type) honey comb structures of silicon and germanene was announced in 2009 [62]. Similar to electrons in graphene, it is noteworthy that the silicene and germanene have linearly crossing electron bands at the Fermi energy, representing that electrons in the materials behave as massless electrons. Experimentalists revealed that low energy electrons of silicene moves like massless Dirac Fermions and silicene over-laid on silver exhibits Fermi velocities as much as graphene counterpart [63], [64]. Germanene and stanene are also predicted to show similar physics as silicene by first-principles simulations [65], [66]. Especially, a single-layer crystal composed of germanium with one hydrogen bonded in the out-of-plane direction for each atom is called germanane (GeH). While germanene has no band gap, germanane has direct band gap (1.48–1.60 eV) [67] potentially useful optoelectronics. The hydrogenated germanene showed ultrahigh carrier mobility ($> 1.8 \times 10^4$ $\mathrm{cm^2/V \cdot s}$) [67]. Reasonably high field-effect mobility (~ 150 $\mathrm{cm^2/V \cdot s}$) and large ON/OFF current ratio ($> 10^5$) have been reported for GeH field-effect transistors (FETs) [68]. Not only that, notable spin orbit coupling (SOC) was reported in silicene, germanene, and stanine [66], [69]. Due to the large SOC, the materials are regarded as very promising for applications using the quantum spin hall (QSH) effects. Tin-based materials have not been studied as much as silicene and germanene, but, in 2005, the stanene grown by molecular beam epitaxy was announced, confirmed by atomic and electronic characterization using scanning tunneling microscopy and angle-resolved photoemission spectroscopy, in combination with first-principles calculations.[70]. In addition, other first-principles calculations have presented that the band structure of silicene and germanene can be adjusted with a vertical electric field, although extremely large electric fields which would break any known field oxide in FETs are required [71], [72]. Numerical simulation of devices based on these materials has also been explored using Monte-Carlo transport [73].

Phosphorene, also known as monolayer black phosphorus (BP), is another 2D material intriguing intense research attention these days. Recently, it has been revealed that phosphorene has high carrier mobility, and high optical and UV absorption. Its unique anisotropic orthorhombic structure makes it ductile along one of the in-plane crystal directions but stiff in the out-of-plane direction. For the last a

few decades, black phosphorus had got little attention as a semiconductor due to the challenge in controlling the material quality and its small band gap (0.3 eV for bulk). However, recent development in separating few layers recalled black phosphorus for various device applications. L. Li *et al.* published results of theoretical and experimental investigation on black phosphorus field-effect transistors with monolayer and few layers [74]. Table 1.2 provides the band gap and mobility of phosphorene as well as other 2D materials.

2D material	Crystal class	Electronic structure	Bandgap (eV)*	Mobility ($cm^2 V^{-1} s^{-1}$)
Graphene	Hexagonal	Semimetal	NA	2,000–5,000 (supported; experimental values)[130] 200,000 (freestanding; experimental value)[131]
TMDCs (MoS_2)	Hexagonal	Semiconductor	From 1.29 for bulk (indirect) to 1.96 for monolayer (direct)[132]	<320 for electrons, <270 for holes (theoretical values)[133]
Phosphorene	Orthorhombic	Semiconductor	From 0.3 for bulk (direct) to 1.75 for monolayer (direct)	<10,000–26,000 (monolayer; theoretical values) 400–4,000 (few-layer; experimental values)
h-BN	Hexagonal	Insulator	5.971 (direct)[134]	–

h-BN, hexagonal boron nitride; NA, not available; TMDCs, transition metal dichalcogenides. *Bandgap values are all from experimental sources.

Table 1.2 Properties of phosphorene compared with those of other 2D materials. Table reprinted with permission from reference 75, © 2016 Springer Nature.

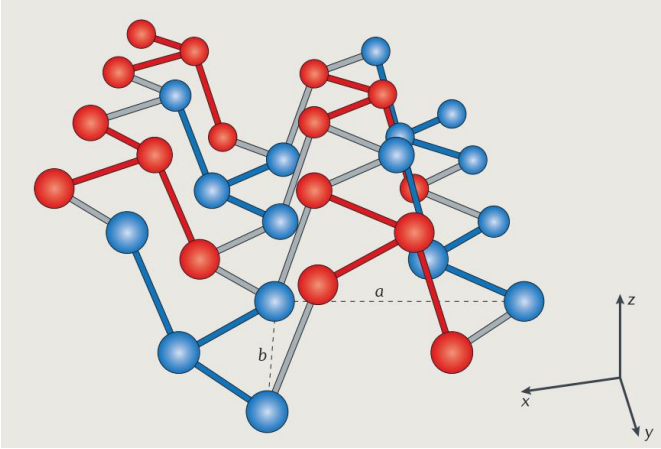

Figure 1.5 The atomic structure of phosphorene. Figure reprinted with permission from reference 75, © 2016 Springer Nature.

White phosphorus P_4 molecule should be considered to understand phosphorus chemistry. Each phosphorus atom forms three bonds with its neighbors and four atoms form a tetrahedron with six single bonds. 3*p* atomic orbitals, which form angle of 90° in the pure status, make major contribution to these bonds. Since bonds of phosphorus are out of perpendicular, it requires arc-like bonds to be stabilized [76], [77].

However, for phosphorene, sp^3 bonds in P_4 bonds are broken to constitute angles of 96.34° and 103.09° which is closer to the angle of perfect tetrahedron, 109.05°. Stability is increased with crystal structure. Resulting atomic structure is shown in the Figure 1.5. The rest pairs have angles of 45° with respect to plane and contribute puckering of the structure. Each atom has two neighbors at 2.224 Å and a third one at 2.244 Å due to two difference bond angles [78]. *y* axis is called the zigzag direction, while the *x* axis is named armchair direction. The lattice constant of the bulk black phosphorus is 4.374, 3.313, and 10.473 Å for *a*, *b*, *c*, respectively, which are determined by using time-of-flight neutron powder diffraction [79]. Nevertheless, there are many factors which make it difficult to precisely decide these lattice constants with DFT calculations: variation of the covalent intralayer bonds and of the weak interlayer bonds, and the directional in-plane bonding geometry [80], [81].

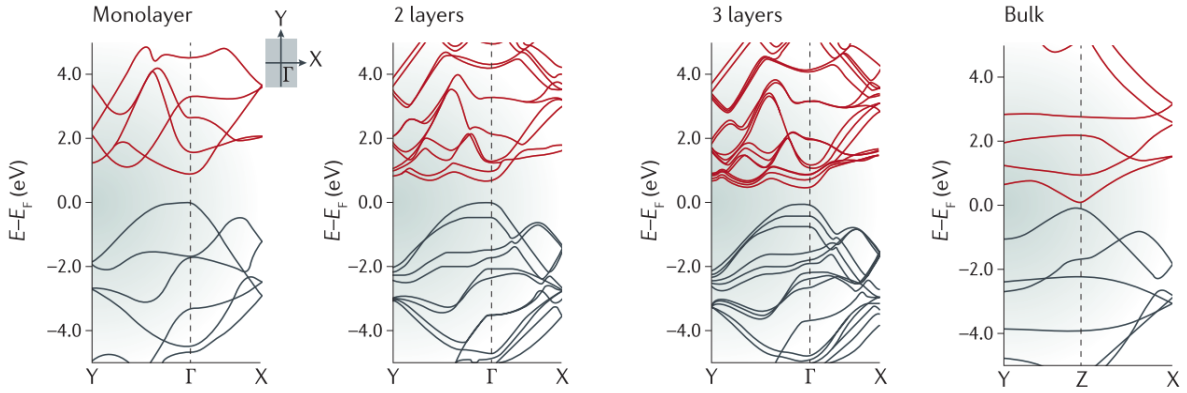

Figure 1.6 Band structures of black phosphorus, plotted by DFT with varying number of layers. Figure reprinted with permission from reference 75, © 2016 Springer Nature.

Band structures of black phosphorus, which depend on the number of layers, are exhibited in Figure 1.6. It shows a concurrent splitting of the bands with increasing number of layers. Monolayer, few-layer and bulk phosphorus have band gaps ranging from ~0.3 eV (bulk) to ~2.0 eV (monolayer) [82]. However, showing that band dispersion is mostly unchanged, the band gaps are measured at Γ point of the first Brillouin zone (BZ) for the all different number of layers. Compared to some TMD materials like MoS_2 or WS_2, exhibiting indirect-to-direct band gap transitions with the change in the number of layers from bulk to monolayer, black phosphorus has direct band gap regardless of the number of layers, which is analogous to some other TMDs such as ReS_2, TiS_3 and InSe. It is significantly beneficial for 2D material to have the direct band gap regardless of the exact number of layers for optoelectronics applications considering the performance and the efficiency of the devices. Large electromagnetic spectrum of black phosphorus is the second advantage for optical applications. The spectrum is covered by the thickness-dependent band gaps, ranging from visible, middle infrared, and even below the spectral region covered by semiconducting TMDs.

Furthermore, phosphorene possesses high carrier mobility due to the significant improvement in preparation and encapsulation methods. Mobility is increased to a value more than 1,000 $\mathrm{cm^2/V \cdot s}$ along the *y* direction with increasing thickness up to 10 nm (see Table 1.2). A theoretical work indicates that this value can be improved even more: in a monolayer, mobility of holes may be increased up to 10,000–26,000 $\mathrm{cm^2/V \cdot s}$, while in thick layer (five-layer), it is around 4,800–6,400 $\mathrm{cm^2/V \cdot s}$ [81].

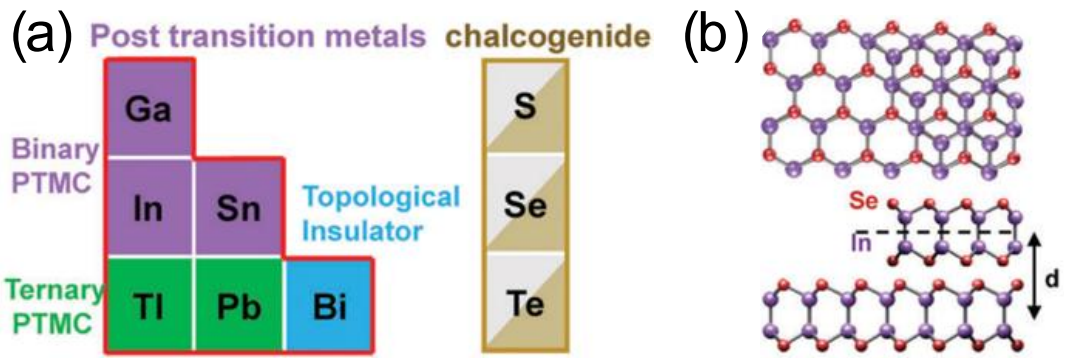

Figure 1.7 Post-transition metal chalcogenides (PTMCs). (a) Element combination of PTMCs, with six recognized post-transition metals: gallium (Ga), indium (In), tin (Sn), thallium (Tl), lead (Pb), and bismuth (Bi). (b) Schematic illustration of the top-view and cross-sectional view of an InSe lattice, with a Se–In–In–Se structure, and each sheet is weakly bound by van der Waals forces. Figures reprinted with permission from: (a) reference 83, © 2018 Royal Society of Chemistry; (b) reference 84, © 2017 Springer Nature.

1.1.2.3 Post-Transition Metal Chalcogenides (PTMCs)

The most recent family of 2D materials, so-called novel post-transition metal chalcogenides (PTMCs), includes combinations of group III elements (e.g., Ga and In) or group IV (e.g., Sn) with chalcogenides as shown Figure 1.7(a). Especially, group IV chalcogenides have two puckered atomic planes analogous to BP [85], [86]. PTMCs based on Ga, In, and Sn are usually semiconductors with variable band gaps relying on the exact combinations between the metals and chalcogens. PTMC based on Ga has larger band gap of 3.3–3.4 eV for monolayer and 1.7–2.5 eV [87] for bulk than that of TMDs. Device using such large band gap materials can be employed for broad wavelength from the UV to visible range [88]. Furthermore, monolayer GaSe has very heavy holes and a large density-of-states due to almost flat valence band in the central region of *E–k* structure [89]. Fast photoresponse has been reported showing distinct optical properties of GaSe [90], [91]. This large effective mass of holes in GaSe could be adapted to electronic application, enabling suppressing the leakage current in sub-5 nm transistors. To avoid short channel effects such as large OFF-state current, large effective mass is preferable. Some *ab-initio* studies revealed that high performance of GaSe FETs even exceeding that of silicon transistor as guided by the ITRS [92]. The studies for a ultra-short channel (3 nm) GaSe FET, demonstrated subthreshold swing (SS) of 92 mV/dec, 4 order of magnitude ON/OFF ratio, and ON

current density of 1.8 $\mathrm{mA}/\mu\mathrm{m}$ [93]. Even though the theoretical investigation predicted high electrical performance, experimentally measured carrier mobility was rather low. Like early state of MoS_2 research, the gap between theory and experiments is due to their large band gap and high resistivity at metal semiconductor contact, and there is possibility to be further improved using better contact engineering.

Unlike Ga-based chalcogenides, other PTMC family has a smaller band gap (~1.2 eV) which is required for high performance electronics. Atomistic structure of InSe is typically M–X–X–M (Se–In–In–Se) and each layer is stacked by van der Waals forces. InSe is known for its light electron mass and high carrier mobility. Two-terminal field effect mobility is much higher than typical TMDs (MoS_2, WSe_2) counterpart and is even as high as state-of-the-art strained silicon devices. However, it is very sensitive to surface phonon scattering at channel–oxide interfaces or the charge impurities [94]–[96]. To avoid that, PMMA was deposited as a trap-free dielectric [96], resulting in a two-terminal field effect mobility $\sim 1{,}055\ \mathrm{cm}^2/\mathrm{V}\cdot\mathrm{s}$ which is higher than that utilizing Al_2O_3 as gate oxide with mobility of $64\ \mathrm{cm}^2/\mathrm{V}\cdot\mathrm{s}$. In addition, some fabrication technology developed in TMDs and BP was used to investigate dependence of hall mobility on temperature [97], [98]. The largest reported field-effect hall mobility in InSe transistor to date is $2{,}000\ \mathrm{cm}^2/\mathrm{V}\cdot\mathrm{s}$ at room temperature and $12{,}700\ \mathrm{cm}^2/\mathrm{V}\cdot\mathrm{s}$ at cryogenic temperature [84], which are better than that of experimental BP transistors introduced above. In addition, due to the larger band gap (1.2 eV) than BP counterpart (0.3 eV), ON/OFF ratio is also several orders of magnitude higher ($> 10^8$). The reasonable band gap and intrinsically large mobility of group III PTMCs were also investigated by *ab-initio* calculation [99], [100]. Simulation by combination of the *ab-initio* and quantum transport in the ballistic regime were carried out, reporting compelling performance with respect to industry requirements [93], [101], [102]. Therefore, PTMCs can be regarded as potentially very attractive semiconductor for high speed digital electronics beyond TMDs and phosphorene.

1.1.3 Insulator: Hexagonal Boron Nitride (hBN)

Hexagonal boron nitride (hBN) is a 2D material which has highly thermoconductive, mechanically strong, and lubricative due to their similar intralayer strong bonds and interlayer weak van der Waals forces. The layer looks white or near transparent with a wide band gap resulting in high insulation, thermal and chemical stability. Therefore, it is possible for hBN to be applied as gate dielectric, protective coating, insulating thermal conductors. Furthermore, since it has an atomically smooth surface that is relatively free of dangling bonds and charge traps, and a lattice constant similar to that

of graphite, hBN can be fascinating substrate for 2D materials. Along with broad research for graphene, 2D hBN was theoretically simulated as good supporter to induce band gap in graphene if graphene was deposited on it [103], which led to experimental enhancement of hBN research significantly [104]. Recently, hBN was crucially utilized as graphene heterostructure to reduce contact resistance. A new device topology where 3D metal electrodes are connected to encapsulated 2D graphene with hBN along the 1D graphene edge were demonstrated as shown in Figure 1.8. Measured contact resistance of the new contact geometry is remarkably low (~150 $\Omega \cdot \mu m$), which is ~25% lower than the best reported surface contacts without additional contact engineering [105]. Not only graphene, these days, hBN is being required almost 2D electronic devices based on TMDs [106]–[108], Group-IV 2D-Xenes [98], [109], and PTMCs [84].

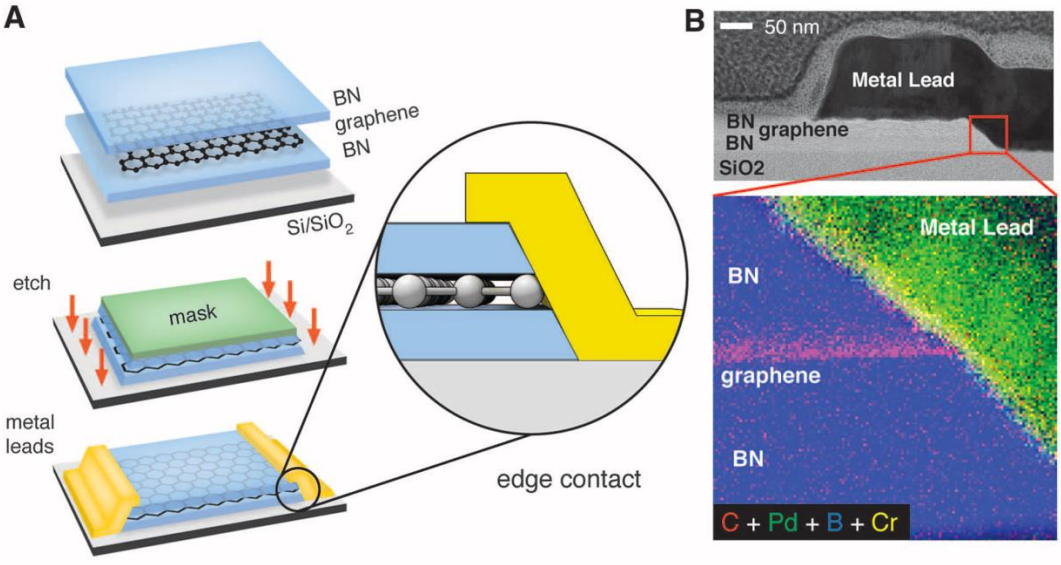

Figure 1.8 (a) Fabrication process of the 3D metal electrodes are connected to encapsulated 2D graphene with hBN along the 1D graphene edge. (b) High-resolution bright-field STEM image showing details of the edge-contact geometry. The expanded region exhibits a magnified false-color EELS map. Figure reprinted with permission from reference 105, © 2013, American Association for the Advancement of Science.

1.2 TMD Electronic Devices

1.2.1 Two-terminal Devices

TMDs are used in some two-terminal devices such as photodetectors due to its high Earth abundance, direct band gap (for monolayer), and appropriate band gap size enabling visible portions of the electromagnetic spectrum, large exciton binding energies, and strong photoluminescence. Some major categories of two-terminal devices are photodiodes, solar cells, and LEDs.

To have short response time for photodetectors, rapid separation and collection of photogenerated carriers within a short distance by a built-in electric field are desired. So far, various junction techniques have been investigated to achieve ultrafast photodetectors including homojunctions between regions with different doping concentration, heterojunctions between two types of semiconductors, and semiconductor–metal Schottky junctions. Recently, a metal–semiconductor–metal (M–S–M) junction has also been introduced. Due to the short channel length design between the two M–S junctions, it resulted in fast response time similar to conventional FETs [110], [111]. Stacks of graphene/TMDs/graphene heterojunctions have been introduced, showing rapid response time down to 50 μs. Heterojunctions for *p*- and *n*-type look promising in photodiode for rapid photodetection. For instance, *n*-type MoS_2 attached to *p*-type Si of crystalline [112] and amorphous [113] have been experimentally investigated. Also, fast photoresponse < 15 µs was obtained from a gate-tunable photodiode which was composed of *p*-type semiconducting single single-wall carbon nanotubes (SWCNTs) and *n*-type monolayer MoS_2 [114].

In addition, TMDs are expected to have great potential for other two-terminal devices such as photovoltaic cells and light-emitting devices. Monolayer and bulk TMDs are well-suited for the photovoltaic applications since those have band gap energy ~1.3 eV, which is desired for high-efficiency photovoltaics according to the Shockley–Quessier limit (see Figure 1.9). A theoretical study revealed that maximum power conversion efficiency (PCE) of a type-II heterojunction between WS_2/MoS_2 is better (1.5%) than that of a Schottky junction solar cell composed of a graphene–MoS_2 stack (~1%) [115]. Roughly 1% of PCE is obtained experimentally from a photovoltaic device with an asymmetric M–S–M Schottky junction on a multilayer MoS_2 flake [116], which is better than a split gated p-n junction on a monolayer WSe_2 flake resulting in 0.5% PCE [117]. Other investigation on heterojunction structures reported that vertically stacked graphene/TMDs/graphene can produce an external quantum efficiency (EQE) of 55% at a single wavelength [118].

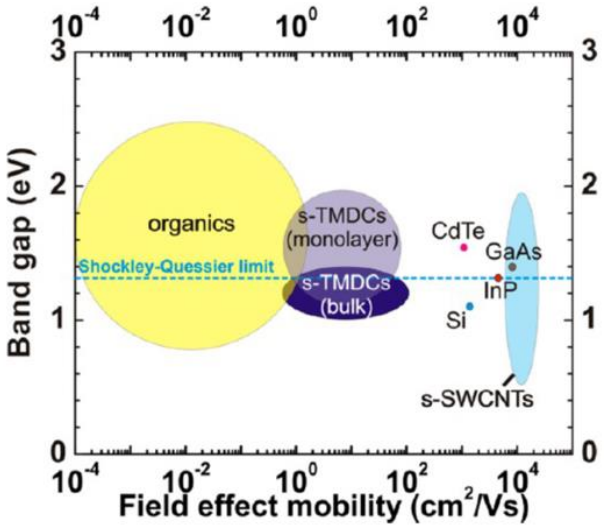

Figure 1.9 Band gap vs. field-effect mobility for conventional and 2D material semiconductors used in current generation photovoltaic technologies. Figure reprinted with permission from reference 119, © 2014, American Chemical Society.

LEDs are another emerging application based on the p-n junction. Due to the need of direct band gap materials, monolayer TMDs could be possible options for transparent and flexible LEDs. Even though it is very difficult to control doping process in fabrication, low quantum efficiencies (~10^{-5}) was reported by LEDs fabricated with a Schottky junction [120]. Homojunction using electrostatic doping in intrinsic monolayer WSe_2 LEDs produced maximum efficiencies of ~0.2% [117], [121]. In heterojunction with monolayer MoS_2 and crystalline *p*-type Si, excitonic electroluminescence has been observed [112]. However, further improvements in doping, surface engineering, encapsulation, and device design are required for LEDs based on TMDs to reach the potential of commercialized organic LEDs exhibiting 20% emission efficiencies.

1.2.2 Three-terminal Devices

1.2.2.1 Switching Applications

TMDs' captivating features, including the absence of dangling bonds, inherently thin structure, and high mobility comparable to Si [122], make them attractive for a channel material in field-effect transistors. Although the electrical properties of bulk semiconducting TMDs have been investigated for decades [123], the very first transistor using TMDs was reported in 2004 [124] just after the landmark paper on graphene by the Manchester group. The TMD transistor adopted WSe_2 as a channel material, which showed up to 500 $cm^2/V \cdot s$ mobility, ambipolar behaviors, and 10^4 ON/OFF current ratio at relatively low temperature of 60 K. Following that, Kis, *et al.* introduced remarkable *n*-type MoS_2 transistor in 2011 [37], as shown in Figure 1.10. Majority carriers flowing through the channel material is determined by Schottky barrier height (Φ_{Bn}) at the metal–semiconductor interface if no doped semiconductor as source and drain is adapted. The top-gated structure with monolayer MoS_2 and HfO_2 as gate dielectric, showed significant ON/OFF current ratio (~10^8), room-temperature mobility (15 $cm^2/V \cdot s$), and 74 mV/decade of subthreshold swing (*SS*). HfO_2 used for high-*k* gate dielectric in this device boosted the mobility due to dielectric engineering [12], [125]–[127]. In another paper, a *p*-type WSe_2 FET with chemically doped source/drain contacts was reported. The device was fabricated with a top-gate geometry and high-*k* dielectric, which demonstrated hole mobility of 250 $cm^2/V \cdot s$, *SS* of ~60 mV/decade and 10^6 ON/OFF current ratio [128].

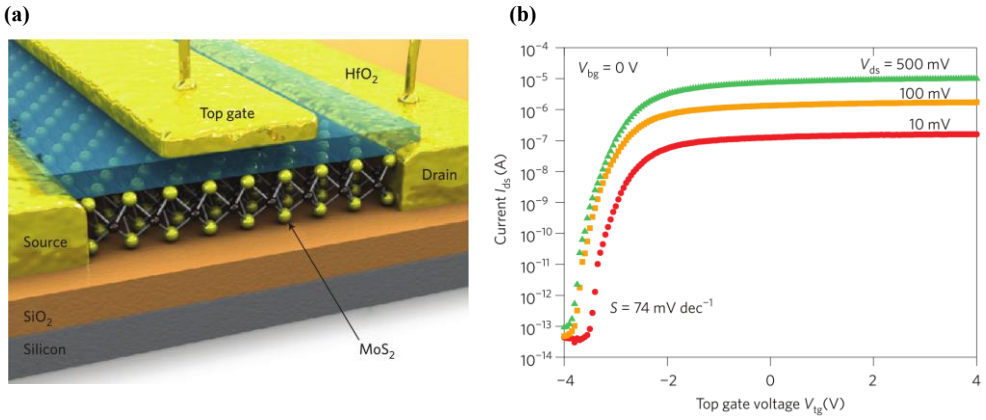

Figure 1.10 (a) Device structure of monolayer MoS_2 FET device with HfO_2-top-gated. (b) Transfer characteristics of device in (a). Figures reprinted with permission from reference 37, © 2011, Springer Nature.

Lately, a number of state-of-the-art devices based on MoS_2 have been investigated. It was reported that atomic-layer-deposited (ALD) high-*k* dielectric was integrated on MoS_2 crystals and dual-gate geometry with ALD Al_2O_3 as the gate dielectric, exhibiting high field-effect mobility of electrons [129]. Moreover, multilayer MoS_2 FETs have been comprehensively investigated, since commercial fabrication processes for monolayer MoS_2 with high-*k* dielectric layer are very limited by its compatibility. The outstanding features include high carrier mobility, excellent subthreshold swing, and robust current saturation over large voltage range [130].

On the other hand, Yoon *et al.* demonstrated theoretical analysis of monolayer MoS_2 transistors based on numerical simulations [131], [132]. Top -gated MoS_2 transistors with 15 nm gate length in the ballistic regime were simulated through the non-equilibrium Green's function (NEGF) based on quantum simulations, which predicted ON current of 1.6 mA/μm, *SS* of ~60 mV/dec, ON/OFF current ratio of 10^{10}, and immunity to short channel effects (drain-induced barrier lowering of ~10 mV/V). Figure 1.11 shows the simulation results of the monolayer MoS_2 transistor at two different drain voltages. Even though the performance cannot beat the conventional III-V transistors, the monolayer MoS_2 transistor would be very suitable for low-power applications due to its large ON/OFF ratio, high Earth abundance to a certain degree, and an excellent electrostatic control. However, short channel effects at a double-gated monolayer MoS_2 FET with channel length of 5 nm are observed in the theoretical investigation [133] due to direct source-to-drain tunneling of electrons, which leads to degraded subthreshold swing. Therefore, improvement to overcome short channel effects in FETs based on short TMDs channel is required.

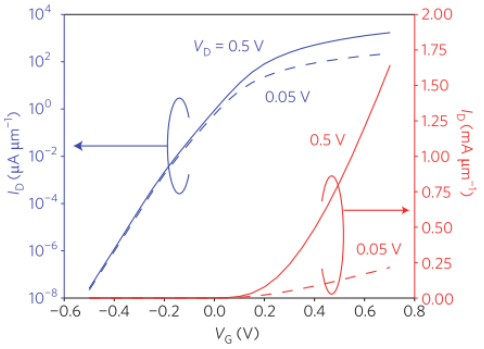

Figure 1.11 Transfer characteristics at two different drain voltages for a monolayer MoS_2 FET device, numerically simulated by NEGF–Poisson's equation self-consistent method. Figure reprinted with permission from reference 132, ©2011, American Chemical Society.

1.2.2.2 Sensing Applications

1.2.2.2.1 Photosensors

Most of photosensors/photodetectors are categorized to two types: photodiodes and photoconductors. For conventional materials, photodiodes were commonly used photodetectors. Phototransistors or so-called Photo-FETs are based on photoconductors structure and additionally have field effect modulation due to applied gate bias. Phototransistors with large photogain usually show slower response times than photodiodes by several orders of magnitude, because both the gain and the time constant are given by the lifetime of the captured carriers [134]. However, they have the potential for extremely high sensitivity due to the gain mechanism, which is much higher than those of photodiodes. For instance, a MoS_2 phototransistor demonstrated dark current close to that of photodiode. The gate-tunable conductivity allows fully depleting the channel in the MoS_2 phototransistor, and due to the atomically thin profile of the monolayer MoS_2, extremely low OFF current densities of 25 fA/μm have been achieved [37]. This indicates that MoS_2 photo-FETs with dimensions of 1 μm × 1 μm can already reach dark currents of only 1 order of magnitude higher than commercial, uncooled InGaAs photodiodes with the same dimensions.

Various phototransistors based on TMDs have been introduced showing high optical performance. Phototransistor based on monolayer MoS_2 reported in 2012 [135] showed promising and advantageous properties for the next generation photodetectors. Even rapid switching behavior of photocurrent generation and annihilation with a responding time within 50 ms was shown in the phototransistor based on the mechanical exfoliation method. In addition, detection of different wavelengths could be achieved by using different thickness of MoS_2 layers. Choi *et al.* published a paper for multilayer MoS_2 phototransistors with an atomic-layer-deposited (ALD) Al_2O_3 gate dielectric layer in a bottom gate TFT configuration [136]. Those achieve higher room temperature mobilities (> 70 $cm^2/V \cdot s$), lower operating gate bias (< 5 V), and a negligible shift in the threshold voltages during illumination, compared to conventional amorphous InGaZnO phototransistors having multiple issues, such as high power consumption and reliability, due to their high SS (> 100 mV/dec), large gate bias (> 10 V), and distinct shift (a few V) in the threshold voltage during illumination. Furthermore, their multilayer MoS_2 phototransistors display better optoelectronic properties than single layer MoS_2 phototransistors, including a wider spectral response (< ~900 nm) and higher photoresponsivity (> 100 mA/W). Another multilayer MoS_2 phototransistors based on transparent gate electrodes were fabricated by Lee *et al.*

[137]. They reported that triple channel layers with a band gap of 1.35 eV produce high photodetection capabilities for red light while green light detection is sensed effectively with mono- and bilayer phototransistors with band gaps of 1.8 eV and 1.65 eV, respectively. Recently, multilayer WS_2 grown by CVD was also used to build phototransistors [138]. Furthermore, significant efforts to increase photocurrent through MoS_2 have also been made by plasmonic Au nanoparticles [139]. It is revealed that one of the dominant optical effects is the thermoelectric effect according to a report on scanning photocurrent measurements of unbiased monolayer MoS_2 devices [140], and others claimed that the dominant mechanism is interband excitation under bias. Contributions from these two mechanisms at zero bias might be varied devices to device [141]. Separation of photoexcited electron–hole pairs across the channel, which results in large net photocurrent, is observed under large drain bias (*i.e.*, saturation mode) due to large enough electric field (Figure 1.12(b)) [142]. Heterostructures are also utilized to enhance photoresponsivity, R. For instance, vertically stacked graphene and MoS_2 channel exhibited $R > 10^7\ \mathrm{A}/W$ [143], [144]. However, even though various 2D-based phototransistors have demonstrated high performance, precise interpretation for key mechanisms of the high optical response is still on immature stage. Following theoretical investigation focusing on both materials and devices are thus required as next step.

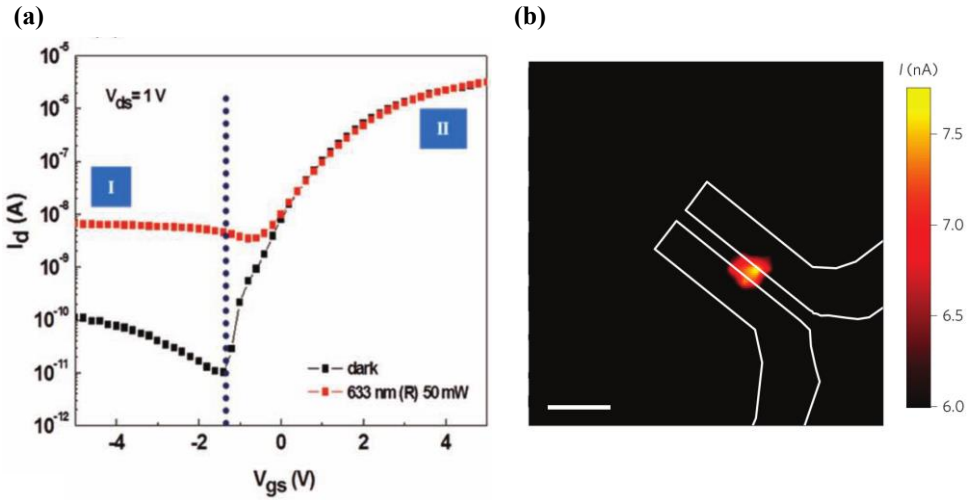

Figure 1.12 (a) Transfer characteristics of a multilayer MoS_2 photo-FET in dark (black) and under illumination (red). (b) Spatial map of the photocurrent recorded as a focused laser beam. Scale bar, 5 μm. Figures reprinted with permission from: (a) reference 136, © 2012 WILEY-VCH Verlag GmbH & Co. KGaA, Weinheim; (b) reference 142, © 2013, Springer Nature.

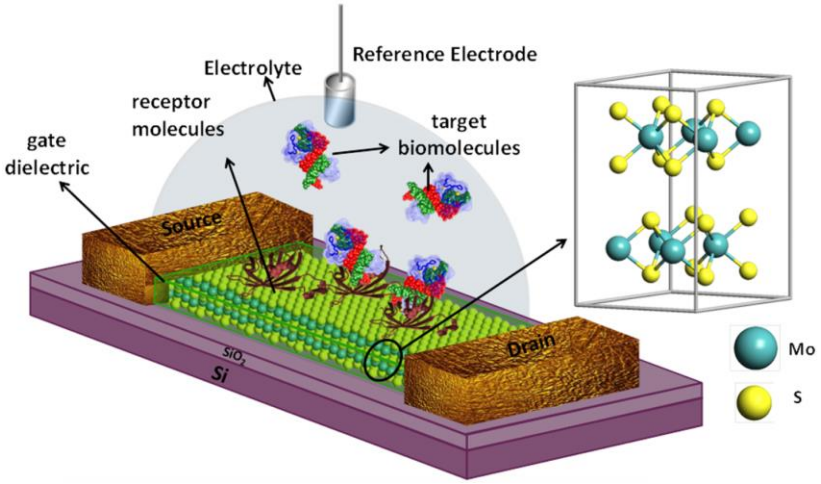

Figure 1.13 Schematic diagram of MoS_2 FET biosensor. Figures reprinted with permission from reference 145, © 2014, American Chemical Society

1.2.2.2.2 Biosensors

Biosensors are now being applied to national security, forensic industries and environmental monitoring as well as diagnostics. FET-based biosensors have triggered vast attention due to FETs' inherit attributes such as fast electrical detection without the requirement for marking the biomolecules, low power consumption, and inexpensive mass production. A MoS_2 FET biosensor geared to ultrasensitive and specific detection of biomolecules was reported in 2014 by Sakar *et al*. [145]. The devices demonstrated not only biomolecule detection but also great value of sensitivity for pH sensing. As mentioned before, lack of dangling bonds is a remarkable advantage of MoS_2 which reduces the scattering of carriers close to the surface and interface traps. Due to this benefit, low interface density-of-states at the semiconductor-insulator interface can lead to better switching control and reduction in low-frequency (flicker) noise, which is fundamental noise in FET biosensors [146]. Furthermore, theoretical analysis were recently performed for MoS_2 FET biosensors for detecting prostate cancer [147]. The devices were numerically simulated to provide a rigorous and comprehensive understanding of the operating mechanism of the devices, and guidelines for the device design optimization with enhancement of the sensitivity. In the future, based on additional features of TMDs such as transparency, flexibility, and mechanical strength, TMDs FET-based biosensors can be extensively adapted for wearable and implantable applications.

1.3 Outline of the Thesis

In this thesis, I focus on main mechanisms of photoillumination effects on phototransistors based on TMDs such as $MoSe_2$ and MoS_2. For thorough understanding of the physical mechanisms, analytical modeling and numerical simulations are carried out.

The thesis is organized as follows. In Chapter 2, device simulation methodologies are introduced. A few electrical transport methods are explained. Among them, non-equilibrium Green's functions (NEGF) is described with two different methods importing electronic states of the channel materials into the transport equations; effective mass and tight-binding approximations. In Chapter 3, uncommon behaviors of a $MoSe_2$ phototransistor are analyzed. To confirm the key origin of uniquely high photoresponsivity of fabricated $MoSe_2$ phototransistors, density-of-states was extracted by temperature-dependent analysis. In Chapter 4, photoillumination effects of $MoSe_2$ phototransistors are analytically modeled. Two main optical mechanisms are modeled; photoconductive (PC) and photogating (PG) effects for in-depth understanding of high photoresponsivity in the fabricated $MoSe_2$ phototransistors. In Chapter 5, The photoillumination effects of $MoSe_2$ phototransistors are numerically simulated. Trap model representing capture and emission of the carriers is introduced. Along with the trap model, the phototransistors are self-consistently simulated by NEGF method to calculate barrier modulation of the PG effect. In Chapter 6, the simulation method used in Chapter 5 is extended to a phototransistor based on the other type of TMDs, MoS_2 nanomesh. High optical response of nano-patterned MoS_2 phototransistors is characterized, and its material and device are theoretically analyzed by density functional theory (DFT) and NEGF with the trap model, respectively. In chapter 7, conclusions and suggestions for further study are made.

Chapter 2 Device Simulations

All the simulations conducted in this paper employed a self-consistent simulation scheme between the electrostatic potential and the charges inside the nanoscale electronic devices. Considering three-terminals devices, source and drain bias voltages are applied for carrier injection and ejection, and gate bias is applied to control the conductance of the device. It is called 'self-consistent' since the changes in $\rho(\vec{r})$ adjust potential $U_{SC}(\vec{r})$ inside the device, which in turn alters charge density until both the potential and charge density reach consistent values. For this iterative simulation, two major equations are needed: the Poisson's equation and the transport equation. Input and output of the Poisson's equation are charge density $\rho(\vec{r})$ and the self-consistent potential $U_{SC}(\vec{r})$, respectively (see Figure 2.1). It is solved by a finite difference method (FDM) method, which will be explained in Section 0. On the other hand, a full quantum mechanical transport model based on NEGF formalism results in charge density, $\rho(\vec{r})$ using the self-consistent potential $U_{SC}(\vec{r})$ from the Poisson's equation as an input. The formalism will be introduced in the Section 2.1.2.1.

The self-consistent procedure for a quantum mechanical simulation of FETs consists of following steps [148]:

1. All the operators are discretized by setting FDM for a given FET structure.
2. An initial guess value of $U_{sc}(\vec{r})$ is given to initiate self-consistent loop (*e.g.*, a potential $U_{sc}(\vec{r})$ of flat band condition, or the final potential of the previous simulation, which possibly has the closest solution to the self-consistent potential of the new simulation)
3. For a given $U_{sc}(\vec{r})$, a suitable Hamiltonian, H, can be written for the device and then contact self-source/drain energy matrices are computed, respectively.
4. Considering all above information, the retarded Green's function is calculated, which leads to charge density matrix.
5. The computed charge density in the previous step is fed into the Poisson's equation to calculate the self-consistent potential, $U_{sc}(\vec{r})$.
6. Steps 3–5 will be continued until the error between the new and the previous potential energies becomes less than a certain criterion.

7. Finally, the current through the device is calculated from the converged self-consistent potential and charge.

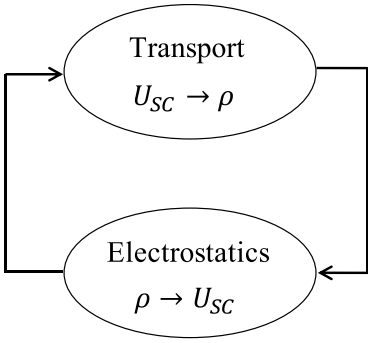

Figure 2.1 Self-consistent diagram showing an iteration between the transport and the Poisson's equation [148].

2.1 Transport

2.1.1 Semi-classical Transport Simulations

2.1.1.1 Drift-Diffusion Transport

Carrier transport of micron or sub-micron FETs can be accurately calculated by conventional carrier transport models. They basically stem from the Boltzmann transport equation (BTE) by involving a few simplifying closure approximations [149]. They primarily describe scattering-dominant transport, which is usual in long channel devices. However, carrier transport in nanoscale devices is in quasi-ballistic transport regime [150], and therefore, such classical models may not be suitable to predict device performance and describe underlying physics of nanoelectronics [151], [152].

The classical BTE is a complex integro-differential equation. It is based on collective viewpoint instead of individual particle picture and formulates an equation for $f(\vec{r}, \vec{k}, t)$, which is the Fermi distribution function under equilibrium at position $\vec{r}$, with momentum $\vec{k}$, at time t, assuming a Newtonian movement of the particles. The Boltzmann transport equation (BTE) is provided with

$$\frac{\partial f}{\partial t} + \vec{v} \cdot \nabla_r f - \frac{q\vec{E}}{\hbar} \nabla_k f = \left.\frac{\partial f}{\partial t}\right|_{Coll} \tag{2.1}$$

where $\vec{E}$ is the electric field and $\left.\frac{\partial f}{\partial t}\right|_{Coll}$ is the collision term resulting solely from two-body collisions between particles which are assumed to be uncorrelated prior to the collision. In general, Equation (2.1) should be solved to find f.

It is very difficult to obtain solution to the BTE without approximations such as a response matrix approach [153]. A method of directly solving the six-variable equation in the steady state was proposed [154]. However, as we mentioned earlier, the BTE describes carrier dynamics in a classical approach, quantum mechanical phenomena in nanoscale devices can be hardly captured in the solutions. Furthermore, a non-degenerate distribution function is typically used to simplify the scattering operator $\frac{\partial f}{\partial t}$ when solving the equation [154]. This approximation breaks Pauli's exclusion principle, which is obviously essential in describing the scattering of a highly degenerate carrier gas within extremely short channel transistors.

Semiclassical descriptions based on the solution of the BTE can be categorized as Monte-Carlo (MC) and drift-diffusion (DD) transport. MC provides statistical solution of BTE and has been widely employed for the study of transport in semiclassical approaches in traditional semiconductors. It utilizes statistics to track the path of classical particles in between random scattering events that change the particle's path and the particles are treated quantum-mechanically using Fermi's golden rule.

On the other hands, DD has been one of the most popular approximations to calculate transport in conventional semiconductor devices [155], [156]. Based on BTE approximated under the relaxation time, DD can be derived from current equation defined as summation of drift current and diffusion current density ($J = J_{drift} + J_{diff}$). Electron current density is $J_n = qn\mu_n\vec{E} + qD_n\nabla n$, while hole current density is $J_p = qp\mu_p\vec{E} - qD_p\nabla p$, where q, n, p, μ_n, μ_p, $\vec{E}$, D_n, and D_p are single electron charge, electron and hole concentration, field effect electron and hole mobility, electric field, electron and hole diffusion coefficients, respectively. $\mu_{n/p}$ and $D_{n/p}$ are functions of electric field. Density-of-states through Fermi-Dirac integral of n and p enter into the model as materials description information. Current density can be obtained by the current equations with help of continuity equation introducing a time-dependent variation of the carrier densities, which is defined as: $\frac{dp}{dt} = -\frac{1}{q}\nabla \cdot J_p - R + G$ for n-type transistors, and $\frac{dn}{dt} = \frac{1}{q}\nabla \cdot J_n - R + G$ for p-type transistors, where R and G are

recombination and generation rate, respectively. By assuming steady-state condition and no net generation rate, left-hand sides of the continuity equations become zero, resulting in $\nabla \cdot J_n = 0$ and $\nabla \cdot J_p = 0$, meaning that current densities at every position in the device are equal. Next, the drift-diffusion equations are discretized by finite difference method (FDM). Finally, by using numerical iterative or direct methods, the discretized equations are computationally solved for charges and current densities.

Commonly, DD is a proper model to calculate charge transport based on diffusive regime in microscale device [157], [158]. While the electron gas is assumed to be in thermal equilibrium with the lattice temperature ($T_n = T_L$) in the DD approach, electrons gain energy from the field and the temperature T_n of the electron gas increases in the presence of a strong electric field. Since the pressure of the electron gas is proportional to nk_BT_n, the driving force now becomes the pressure gradient rather than merely the density gradient. This introduces an additional driving force, namely, the temperature gradient besides the electric field and the density gradient. This is called hydrodynamic (HD) model whose current is rewritten as $J = J_{drift} + J_{diff} + \rho D_T \nabla T_n$, where ρ is charge concentration, D_T is thermal diffusivity, and T is temperature. When electric field is very high in the device, MC method can be replaced with HD which has been employed to investigate dependence of transport in graphene at high-field on different substrates [159].

2.1.1.2 Top of the Barrier Model

In DD transport model, electrons drift and diffuse from source to drain due to electrical field and charge concentration gradient. While electrons are moving, those are bothered by numerous scattering events relaxing their momentum and energy. The scattering effects are considered in DD model by mobility and diffusion coefficient. On the other hand, in the ballistic regime, it is assumed that the electrons travel in the channel without any obstacles which scatter electrons' movements, resulting in no loss of momentum or energy. At the same time, energy barrier in the channel modulated by gate bias still obstruct path of the electrons. If the energy of the barrier is higher than their energy, they are simply reflected back. Otherwise, the electrons reach the drain with probability of 100%. This model still treats the carriers as semi-classical particles since effect of any quantum effect such as interferences and tunneling are entirely disregarded. The local density-of-states within the device is just that of a bulk semiconductor but pulled up or down by the local electrostatic potential. This approximation works well only when the electrostatic potential does not vary too rapidly. It is obvious that the critical energy which determines transmission of the carriers is the maximum barrier height in the channel, and thus it is called the "top of the barrier model".

To evaluate the electron density along the channel position within the ballistic device we should compute two terms: one for the states filled from the source and another for the states filled from the drain.

$$n(x) = \int dE[\mathrm{LDOS}_L(x,E)f_L(E) + \mathrm{LDOS}_R(x,E)f_R(E)] \tag{2.2}$$

where, $\mathrm{LDOS}_{L/R}(x,E)$ are local density-of-states at energy E, fillable from source or drain within the device, which is just that of a bulk semiconductor but shifted up or down by the local electrostatic potential. The density-of-state contains summation over spin states. For diffusive transport, a single density-of-states is treated and it is filled depending on a source quasi-Fermi level, but for ballistic devices, the density-of-states separates into parts fillable from each lead. The current flowing from source to drain (or drain to source) can be obtained by simply the transmission probability $T(E)$ at energy E times the Fermi distribution of the source (drain). The total current in the device can be expressed as

$$I = \frac{2q}{h}\int dET(E)[f_L(E) - f_R(E)] \tag{2.3}$$

For Figure 2.2, $T(E) = 0$ for $E < E_{TOP}$ and $T(E) = 1$ for $E > E_{TOP}$.

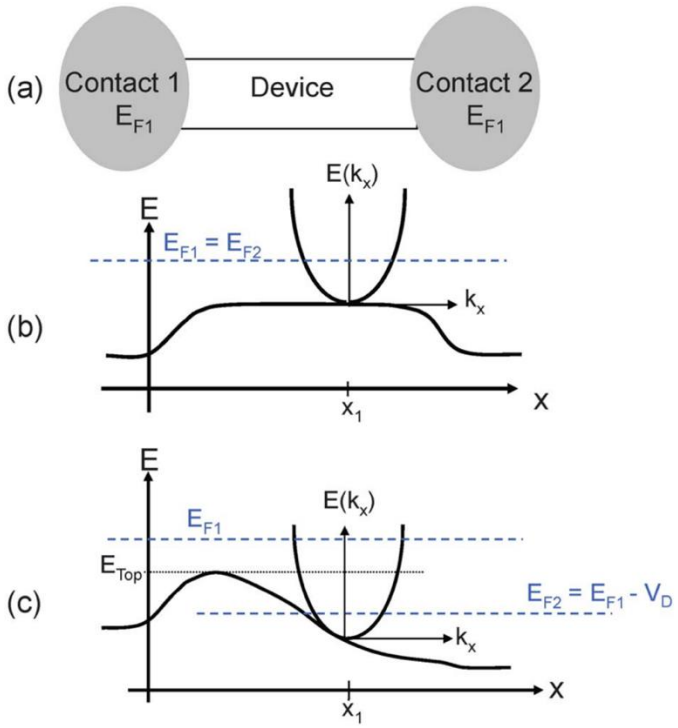

Figure 2.2 (a) Schematics of a ballistic device with two contacts that function as reservoirs of thermal equilibrium carriers. Energy band diagram (b) under equilibrium conditions, and (c) under bias. Figures reprinted with permission from reference 159, © 2008, IEEE.

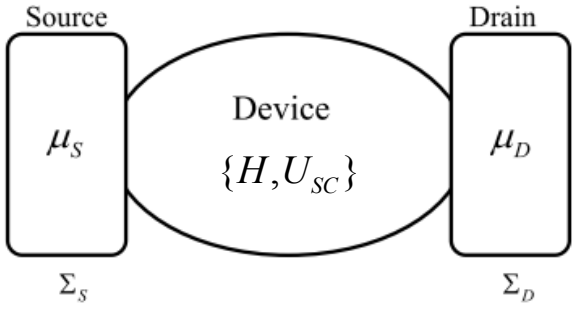

Figure 2.3 Schematic structure of quantum transport in a device where the channel is connected to the source/drain contacts [148].

2.1.2 Quantum Transport Simulations

2.1.2.1 Non-equilibrium Green's Function (NEGF) Transport

To predict and explore device characteristics of nanoscale FETs, transport properties are investigated using the non-equilibrium Green's function (NEGF) formalism [148], [160]–[166] under non-equilibrium bias situations and open boundary conditions through contacts. The NEGF formalism has been adopted to investigate a variety of devices from conventional Si MOSFETs [167] to MOSFETs of new channel materials [168], or to carbon nano-tube FETs. In this section, the fundamentals of the NEGF formalism will be described briefly.

Hamiltonian, *H,* which can describe the electronic properties (potential and kinetic energies) of the active material should be provided with the NEGF. In this study, *H* is described based on effective mass (EM) or tight-binding approximation (TB). The channel is connected to two-terminal conductors, source (S) and drain (D) (see Figure 2.3). Applied bias between the two contacts determines the difference of the electrochemical potential levels (μ_S and μ_D) and how electrons are thermally distributed in each contact through the Fermi function, $f_{S/D}$. As an isolated channel is coupled to the S/D contacts, the discrete levels within the channel broaden into a continuous density-of-states. Coupling between the active channel and the S/D contacts is described by using appropriate self-energy matrices (Σ_S and Σ_D). After getting *H*, Σ_S, Σ_D, μ_S and μ_D, we can calculate the retarded Green's function [166] at a given energy as

$$\mathrm{G}(E) = [(E + i0^+)I - H - \Sigma_s - \Sigma_D]^{-1} \tag{2.4}$$

where *E* is energy and *I* is the identity matrix, and $0^+$is an infinitesimal positive value. In the ballistic regime, the local density-of-states (LDOS) is given by spectral function $[A] = i[G - G^+] = [A_S] + [A_D]$, where $A_{S/D} = G\Gamma_{S/D}G^+$, and $\Gamma_{S/D} = i[\Sigma_{S/D} - \Sigma_{S/D}^+]$ represents the energy level broadening due to the source/drain contacts. Then, the electron correlation function is expressed as

$$[\mathrm{G}^n] = [\mathrm{G}\Gamma_\mathrm{S}\mathrm{G}^+]f_S + [\mathrm{G}\Gamma_D\mathrm{G}^+]f_D \tag{2.5}$$

which is used to obtain the charge density:

$$\rho = \frac{1}{2\pi}\int \mathrm{G}^n(E)dE \tag{2.6}$$

This charge is given to the Poisson's equation to calculate a new potential which will be the input of NEGF formalism. This iteration continues until it satisfies a criterion, which will be explained in detail in the Section 0. If $f_s = f_D = 1$, then all states are filled with electrons, and thereby [G^n] becomes LDOS. Subsequently, current at source or drain terminal per spin [166] is calculated as

$$I_{S/D} = (q/h)\int_{-\infty}^{+\infty} \tilde{I}_{S/D}(E)dE \tag{2.7}$$

where $\tilde{I}_{S/D} = \text{Trace}\left[\Gamma_{S/D}\text{A}\right]f_{S/D} - \text{Trace}[\Gamma_{S/D}G^n]$, and h is Planck's constant.

2.1.2.2 Electronic States

Hamiltonian matrix describes the fundamental electronic properties of the material and is key input to NEGF simulations. The Hamiltonian H consists of two parts [166]: isolated materials, H_0, and the potential, U.

$$H = H_0 + U \tag{2.8}$$

In this section, three different approximations in the Hamiltonian matrix will be introduced.

2.1.2.2.1 Effective Mass (EM) Approximation

As the simplest approach, the effective mass (EM) method can be adopted to discretize the Hamiltonian operator to the matrix [H]. Without using *ab-initio* or TB method, it is very difficult to describe exact Hamiltonian matrix of a material due to complexity of the band structure of TMDs in conduction and valence bands. The EM method offers a much more handful way to represent electronic properties of semiconductor since its description around the lowest (highest) energy levels close to conduction band (valence band) can be given with a parabola for n-type (p-type) semiconductors. For example, for an n-type semiconductor, this simple relationship can be expressed as [166]

$$h(\vec{k}) = E_c + \frac{\hbar^2 k^2}{2m^*} \tag{2.9}$$

where E_c and m_e are the conduction band minima and the effective mass of electrons, respectively, and m^* can be determined by fitting the parabola equation on to the band structure. Replacing $\vec{k}$ with $-i\vec{\nabla}$, Equation (2.9) can be changed to a differential equation which has the same energy eigenvalues easily written like this [166]:

$$\left[E_c - \frac{\hbar^2}{2m^*}\nabla^2\right] f(\vec{r}) = Ef(\vec{r}) \tag{2.10}$$

Plane wave solutions, $f(\vec{r}) = \exp(\mathrm{i}\vec{k}\cdot\vec{r})$, can be easily checked if those are eigenfunctions corresponding to eigenvalues, $E(\vec{k}) = E_c + (\hbar^2 k^2/2m^*)$. Then, Equation (2.10) can be converted to the Hamiltonian matrix through the finite difference method, which is much simpler for computational calculation. For instance, H_0 in 1D structure (see Figure 2.4) can be written as:

$$H_0 = \begin{array}{c} \\ 1 \\ 2 \\ \vdots \\ N-1 \\ N \end{array} \begin{array}{c} \begin{array}{cccccc} 1 & 2 & \cdots & N-1 & N \end{array} \\ \begin{bmatrix} 2t_0 & -t_0 & & 0 & 0 \\ -t_0 & 2t_0 & & 0 & 0 \\ & & \ddots & & \\ 0 & 0 & & 2t_0 & -t_0 \\ 0 & 0 & & -t_0 & 2t_0 \end{bmatrix} \end{array} \tag{2.11}$$

where t_0 is hopping energy, defined as $t_0 = \frac{\hbar^2}{2m^*a^2}$ where a is grid spacing.

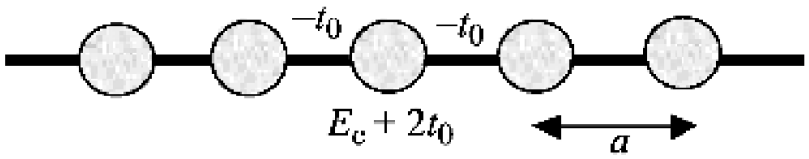

Figure 2.4 The effective mass Hamiltonian matrix in 1D can be visualized as a 1D array of unit cells each with energy $E_c + 2t_0$ bonded to its nearest neighbors by $-t_0$. Figures reprinted with permission from reference 165, © 2005, Cambridge University Press.

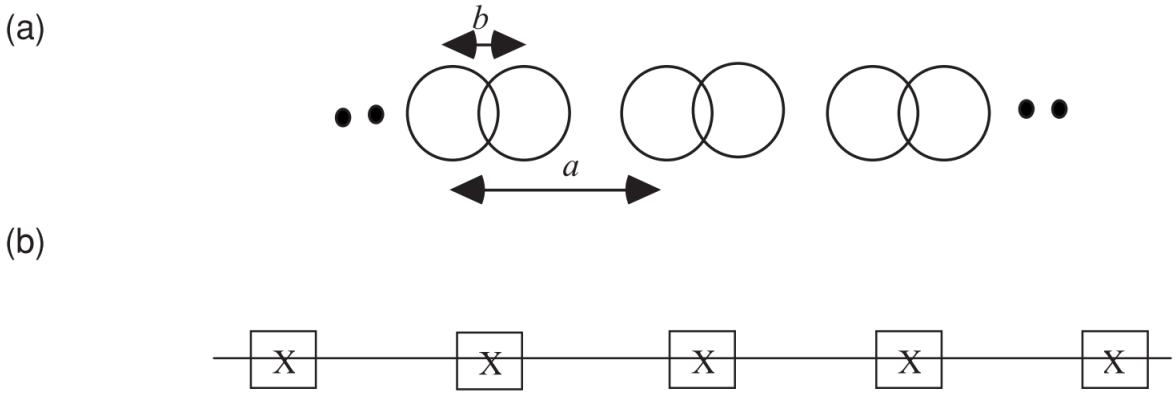

Figure 2.5 (a) A one-dimensional solid whose unit cell consists of two atoms. (b) Basic lattice defining the periodicity of the solid. Figures reprinted with permission from reference 165, © 2005, Cambridge University Press.

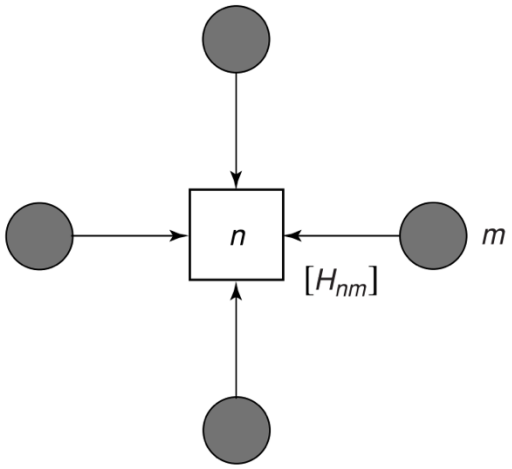

Figure 2.6 Schematic picture showing a unit cell *n* connected to its neighboring unit cells *m* by a matrix [H_{mn}] of size ($b \times b$), *b* being the number of the basis functions per unit cell. Figures reprinted with permission from reference 165, © 2005, Cambridge University Press.

2.1.2.2.2 Tight-Binding (TB) Approximation

The TB method is a very powerful way to calculate *E–k* relation using an approximate set of the basis functions per unit cell. If we use *N* unit cells *b* basis per unit cell, we can write down Hamiltonian matrix with size of $Nb \times Nb$. To establish a general form of the TB Hamiltonian, let's see an arbitrary unit cell *n* (Figure 2.6) surrounded by its neighboring unit cells *m* with the relationship described by matrix [H_{nm}] (size of $b \times b$), where *b* is the number of the basis functions in one unit cell. If there are *N* number of unit cells in the structure and we divide [*H*] matrix (size of $Nb \times Nb$) into a set of equations following a method used in a one-dimensional solid, the overall matrix equation is expressed as

$$E\{\phi_n\} = \sum_m [H_{nm}]\{\phi_m\} \tag{2.12}$$

where $\{\phi_n\}$ is a (b × 1) column vector indicating the wavefunction in unit cell *m* and *E* is the corresponding eigenstate of the Schrödinger Equation. It is noticed that this equation can be solved if the solution is

$$\{\phi_n\} = \{\phi_0\} e^{i\vec{k}\cdot\vec{d_n}} \tag{2.13}$$

This solution can be put into Equation (2.12) and be solved as

$$E\{\phi_0\}e^{i\vec{k}\cdot\overrightarrow{d_n}} = \sum_m [H_{nm}]\{\phi_0\}e^{i\vec{k}\cdot\overrightarrow{d_m}}$$
$$E = \sum_m [H_{nm}]\, e^{i\vec{k}\cdot(\overrightarrow{d_m}-\overrightarrow{d_n})} \tag{2.14}$$

Therefore,

$$E\{\phi_0\} = \left[h(\vec{k})\right]\{\phi_0\} \tag{2.15}$$

with

$$\left[h(\vec{k})\right] = \sum_m [H_{nm}]e^{i\vec{k}\cdot(\overrightarrow{d_m}-\overrightarrow{d_n})} \tag{2.16}$$

where the size of the matrix $\left[h(\vec{k})\right]$ is $b \times b$. This form is applied to any unit cell n. All the neighboring unit cells (including itself) which has an overlap (non-zero matrix) should be taken into consideration when the summation in Equation (2.16) is done. Then, same as a one-dimensional solid, the set of eigenvalues of $\left[h(\vec{k})\right]$ for each value of $\vec{k}$ can be plotted as a *E–k* band structure. The number of eigenvalues per one $\vec{k}$ value is equal to the number of basis function, b. Therefore, there will be b number of curves in the band structure plot. Also, as long as $[H_{nm}]$ and the position vector, $\overrightarrow{d_m} - \overrightarrow{d_n}$, are achievable, we can make up a Hamiltonian matrix $[H]$ which can be inserted to calculate the transport of the device in NEGF formalism which was explained details in the Section 2.1.2.1.

In this thesis, three-band TB model involving the third nearest-neighbor (TNN) hoppings [169] is utilized for the device simulations. This is called "TNN TB" in the following, and it is greatly efficient way to build the Hamiltonian matrix for TMDs materials. In the TMDs MX_2 (M = Mo, W; X = S, Se, Te), this model considers only the *d* orbitals as bases in the M atom, especially,d_z^2, d_{xy}, and $d_{x^2-y^2}$ orbitals. The model is sufficient to capture the band-edge properties in the ±K valleys, including the energy dispersions as well as the Berry curvatures, The TNN TB Hamiltonian matrix is obtained as

$$\left[H^{TNN}(\vec{k})\right] = \begin{bmatrix} V_0 & V_1 & V_2 \\ V_1^* & V_{11} & V_{12} \\ V_2^* & V_{12}^* & V_{22} \end{bmatrix} \tag{2.17}$$

in which

$$V_0 = \epsilon_1 + 2t_0(2\cos\alpha\cos\beta + 2\cos\alpha) + \epsilon_1 + 2r_0(2\cos 3\alpha\cos\beta + \cos 2\beta) + 2u_0(2\cos 2\alpha\cos 2\beta + \cos 4\alpha) \tag{2.18}$$

$$\mathrm{Re}[V_1] = -2\sqrt{3}t_2\sin\alpha\sin\beta + 2(r_1 + r_2)\sin 3\alpha\sin\beta - 2\sqrt{3}u_2\sin 2\alpha\sin 2\beta \tag{2.19}$$

$$\mathrm{Im}[V_1] = 2t_1\sin\alpha\,(2\cos\alpha + \cos\beta) + 2(r_1 - r_2)\sin 3\alpha\cos\beta + 2u_1\sin 2\alpha\,(2\cos 2\alpha + \cos 2\beta) \tag{2.20}$$

$$\mathrm{Re}[V_2] = 2t_2(\cos 2\alpha - \cos\alpha\cos\beta) - \frac{2}{\sqrt{3}}(r_1 + r_2)(\cos 3\alpha\cos\beta - \cos 2\beta) + 2u_2(\cos 4\alpha - \cos 2\alpha\cos 2\beta) \tag{2.21}$$

$$\mathrm{Im}[V_2] = 2\sqrt{3}t_1\cos\alpha\sin\beta + \frac{2}{\sqrt{3}}\sin\beta\,(r_1 - r_2)(\cos 3\alpha + 2\cos 3\alpha) + 2\sqrt{3}u_1\cos 2\alpha\sin 2\beta \tag{2.22}$$

$$V_{11} = \epsilon_2 + (t_{11} + 3t_{22})\cos\alpha\cos\beta + 2t_{11}\cos 2\alpha + 4r_{11}\cos 3\alpha\cos\beta + 2\left(r_{11} + \sqrt{3}r_{12}\right)\cos 2\beta + (u_{11} + 3u_{22})\cos 2\alpha\cos 2\beta + 2u_{11}\cos 4\alpha \tag{2.23}$$

$$\mathrm{Re}[V_{12}] = \sqrt{3}(t_{22} - t_{11})\sin\alpha\sin\beta + 4r_{12}\sin 3\alpha\sin\beta + \sqrt{3}(u_{22} - u_{11})\sin 2\alpha\sin 2\beta \tag{2.24}$$

$$\mathrm{Im}[V_{12}] = 4t_{12}\sin\alpha\,(\cos\alpha - \cos\beta) + 4u_{12}\sin 2\alpha\,(\cos 2\alpha - \cos 2\beta) \tag{2.25}$$

$$V_{22} = \epsilon_2 + (3t_{11} + t_{22})\cos\alpha\cos\beta + 2t_{22}\cos 2\alpha + 2r_{11}(2\cos 3\alpha\cos\beta + \cos 2\beta) + \frac{2}{\sqrt{3}}r_{12}(4\cos 3\alpha\cos\beta - \cos 2\beta) + (3u_{11} + u_{22})\cos 2\alpha\cos 2\beta + 2u_{22}\cos 4\alpha \tag{2.26}$$

$$(\alpha, \beta) = \left(\frac{1}{2}k_x a, \frac{\sqrt{3}}{2}k_y a\right) \tag{2.27}$$

where a is the lattice constant and ϵ_j is the on-site energy corresponding to each atomic orbital. There are multiple independent parameters in $H^{TNN}(k)$: ϵ_1, ϵ_2, t_0, t_1, t_2, t_{11}, t_{12}, t_{22}, r_0, r_1, r_2, r_{11}, r_{12}, u_0, u_1, u_2, u_{11}, u_{12}, and u_{22}.These parameters are determined by fitting the band structures on the first-principles (generalized-gradient approximation) results. Since the low-energy physics near the ±K points are the most interested energy region for the device simulations, the band energies are fitted at

the points, with least-square fitting. For $MoSe_2$ whose lattice constant, a = 3.326 Å, the obtained parameters are listed in Table 2.1

ϵ_1	ϵ_2	t_0	t_1	t_2	t_{11}	t_{12}	t_{22}	r_0	
r_2	r_{11}	r_{12}	u_0	u_1	u_2	u_{11}	u_{12}	u_{22}	r_1
0.684	1.546	-0.146	-0.130	0.432	0.144	0.117	0.075	0.039	
0.069	0.052	0.060	-0.042	0.036	0.008	0.272	-0.172	-0.150	-0.209

Table 2.1 Fitted parameters (in units of eV) for the three-band TNN TB model based on the FP bands in generalized-gradient approximation case.

2.1.2.2.3 Modified Effective Mass (EM) Approximation

According to the previous chapters, both EM and TB methods have their pros and cons. I propose a new methodology of ballistic quantum transport simulation based on EM approximation for TMDs FETs, providing accurate charge transport calculation and light computational calculation load at the same time. I thoroughly explain method to calculate new effective mass maintaining density-of-states (DOS) to improve accuracy of carrier transport.

Simulation Method A simulation scheme of modified EM method is introduced based on original EM approximation since it provides significantly shorter calculation time compared to TB approximation. In the simulation, the drain current is calculated once self-consistency is achieved. The current equation can be written as a function of the transmission coefficient from the source contact to drain contact [166] as following

$$T_{SD} = \text{trace}[\Gamma_S G \Gamma_D G^{\dagger}] \tag{2.28}$$

where G is retarded Green's function, and $\Gamma_{S/D} \equiv i(\Sigma_{S/D} - \Sigma_{S/D}^{\dagger})$. $\Sigma_{S/D}$ is self-energy matrix for the source/drain contacts. Then, transmitted current is calculated analytically by flowing equation [170]:

$$I[E(k_x)] = \frac{q}{\hbar^2}\sqrt{\frac{m_y^* k_B T}{2\pi^3}}\{\mathcal{F}_{-1/2}[\mu_S - E(k_x)] - \mathcal{F}_{-1/2}[\mu_D - E(k_x)]\}T_{SD}[E(k_x)] \tag{2.29}$$

where q, $\hbar$, m_y^*, k_B, T, and $\mathcal{F}_{-1/2}$, are the single electron charge, plank constant, electron effective mass along the transverse (y) direction, Boltzmann constant, temperature, and Fermi–Dirac integral accounting for all transverse mode contributions, respectively. The total current is achieved by summing over all conduction band valleys and integrating over all $E(k_x)$. According to the Equation (2.29), the transmitted current directly depends on effective mass along transverse direction, m_y^*, which means that the current is directly determined by shape of paraboloid of approximated band structure in the conduction band. With original isotropic effective mass, the contour has circular shape as shown in Figure 2.7(a) while, with modified anisotropic effective mass, for instance, decreased m_y^* and increased m_x^*, the paraboloid becomes oval cup as shown in Figure 2.7(b), resulting in smaller transmitted current.

Next, it would be handful to modulate value of the current by changing only m_y^* if the transmission coefficient is maintained. To do this, we should have same self-consistent effect on the electrostatic

potential with different effective mass. This can be realized through maintaining DOS by keeping DOS effective mass $\left(m_r = \sqrt{m_x^* m_y^*}\right)$, according to [171].

Considering these, the simulation scheme consists of following steps:

1. Given device structure and material parameters, we simulate FETs for plotting I_D–V_G characteristics based on EM approximations.
2. Next, ON-state gate bias, V_{ON}, is determined by $V_{ON} = V_{OFF} + V_{DD}$, where V_{OFF} is OFF-state gate voltage which gives small current (generally 10^{-3}–10^{-4} [A/m]), and V_{DD} is drain bias.
3. Only at the V_{ON}, I_D of the FET is simulated based on TB approximations.
4. At the same V_{ON}, we calculate current ratio and get the modified effective mass in the y direction, m_Y^* by the following equation:

$$m_Y^* = m_y^* \times \left(\frac{I_{TB}|_{V_{ON}}}{I_{EM}|_{V_{ON}}}\right)^2 \tag{2.30}$$

   current ratio ($I_{\mathrm{TB}}|_{V_{\mathrm{ON}}}/I_{\mathrm{EM}}|_{V_{\mathrm{ON}}}$) can be larger or less than 1 since I_D–V_G curve of EM can be whether underestimated or overestimated than that of TB as shown in Figure 2.7 (c).
5. Effective mass in the x direction also should be changed maintaining DOS by the following equation:

$$m_{\mathrm{X}}^* = \frac{m_r^2}{m_{\mathrm{Y}}^*} \tag{2.31}$$

6. Simulate full I_D–V_G characteristics with new effective mass, m_{X}^* and m_{Y}^*

Electronic properties of monolayer $MoSe_2$ have been described by three-band TNN TB approximation [169], and EM approximation which is calculated by fitting following equation to the conduction band minima (CBM) valley along transport and transverse directions of band structure plotted by the TB approximations.

$$\mathrm{E} = \frac{\hbar^2 k^2}{2m^*} \tag{2.32}$$

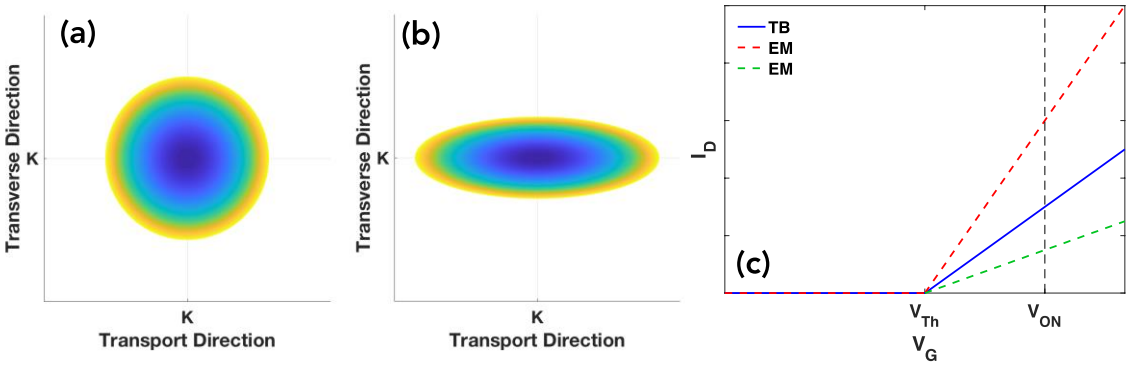

Figure 2.7 Top-view of paraboloids of approximated band structure at conduction band minima by effective mass method at *k* space with (a) original isotropic effective mass and (b) modified anisotropic effective mass. (c) Simplified I_D–V_G characteristics based on TB method (solid blue line), and overestimated (red dashed line) and underestimated (green dashed line) EM methods.

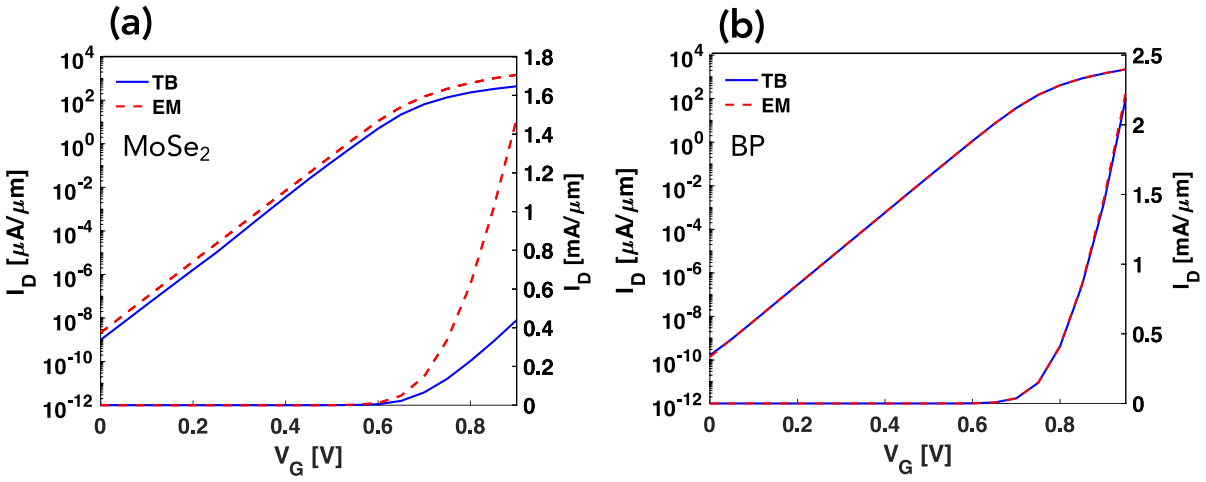

Figure 2.8 Linear and logarithmic I_D–V_G characteristics of monolayer (a) $MoSe_2$ and (b) black phosphorous FETs based on effective mass (red dashed curve) and tight-binding (blue solid curve) approximations

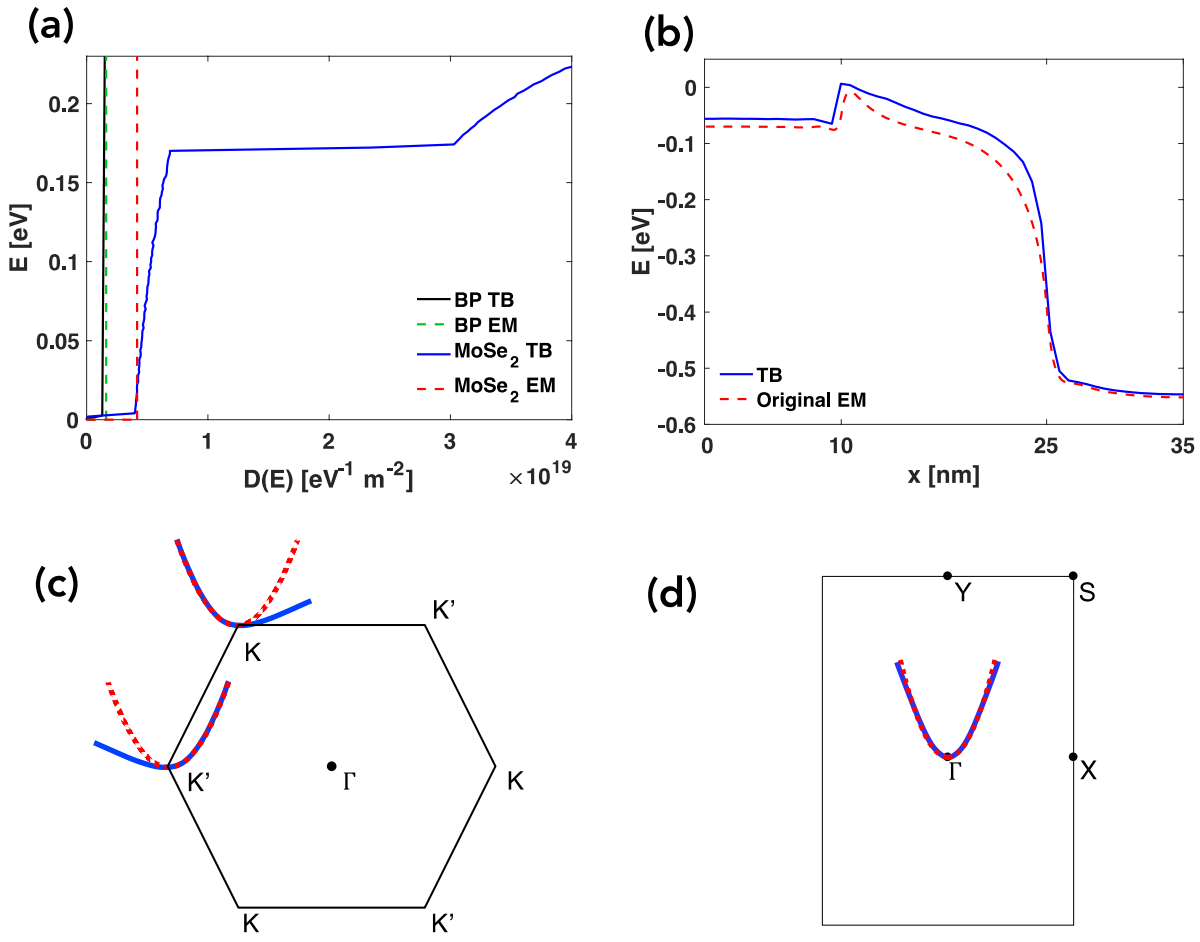

Figure 2.9 (a) Density-of-states of $MoSe_2$ and black phosphorous based on EM (dashed curve) and TB (solid curve). (b) Energy band diagram (E_C) of monolayer $MoSe_2$ FETs based on original effective mass and tight-binding methods. The first Brillouin zone of (c) $MoSe_2$ and (d) black phosphorous.

Band gaps of $MoSe_2$ in the both approximations are 1.43 eV. Carrier transport is calculated by the NEGF method based on TB, EM, and modified EM approximations, which is calculated iteratively with the Poisson's equation until both charge density and electrostatic reach self-consistence values [166]. For TB method along transverse direction, periodic boundary condition is applied and the charge and current are calculated by summing up all transverse modes along the direction considering grid spacing of the sub bands. Due to relatively short channel length, ballistic transport regime is assumed, ignoring scattering effect. In solving electrostatics, the Neumann boundary conditions are applied for the doped contacts (source and drain). The simulated nominal device structure has following parameters: active channel material is monolayer $MoSe_2$. Channel length and source/drain lengths are 15 nm and 10 nm, respectively. Gate oxide is 3.2-nm-thick HfO_2 ($\kappa = 25$) with double gate geometry. Power supply voltage of $V_{DD} = 0.5$ V is applied, and room temperature is assumed.

Results Figure 2.8 (a) shows transfer characteristics of monolayer $MoSe_2$ FET based on EM approximation which is compared with TB approximation counterpart. EM results in much higher both ON (V_{ON} = 0.85 V) and OFF current (V_{OFF} = 0.35 V) than TB by 308.2% and 213.3%, respectively. To check if the large difference in current is observed only for $MoSe_2$, same device simulations are followed with black phosphorous (BP) for active channel layer. As shown in Figure 2.8(b), transfer characteristics of BP based on EM is exactly matched with TB counterpart. This large current difference which can be observed in only $MoSe_2$ not BP is attributed to difference of DOS in EM and TB. Figure 2.9 (a) exhibits analytically calculated EM DOS ($= m^* S/2\pi\hbar^2$) and numerically calculated TB DOS from *E–k* band structure, for both materials. While DOS of BP is almost identical each other, that of $MoSe_2$ shows huge difference in EM and TB, especially energy range above 0.16 eV. Due to this difference, conduction band minima (E_c) potential profile by EM is deviated from that by TB as shown in Figure 2.9(b), meaning that TB needs more robust self-consistent effect to push down the potential profile due to larger DOS than that of EM. This is because the electronic states approximation with greater DOS requires more number of electrons in degenerately doped source and drain regions to widen the energy gap between electrochemical potential and conduction band minima ($\mu_{S/D} - E_C$).

Direction		Transport (Γ → K)	Transverse (near K)
$MoSe_2$	Original	0.4923	0.4984
	Modified	4.6728	0.0525
WTe_2	Original	0.2539	0.2567
	Modified	0.3830	0.1702

Table 2.2 Effective mass calculated by original and modified effective mass approximations for $MoSe_2$ and WTe_2. Unit is m_0, single electron mass.

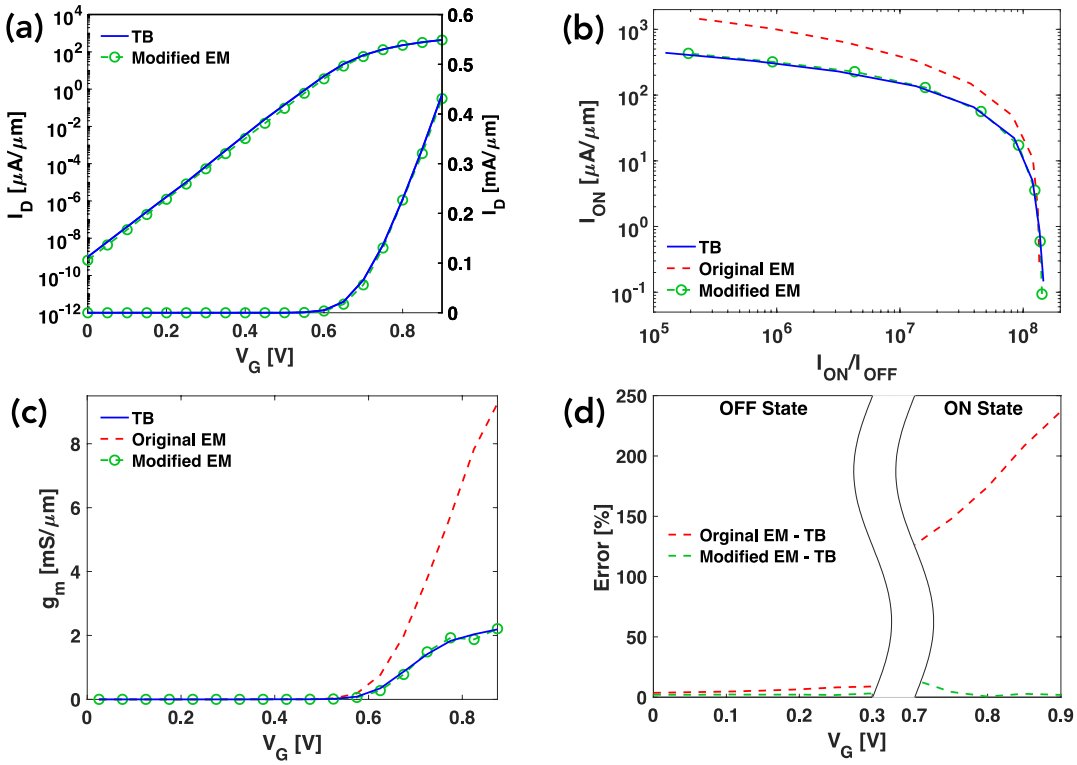

Figure 2.10 Transfer characteristics of $MoSe_2$ FETs. (a) Linear and logarithmic *I–V* characteristics with tight-binding (TB) and modified effective mass (EM) approximations. (b) I_{ON} as function of I_{ON}/I_{OFF} ratio, and (c) transconductance (g_m) with TB, original EM, modified EM. (d) Error of original EM and modified EM methods from TB method. TB, original EM, and modified EM methods are represented as blue solid curve, red dashed curve, and green dashed curve with circles, respectively, in (a), (b), (c), and (d).

Another origin that causes the current difference is deviated curvatures in the band structure. As you can see in the Figure 2.9(c), conduction band valleys of TMDs are located at K points and there are two full valleys within the 1st Brillouin zone (BZ). Since the conduction band valleys plotted by TB at the K points are not reflectional symmetric, EM value is extracted by fitting a parabola to the curvature only along transport direction not along opposite direction, resulting in inevitable discrepancy between the EM curve and the TB curve (K' point of Figure 2.9(c)). On the other hand, for BP, its curvature by EM can be well matched with TB counterpart because the conduction band valley is located at Γ point as shown Figure 2.9(d).

Table 2.2 includes original and modified EM for $MoSe_2$ and WTe_2 as result of the scheme that introduced in the simulation method. Figure 2.10(a) is transfer characteristics of $MoSe_2$ FETs based on TB and modified EM in Table 2.2. These two I_D–V_G curves are perfectly matched each other at both ON and OFF states. The overall performance of the device based on the two approximations can be evaluated by ON current (I_{ON}) vs. ON/OFF current ratio (I_{ON}/I_{OFF}) as shown in Figure 2.10(b). At common I_{ON} of 400 μA/μm, I_{ON}/I_{OFF} of original EM is 9.31×10^6 which is 43 times larger than that of TB, 2.14×10^5. However, I_{ON}/I_{OFF} of modified EM is 2.85×10^5 which is almost same as that of TB. This fact indicates that device simulation for carrier transport by modified EM can sufficiently reproduce transfer characteristics of $MoSe_2$ FETs by TB method. Transconductance, g_m, is plotted in Figure 2.10(c). Like I_{ON} vs. I_{ON}/I_{OFF}, g_m of modified EM is well matched with TB counterpart, which implies that ON state characteristics can be simulated with high accuracy by employing this scheme. To investigate how much accuracy has been enhanced, error of original EM and modified EM from TB were calculated. Error at ON state is calculated by $\text{Erorr} = (I_{EM} - I_{TB})/I_{TB} \times 100$, and error at OFF state was evaluated by logarithmic scale equation, $\text{Error} = (\log_{10} I_{EM} - \log_{10} I_{TB})/\log_{10} I_{TB} \times 100$ due to exponential variation of current. As shown in Figure 2.10 (d), while error of original EM is small having less than 10% at OFF-state, at ON-state, it is large within range of 130–240%. This large deviation of current can be significantly improved by using modified EM, giving error less than 5%.

Figure 2.11 (a) is conduction band potential profile of both original and modified EM. Those are perfectly matched each other due to same density-of-states effective mass. This indicates that self-consistent effects of both approximations are identical, however, it does not mean both gives same current. Due to reduced effective mas along transverse direction, electron transport of original EM is diminished to modified EM which is as much as that of TB as shown energy-resolved current spectrum Figure 2.11(b).

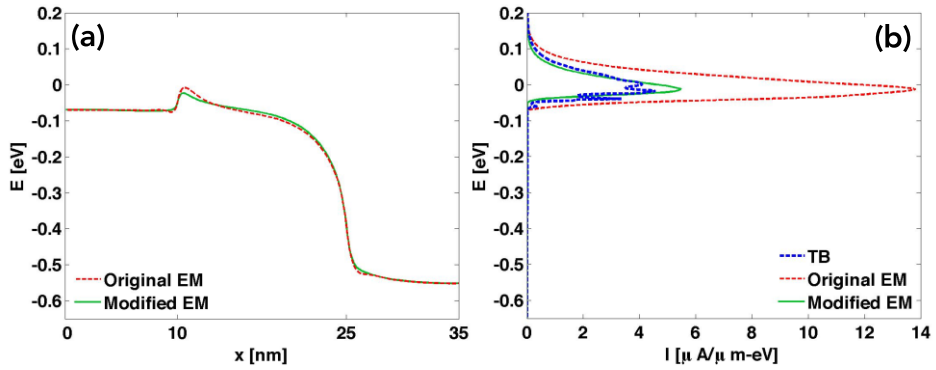

Figure 2.11 (a) Energy band diagram (E_C) of $MoSe_2$ FETs based on original (red dashed curve) and modified (green solid curve) EM methods, and (b) their corresponding energy-resolved current spectrums in addition to that by TB method (dashed blue curve).

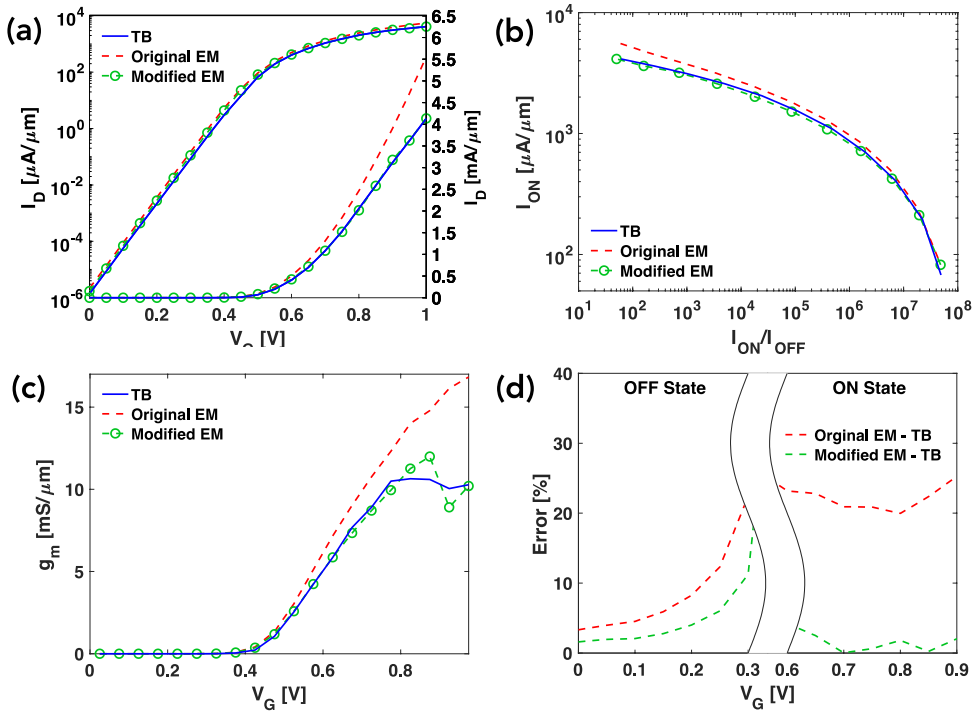

Figure 2.12 Transfer characteristics of WTe_2 FETs. (a) Linear and logarithmic *I–V* characteristics with tight-binding (TB), original, and modified effective mass (EM) approximations. (b) I_{ON} as function of I_{ON}/I_{OFF} ratio, and (c) transconductance (g_m) with TB, original EM, modified EM. (d) Error of original EM and modified EM methods from TB method. TB, original EM, and modified EM methods are represented as blue solid curve, red dashed curve, and green dashed curve with circles, respectively, in (a), (b), (c), and (d).

This scheme can be further expanded to other types of TMDs material where energy band valleys are located at K points thereby EM approximation results in deviation of current calculation from TB approximation. As an instance of TMDs, WTe_2 was chosen for device simulation. Like $MoSe_2$ case, I_D–V_G and I_{ON} vs. I_{ON}/I_{OFF} of modified EM are exactly overlapped with those of TB as shown in Figure 2.12(a)(b). Figure 2.12(c) displays g_m of the modified EM, which is well matched with that of TB at the V_G less than 0.8 V. Due to numerical convergence limitations of ballistic transport NEGF simulations at high V_G, a few unmatched g_m points can be observed at V_G above 0.8 V. Errors of EM approximations are also calculated in Figure 2.12 (d). Errors of original EM, which is calculated from Figure 2.12(a), are improved by modified EM at ON state from ~25% to ~1%.

In summary, a scheme for enhancing accuracy of current calculation in TMD FETs simulations based on EM approximation is introduced. Even though EM approximation gives highly quick simulation procedure, it gives low accuracy for current calculation. By maintaining density-of-states effective mass and modifying transverse direction effective mass, m_y^*, the simulated current can be improved analytically with accuracy as much as TB approximation. There are two origins causing the inaccuracy of EM approximation for TMDs FETs simulation: 1) too simplified DOS and 2) insufficient description of energy band structure by EM method. This was explained by DOS and E–k band structure of BP and $MoSe_2$. With modified EM, $MoSe_2$ and WTe_2 FETs simulations were done revealing that this scheme can exactly reproduce TB simulation in transfer characteristics, I_{ON} vs. I_{ON}/I_{OFF}, g_m, and energy resolved current spectrum. Not only high accuracy and fast simulation time, one of the benefits of this scheme is that it can be applied to any 2D materials which give large difference in current calculation in case that either EM current is larger or smaller than TB current.

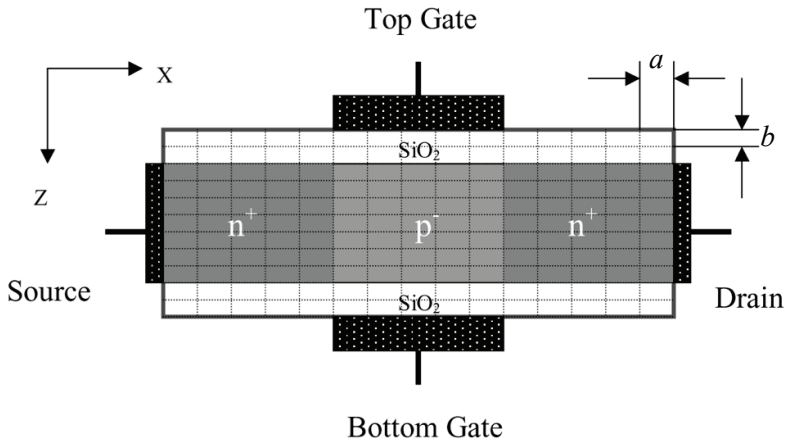

Figure 2.13 Geometry of a thin body double-gate FET. Simulation calculates only a region enclosed by the solid line. *a* and *b* are spatial constants along the X and Z directions, respectively [165].

2.2 Electrostatics

In this section, we will cover how to solve the Poisson's equation numerically by considering general 2D Poisson solver based on the FDM and by applying it to a double-gate MOSFET as an example. Figure 2.13 is the device structure used in this section for the solution.

The following equation is the Gauss's law for any electrostatic system

$$\nabla \cdot \vec{D}(\vec{r}) = \rho(\vec{r}) \tag{2.33}$$

where $\vec{D}$, $\vec{r}$ and ρ, are the electric flux density, position vector ($\vec{r} = x\hat{x} + y\hat{x} + z\hat{z}$), and charge density function, respectively. This expression can be converted to a generalized form of the Poisson's equation by substituting constitutive relation $\vec{D}(\vec{r}) = \varepsilon_0 \varepsilon(\vec{r}) \vec{E}(\vec{r})$ and electric field $\vec{E}(\vec{r}) = -\nabla V(\vec{r})$ assuming uniform dielectric function with the form $\varepsilon(\vec{r}) = \varepsilon_r$

$$\nabla^2 V(\vec{r}) = -\frac{\rho(\vec{r})}{\varepsilon_0 \varepsilon_r} \tag{2.34}$$

where ε_r, ε_0, and $V(\vec{r})$ is dielectric constant, permittivity of free-space, and potential function, respectively. Figure 2.13 has mesh inside where grid of spatial points, [m, n] and potential functions, $V_{m,n}$ are located at the point. Let *a* and *b* be mesh spacings in the X and Z directions, respectively. There are total $N_X \times N_Z$ lattice nodes in the integration range of the Poisson's equation, where N_X and N_Z are

the number of nodes in the X and Z directions, respectively. Since the $N_X \times N_Z$ equations are required to get the same number of unknowns, Equation (2.34) is converted to get the equations for all internal nodes, while equations for boundary nodes are obtained using boundary conditions, either Neumann or Dirichlet. For illustrating one node [m, n] (row m and column n) in internal nodes, the FDM is used for the spatial derivatives. Next, the Poisson's equation is to be expanded by the partial derivatives:

$$\frac{\partial^2 V_{m,n}}{\partial x^2} + \frac{\partial^2 V_{m,n}}{\partial z^2} = -\frac{\rho_{m,n}}{\varepsilon_0 \varepsilon_r} \tag{2.35}$$

where $\rho_{m,n}$ is charge density at node [m, n].

Along the x and z directions, the left-hand side of the Equation (2.35) becomes

$$\frac{\partial^2 V_{m,n}}{\partial x^2} + \frac{\partial^2 V_{m,n}}{\partial z^2} \approx \frac{V_{m,n+1} - 2V_{m,n} + V_{m,n-1}}{a^2} + \frac{V_{m+1,n} - 2V_{m,n} + V_{m-1,n}}{b^2} \tag{2.36}$$

Plugging the equation into Equation (2.35) gives us

$$\begin{aligned} &\frac{a}{b}V_{m-1,n} + \frac{b}{a}V_{m,n-1} - 2\left(\frac{a}{b} + \frac{b}{a}\right)V_{m,n} + \frac{b}{a}V_{m,n+1} + \frac{a}{b}V_{m+1,n} \\ &= -\frac{ab}{\varepsilon} q(n - p + N_D - N_A)_{m,n} \end{aligned} \tag{2.37}$$

Where right-hand side, $\rho_{m,n} = q(n - p + N_D - N_A)_{m,n}$, considers electron/hole charge and doping concentration on the nodes. In simulation work in Chapter 5, N_D, and N_A are assumed to be zero due to practical difficulty of doping on 2D materials. Then, we solve for $V_{m,n}$ to find

$$\begin{aligned} V_{m,n} = \frac{ab}{2(a^2 + b^2)}\Big[&\frac{a}{b}V_{m-1,n} + \frac{b}{a}V_{m,n-1} + \frac{b}{a}V_{m,n+1} + \frac{a}{b}V_{m+1,n} \\ &+ \frac{ab}{\varepsilon} q(n - p + N_D - N_A)_{m,n}\Big] \end{aligned} \tag{2.38}$$

For node [m, n] in oxide/channel interface, $\varepsilon = \varepsilon_{ox}/\varepsilon_{ch}$. For the nodes located at the interface, Equation (2.37) becomes

$$\begin{aligned} &\frac{a}{b}V_{m-1,n} + \frac{b}{2a}\left(1 + \frac{\varepsilon_{Bot}}{\varepsilon_{Top}}\right)V_{m,n-1} - \left(\frac{a}{b} + \frac{b}{a}\right)\left(1 + \frac{\varepsilon_{Bot}}{\varepsilon_{Top}}\right)V_{m,n} + \frac{b}{2a}\left(1 + \frac{\varepsilon_{Bot}}{\varepsilon_{Top}}\right)V_{m,n+1} \\ &+ \frac{a}{b}\frac{\varepsilon_{Bot}}{\varepsilon_{Top}}V_{m+1,n} = -\frac{ab}{\varepsilon_{Top}} q(n - p + N_D - N_A)_{m,n} \end{aligned} \tag{2.39}$$

where ε_{Top} and ε_{Bot} are dielectric constants for the materials above the interface and below the interface [165]. Equations (2.37) and (2.39) indicate that one $V_{m,n}$ is determined by only charge at [m, n] node and the voltage at the four nearest neighbors around it. Figure 2.14 exhibits graphical depiction of these nodes, which is called the computational molecule.

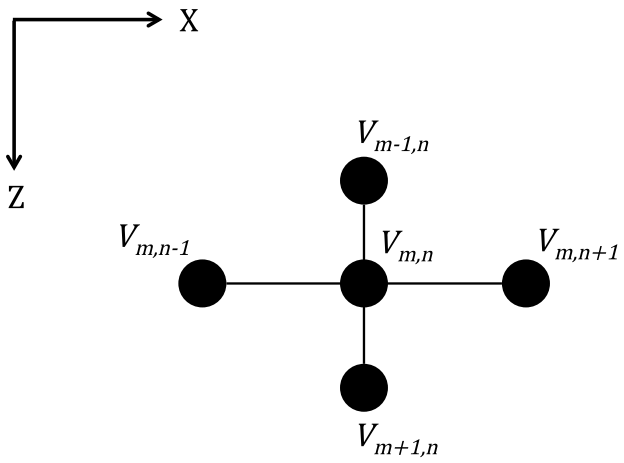

Figure 2.14 A computational molecule for the five-pointed star [172].

Next, the equations for all boundary nodes will be considered. Two of the most common forms of boundary conditions are the Dirichlet and the Neumann boundary conditions. The former can be written as

$$V(r) = f(r) \qquad (r \in \Omega_D) \tag{2.40}$$

where the Ω_D is the set of all nodes which satisfy the Dirichlet condition [172]. This condition forces specific points on the grid to be the potential function, $f(r)$. At the gate contact in our example, substituting Ω_D with a set of nodes at the interface between the gate electrode and the oxide, the numerical equation can be easily written as,

$$V_{m,n} = V_G \tag{2.41}$$

where V_G is the gate bias voltage.

On the other hand, if the derivative of the potential function with respect to the outward unit normal vector to the boundary is known, the Neumann boundary condition can be used, which is defined as

$$\frac{\partial V(r)}{\partial \mathbf{n}} = f'(n) \quad (r \in \Omega_N) \tag{2.42}$$

where **n** is the surface unit normal vector, and f' is the set of known derivatives [172]. The left-hand side is called the normal derivative. This boundary condition enables the contact potentials to be correct values that satisfy charge neutrality in the contact regions. Fixing the known derivatives, f' to 0.0 V/m in our case [165],

$$\begin{aligned} &V_{m,n} - V_{m\pm1,n} = 0 \text{ for the top and bottom edges,} \\ &V_{m,n} - V_{m,n\pm1} = 0 \text{ for the left and right edges,} \\ &2V_{m,n} - \left(V_{m+1,n} + V_{m,n\pm1}\right) = 0 \text{ for the two corner nodes along the top edge, and} \\ &2V_{m,n} - \left(V_{m-1,n} + V_{m,n\pm1}\right) = 0 \text{ for the two corner nodes along the bottom edge.} \end{aligned} \tag{2.43}$$

At the boundaries except gate and source/drain contacts, we assume the same zero electric field condition.

Now, the solution over the all voltage node $V_{m,n}$ can be represented as a simple matrix-vector equation since the node is just linearly dependent on its four nearest neighbors as shown Equations (2.37) and (2.38). By building vector **x** to contain all of the voltage samples within the domain [172]:

$$\mathbf{x} = [V_{1,1} \quad V_{1,2} \quad V_{1.3} \quad \dots \quad V_{m,n-1} \quad V_{m,n} \quad V_{m,n+1} \quad \dots \quad V_{N_Z,N_X}]^T \tag{2.44}$$

we can write the entire problem as a matrix-vector equation form:

$$\mathbf{Ax} = \mathbf{b} \tag{2.45}$$

where **b** is a vector containing all the information about any charge densities and boundary conditions. Solution vector **x** can be finally calculated by obtaining the matrix **A**.

$$\mathbf{x} = \mathbf{A}^{-1}\mathbf{b} \tag{2.46}$$

Among various numerical methods to obtain inverse of the large size matrix **A**, lower–upper (LU) decomposition was used for the simulation which will be introduced for next chapters.

Chapter 3 Analysis on Trap States in *p*-type $MoSe_2$ Phototransistors

3.1 Introduction

As introduced in the Chapter 1, TMDs have been used for various applications these days from switching to sensing devices. In particular, TMDs are intriguing for optoelectronic devices due to the large photoresponsivity in the monolayer form. On the other hand, it is known that the photoillumination effects of multilayer TMDs have been significantly limited due to its inherent indirect band gap. For instance, monolayer MoS_2 phototransistors showed a photoresponsivity of 880 A/W [142] whereas multilayer MoS_2 devices have shown much lower photoresponsivity in the order of 100 mA/W [136], [137], even though they can provide high field-effect mobility ($> 100\ \mathrm{cm^2/V \cdot s}$) and good subthreshold swing (~70 mV/decade) [130], [173]. An advanced local-gate device geometry was adapted for multilayer MoS_2 phototransistors to enhance the photoresponsivity [174]. Nevertheless, multilayer TMDs have clear advantages over their monolayer counterparts for practical applications. For example, multilayer MoS_2 has three times the higher density-of-states than that of monolayer MoS_2, which can produce extensively large current in a ballistic regime [136], [175]. In a scattering regime, driven current is also boosted due to multiple conducting channels created by field-effects in multilayer MoS_2. Moreover, multilayer MoS_2 provides a wider spectral response than that of monolayer MoS_2 − from ultraviolet (UV) to near infrared (NIR) wavelengths − due to its narrower band gap, which can be advantageous in a variety of photodetector applications [176].

Furthermore, multilayer TMDs are suitable for large-area production which can be processed by CVD. At the early stage of investigation on exotic electronic and mechanical properties of TMDs, atomically thin flakes were prepared by using scotch tape assisted exfoliation or electrochemical intercalation from pristine bulk crystals [177]–[179]. However, several critical issues remain ahead before such TMD flakes are integrated into complex circuits, since large-area coverage and systematic control of the film thickness are not offered by the above methods. Thus, in order to implement their attractive properties into a large-area integrated circuit, reproducible large-area production of 2D layered semiconductors is necessary. Recently, there are some reports on the thermal CVD of large-area multilayer MoS_2 [180]–[182]. Among several TMDs materials, I and my collaborators chose $MoSe_2$ as a semiconducting material due to its own advantageous properties. One of the advantages of $MoSe_2$ over MoS_2 is a higher photoresponsivity in solar spectrum range compared to that of MoS_2 due to the higher optical absorption of the material [115] due to the quantum confinement effect during the

band gap transition [183], which implies that the advanced device structure may not be required for $MoSe_2$ phototransistors to achieve high sensitivity.

In this regard, multilayer $MoSe_2$ thin-film phototransistors were fabricated by using CVD by Kim *et. al* in Sungkyunkwan University. Then, device performance of CVD-grown multilayer $MoSe_2$ TFTs is explored by temperature-dependent analysis which extracts density of sub-gap states. The active channel layer was grown by CVD for large-area device production and, optical characteristics of the fabricated devices demonstrated large photoresponsivity (93.7 A/W) and reasonably large field-effect mobility ($\sim 10\ \mathrm{cm}^2/\mathrm{V}\cdot\mathrm{s}$), which could be due to existence of trap state in the band gap.

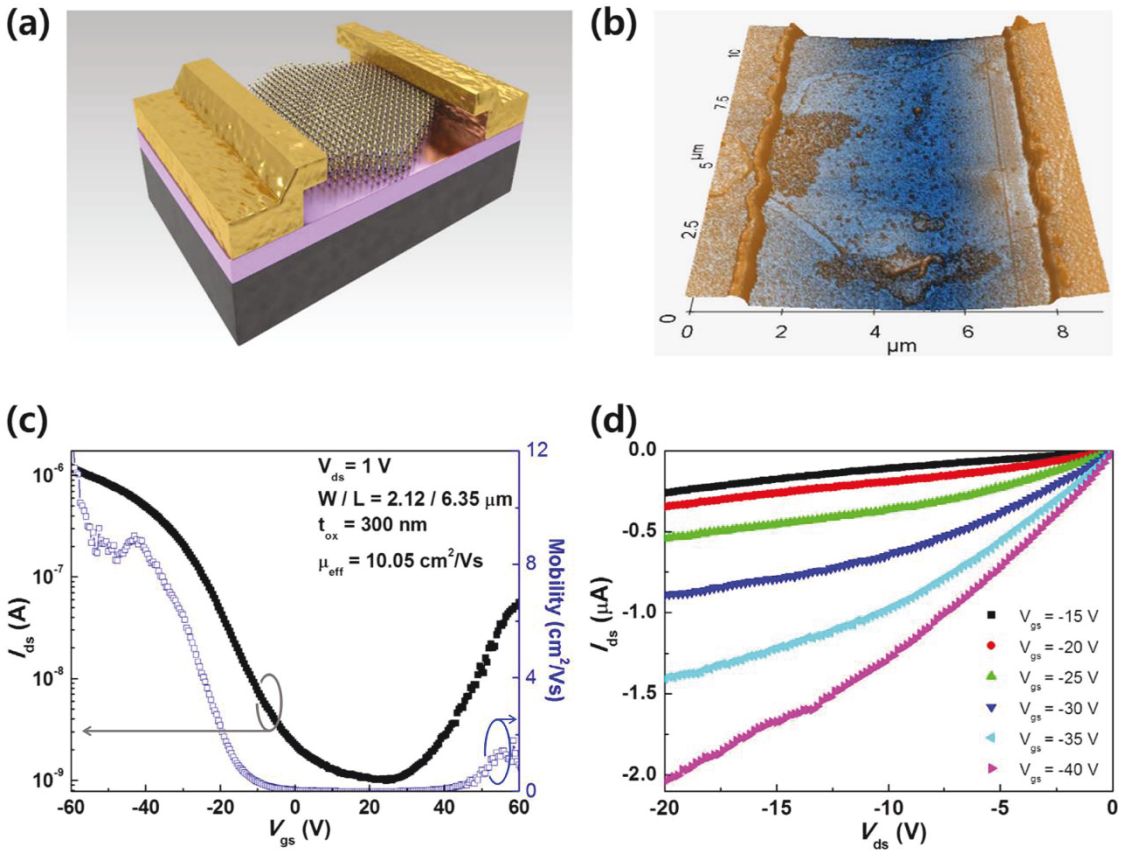

Figure 3.1 Thin-film transistor based on the CVD-grown multilayer $MoSe_2$. (a) A 3D schematic structure for TFT based on multilayer $MoSe_2$ film. (b) A 3D topography AFM image of the hexagonal $MoSe_2$ TFT with a channel length of 6.35 μm. (c) Transfer characteristics (I_{DS}–V_{GS}) and field-effect mobility (μ_{eff}) of the $MoSe_2$ TFT as function of gate bias (–60 ≤ V_{GS} ≤ 60 V at V_{DS} = 1 V). (d) Output characteristics of the respective device (–20 ≤ V_{DS} ≤ 0 V, –40 ≤ V_{GS} ≤ 15 V in steps of 5 V).

3.2 Experimental Results and Theoretical Analysis

Experimental fabrication, measurement, and characterization in this chapter were done by my collaborators, Chulseung Jung, Hyunseong Moon, Young Ki Hong, Jozeph Park, Seung Min Kim, Junyeon Kwon, and Inturu Omkaram in Professor Sunkook Kim's group in Sungkyunkwan University. Figure 3.1(a) shows a three-dimensional (3D) schematic of the fabricated $MoSe_2$ TFT device. The electrodes are composed of Ti as an adhesion layer and Au. Figure 3.1(c) is measured transfer characteristics (I_{DS}–V_{GS}) of the device and extracted mobility (μ_{eff}) values are plotted as function of same V_{GS} range. μ_{eff} was calculated using the following relationship; $\mu_{eff} = g_m L/(WC_{OX}V_{DS})$, where L is the channel length (~6.35 μm), W is the channel width (~2.12 μm), C_{OX} is the capacitance of the gate insulator per unit area, and V_{DS} the applied drain-source voltage (1 V). The maximum transconductance, g_m, is approximately 54 μS. The devices have predominant *p*-type characteristic with ambipolar behavior, with the highest μ_{eff} being approximately 10 $cm^2/V \cdot s$ and an ON/OFF current ratio of ~10^3. The output characteristics (I_{DS}–V_{DS}) (Figure 3.1(d)) was measured in the negative V_{DS} range, which also displays clear *p*-type behaviors.

It is noteworthy that the characteristics of $MoSe_2$ TFTs is *p*-type, although *n*-type behavior is common for $MoSe_2$ TFTs in most recent studies [184], [185]. Here, it is hypothesized that the band structure of as-grown multilayer $MoSe_2$ is varied by a large density of trap sites created by an annealing process during the CVD growth. A recent study reported that anion vacancies in TMDs such as MoS_2, $MoSe_2$, and WSe_2 can be generated by irradiation with thermal annealing at sub-decomposition temperature (~600 °C) [53]. Analogously, since our decomposition temperature (~650 °C) was reached after the CVD growth for 10 min, we can expect that Se vacancies was possibly generated in the multilayer $MoSe_2$. Such defects may also significantly affect the electrical behavior through Fermi level pinning at the interface between the source/drain metal lead and the $MoSe_2$, making the theoretical model of the Schottky barrier height ($\Phi_{Bn} = \Phi_m - \chi$, where Φ_m and χ are the metal work function and the semiconductor's electron affinity, respectively) incorrect prediction [186], [187].

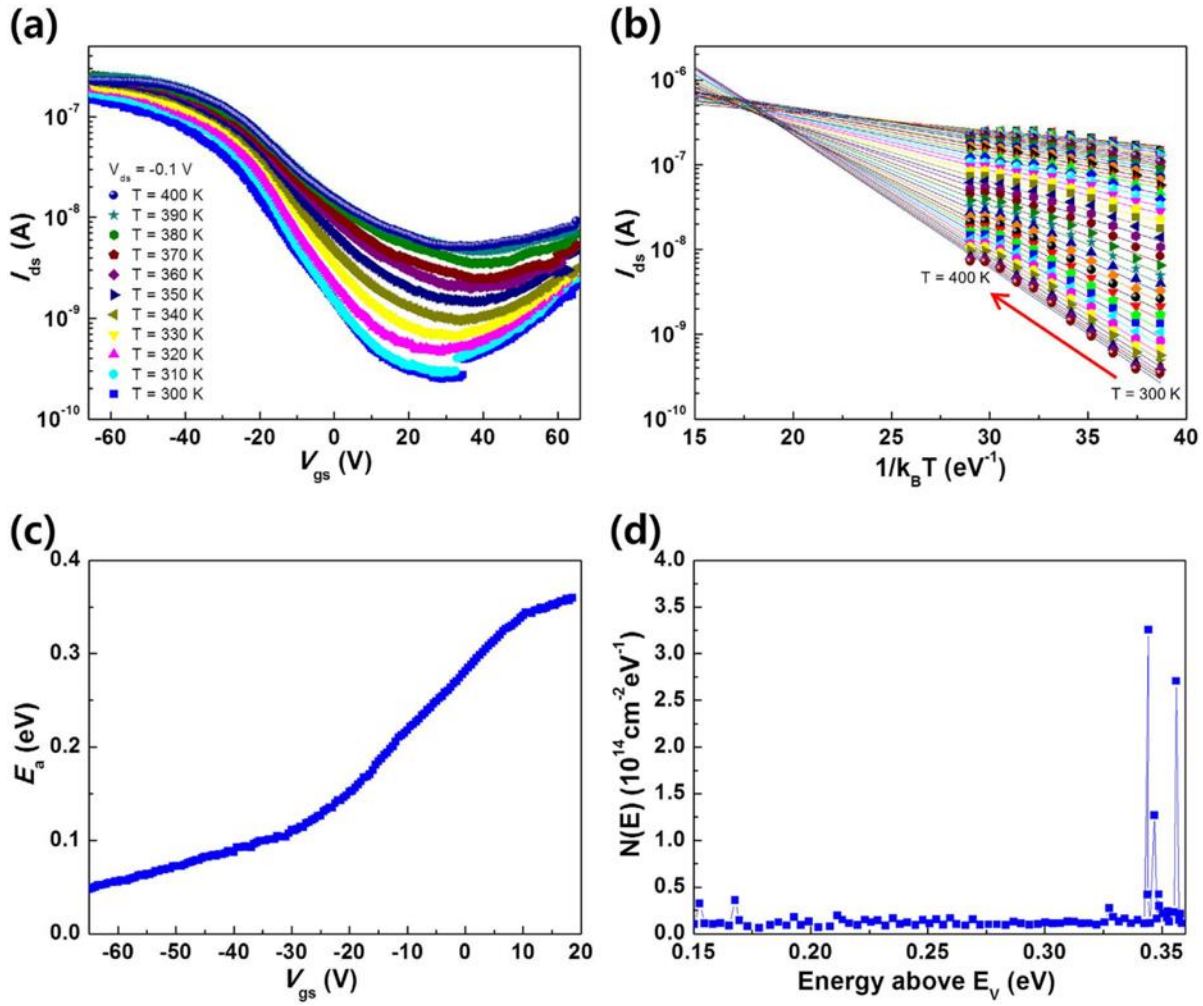

Figure 3.2 Temperature-dependent behavior and density-of-state measurement according to the Meyer–Neldel rule. (a) Transfer characteristics with temperatures from 300 to 400 K in steps of 10 K at V_{DS} = 0.1 V. (b) Temperature dependence of the drain current (I_{DS}) as a function of $1/k_BT$. (c) Activation energy (E_a) extracted using the Meyer–Neldel rule as a function of gate voltage. (d) Density of sub-gap states calculated for the *p*-type $MoSe_2$ TFT as a function of energy above the valence band (E_V). A large density can be observed ~ 0.35 eV above E_V

In order to extract the sub-gap states, a temperature-dependent analysis was performed [188], [189]. Figure 3.2(a) shows the $I_{DS} - V_{GS}$ characteristics at different temperatures between $T = 300$ and 400 K. Figure 3.2(b) depicts the thermally activated current at different V_{GS} values, as a function of $1/k_BT$ (where k_B is the Boltzmann constant). The Arrhenius equation is used to describe the current response to the temperature as $I_{DS} = I_{DS,0}\exp(-E_a/k_BT)$, where $I_{DS,0}$ is a prefactor and E_a is the activation energy [188]. The variation of E_a at different gate voltages is shown in Figure 3.2(c), from which the density of sub-gap states can be obtained by $N(E) = (C_{ox}/q)(\partial E_a/\partial V_{GS})^{-1}$, where q is the elementary charge. Figure 3.2(d) shows a large density of sub-gap states in the band gap near $E_V + 0.35$ eV (E_V being the valence band maximum), which is 0.07 – 0.2 eV below the midgap energy (E_m), since the band gap of bulk $MoSe_2$ is reported to be 0.84 – 1.1 eV [183], [190], [191]. Therefore, at the Ti/Au metal–$MoSe_2$ junction, Fermi level pinning [192] caused by the gap states is expected to occur in such a way that the Schottky barrier height for holes becomes smaller ($\Phi_{Bp} \approx E_g/2 - 0.14$ eV) than that for electrons ($\Phi_{Bn} \approx E_g/2 + 0.14$ eV), resulting in p-type-dominant ambipolar behavior as shown in Figure 3.2(c).

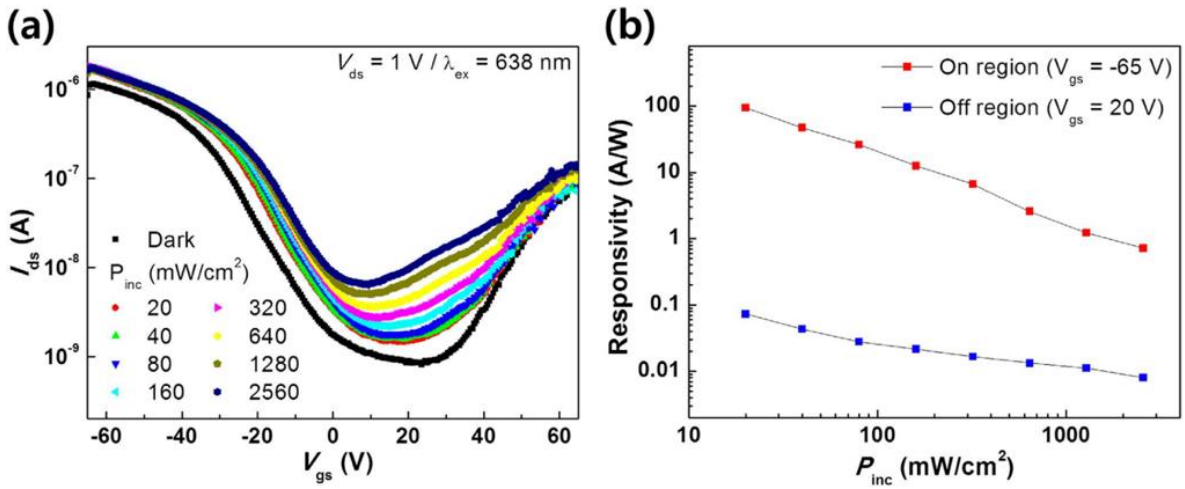

Figure 3.3 Photoresponsive behavior of multilayer $MoSe_2$ TFT. (a) Comparison of transfer characteristics (I_{DS}–V_{GS}) in the dark and under illumination with varying optical power densities. (b) Responsivity of the device as a function of the same optical power densities used in (a) in logarithmic scale in the ON (V_{GS} = –65 V) and OFF (V_{GS} = 20 V) regions.

Now, the photoresponse of the TFTs were measured to explore the optoelectronic properties of multilayer $MoSe_2$ by my collaborators. Transfer characteristics under illumination of 638 nm wavelength as function of V_{GS} at various incident power intensities (from 20 to 2,560 $\mathrm{mW/cm^2}$) are shown in Figure 3.3(a). V_{DS} is 1 V. One of the most significant figure of merits is photoresponsivity defined as $R = I_{ph}/P_{inc}S$, where $I_{ph}(= I_{total} - I_{dark})$ is the photo-induced photocurrent, S is the channel area of the device, and P_{inc} $(\mathrm{W/cm^2}) = P_{tot}/A_{laser}$ (A_{laser} is the area of laser spot) is the incident power density. Figure 3.3(b) depicts dependence of photoresponsivity on incident power density. Photoresponsivity is maximized ($R = 93.7$ A/W) at $V_{GS} = -65$ V with the lowest incident power density. Remarkably, the R is significantly high value for $MoSe_2$ TFTs, considering that the channel layers were grown by CVD. It is also comparable to mechanically exfoliated $MoSe_2$ TFT counterpart [142], [193]–[195]. Recently, it was reported that photoresponsive properties of TMDs were enhanced by the trap sites related to the anion vacancies which correspond with energy levels located in band gap. Large density of sub-gap states in as-grown multilayer $MoSe_2$ was calculated by our temperature-dependent measurements (Figure 3.2), which can be the key cause of the large photoresponsivity.

3.3 Conclusion

We investigated to find origin of the *p*-type behavior and high photoresponsivity of phototransistors based on CVD-grown $MoSe_2$ multilayers. It turns out there are intense density of sub-gap states in as-grown multilayer $MoSe_2$. The special growth method for $MoSe_2$ by CVD was supposed to induce Se vacancies in $MoSe_2$. Such defects are believed to be the origin of the observed ambipolar conduction in our multilayer $MoSe_2$ TFTs, through the Fermi level pinning at the metal-$MoSe_2$ semiconductor interface. This was confirmed by large density-of-states in band gap, measured and calculated by temperature-dependent analysis. Furthermore, enhanced photoresponsivity of 93.7 A/W were shown, indicating that the boosted photoresponsivity is due to the Se vacancies and corresponding quantified large amount of the gap-states in the multilayer $MoSe_2$. However, mechanism coupling the large density-of-states and the high photoresponsivity is still unclear. Thus, further theoretical investigation such as analytical modeling or numerical simulation might be required for in-depth understanding for underlying physics of the optical behaviors of the $MoSe_2$ phototransistors.

Chapter 4 Models for Optical Properties of $MoSe_2$ Phototransistors

4.1 Introduction

In the previous chapter, I introduced important advantages of multilayer TMDs phototransistors over monolayer counterparts in terms of large density-of-states, multiple conducting channels, and wider spectral response. In this regard, the multilayer $MoSe_2$ phototransistors were fabricated by CVD which is able to provide large-area production of 2D layered semiconductors unlike scotch tape exfoliation method. The device performance exhibited *p*-type semiconducting behaviors, and large density of in-gap states were extracted from the channel material to analyze the behaviors. In addition, large photoresponsivity was characterized, which could be attributed to the existence of the large density-of-states in the band gap. However, clear relation between the trap states and the large optical gain is still missing. In this chapter, the main mechanisms to boost the photoresponsivity of the multilayer $MoSe_2$ phototransistors is investigated by analytical modeling. The devices used in this chapter were fabricated through CVD under Mo-rich condition by same collaborator introduced in the previous chapter. The CVD-grown multilayer $MoSe_2$ phototransistors exhibit significantly larger photoresponsivity than naturally obtained multilayer TMDs phototransistors by orders of magnitude. This was successfully analyzed by physically modeling two main photoillumination effects; photoconductive (PC) and photogating (PG) effects.

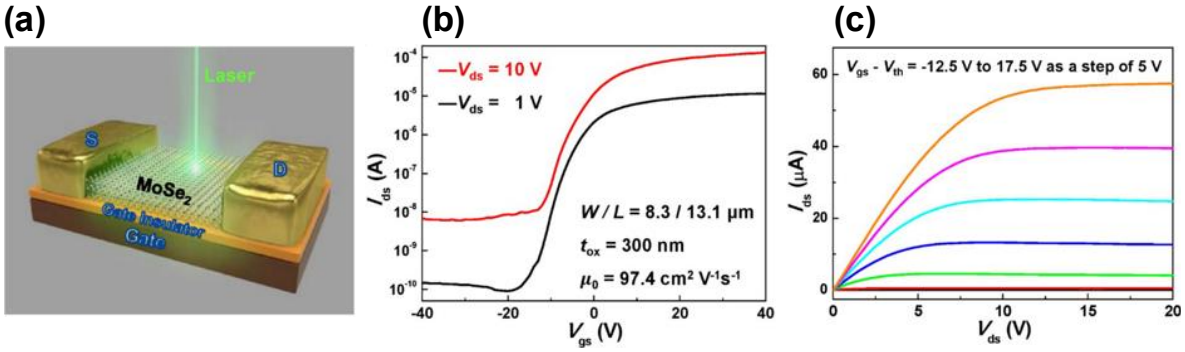

Figure 4.1 (a) A device structure of a CVD-grown multilayer $MoSe_2$ phototransistor. (b) Transfer (I_{DS}–V_{GS}) characteristics of the (a) at V_{DS} = 1 V (black) and 10 V (red). (c) Output characteristics (I_{DS}–V_{DS}) of (a)

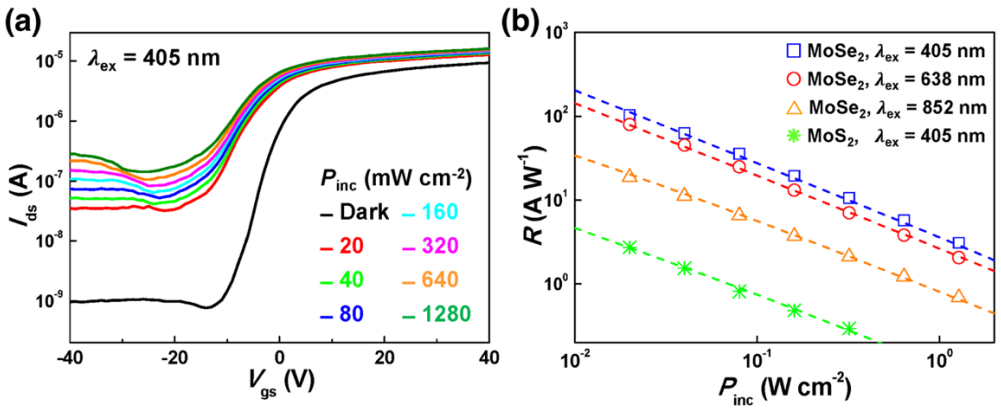

Figure 4.2 Photoresponsive characteristics of synthetic $MoSe_2$ and natural MoS_2 phototransistors. (a) Transfer characteristics (I_{DS}–V_{GS}) of a $MoSe_2$ phototransistor with dark and illumination conditions. Its wavelength and incident optical densities are 405 nm and range of 20 to 1,280 mW/cm^2, respectively. (b) Comparison between measured (open symbols) and modeled (dashed lines) photoresponsivity (R) as a function of P_{inc} with varying wavelengths (405, 438, and 852 nm) for $MoSe_2$ phototransistor, and with a wavelength of 405 nm for MoS_2 phototransistor (stars and green dashed line). A maximum value in the curve for $MoSe_2$ phototransistors is 103.1 A/W at P_{inc} = 20 mW/cm^2 and λ_{ex} = 405 nm.

4.2 Experiments

Like Chapter 3.2, all fabrications, measurements, and characterizations introduced in this chapter were conducted by my collaborators, Junyeon Kwon, Seongin Hong in Professor Sunkook Kim's group in Sungkyunkwan University. The multilayer $MoSe_2$ was grown by atmospheric pressure chemical vapor deposition (APCVD) in Mo-rich condition. My collaborator clearly observed distinct interstitial atoms from aberration corrected high-resolution transmission electron microscopy (HRTEM) image. Each layer is stacked following the ABABAB sequence, which is consistent with the X-ray diffraction (XRD) and Raman spectroscopy analyses, confirming that the whole APCVD-grown $MoSe_2$ has a 2H hexagonal structure. A total of 5 layers of 2H stacking structure are clearly identified with braces and corresponding italicized characters, and a couple of interstitial atoms were found between a- and b-layers and also another group of interstitials between b- and c-layers. The collaborator confirmed that the interstitials observed by the aberration corrected HRTEM images are Mo atoms through density functional theory (DFT). In this regard, it can be hypothesized that the Mo-interstitials might be the key origin of the large photoresponsivity of the multilayer $MoSe_2$ phototransistors.

A schematic structure for the synthetic CVD-grown multilayer $MoSe_2$-based phototransistor is shown in Figure 4.1(a). First, device characteristics in dark were investigated by measuring current–voltage characteristics at V_{DS} = 1 V (black) and 10 V (red) shown in Figure 4.1(b). It shows a clear *n*-type behavior with a large ON/OFF current ratio (I_{ON}/I_{OFF}) of ~10^5 and a large mobility of 97.4 $cm^2/V \cdot s$. Figure 4.1(c) is the measured output characteristics (I_{DS}–V_{DS}) of our device for gate voltages (V_{GS}) from –20 to 10 V. The curve shows a linear region at low V_{DS}, indicating Ohmic contact between $MoSe_2$ and source/drain (S/D) contacts.

Illumination effects on the transfer characteristics of the multilayer $MoSe_2$ TFT at V_{DS} = 1 V is shown in Figure 4.2(a). Incident optical power densities, P_{inc}, is ranged from 20 to 1,280 mW/cm^2 at an excitation wavelength (λ_{ex}) of 405 nm. Under light illumination of P_{inc} = 1,280 mW/cm^2, both the ON and OFF currents are greatly amplified from the dark state by 0.5 and 2.5 orders of magnitude, respectively. Figure 4.2(b) shows the photoresponsivity, *R*, the ratio of photocurrent to the incident power, as a function of the incident optical power densities at λ_{ex} = 405, 638, and 852 nm (square, circle and triangle symbols, respectively). The maximum photoresponsivity is 103.1 A/W at P_{inc} = 20 mW/cm^2 and λ_{ex} = 405 nm, which is larger than that of multilayer MoS_2 phototransistors where the semiconductor material is obtained by mechanical exfoliation approach from natural bulk MoS_2. (green star in Figure 4.2(b)) by ~ 40 times.

4.3 Modeling

The observation of the large photoresponsivity led us to consider influence of the Mo-interstitials on the large current, and investigate the mechanisms of photoillumination effects. The photocurrent can be categorized by two groups: photoconductive (PC) effect ($I_{ph,PC}$) and photogating (PG) effect ($I_{ph,PG}$). PC effect is induced by increased conductivity of the channel material due to photo-induced excess carriers, which are generated electron-hole pairs under light illumination. The consequent photocurrent is calculated in a classical manner as

$$I_{ph,PC} = \left(\frac{W}{L}\right) V_{DS} \Delta\sigma \tag{4.1}$$

where W, L, V_{DS}, and $\Delta\sigma$ are the width and length of the device, source-drain voltage, and conductivity increase due to light illumination, respectively [196].

On the other hand, PG effect is due to a threshold voltage shift under illumination, which can be expressed as $I_{ph,PG} = g_m \Delta V_{th}$ where g_m is transconductance in the dark and ΔV_{th} is the threshold voltage shift caused by accumulated or trapped holes and barrier lowering [197]. The accumulation is attributed partly to the presence of the source-channel junction which obstructs the flow of excess holes into the source in the valence band. On the contrary, excess electrons in the conduction band can easily move from the channel to the drain. In addition, trap states can capture the excess holes, resulting in the suppressing of the potential barrier and the promotion of electron injection from the source, as shown in Figure 4.3.

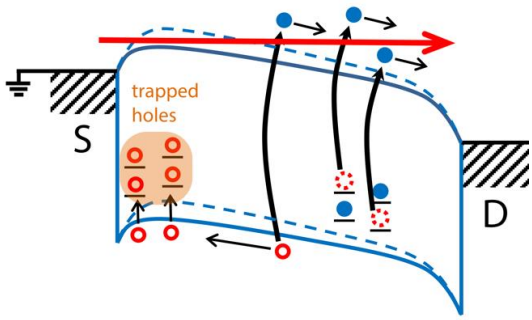

Figure 4.3 A schematic energy band profile, referring the mechanism of the photogating (PG) effect. Electrons and holes are denoted by filled and open circles, respectively.

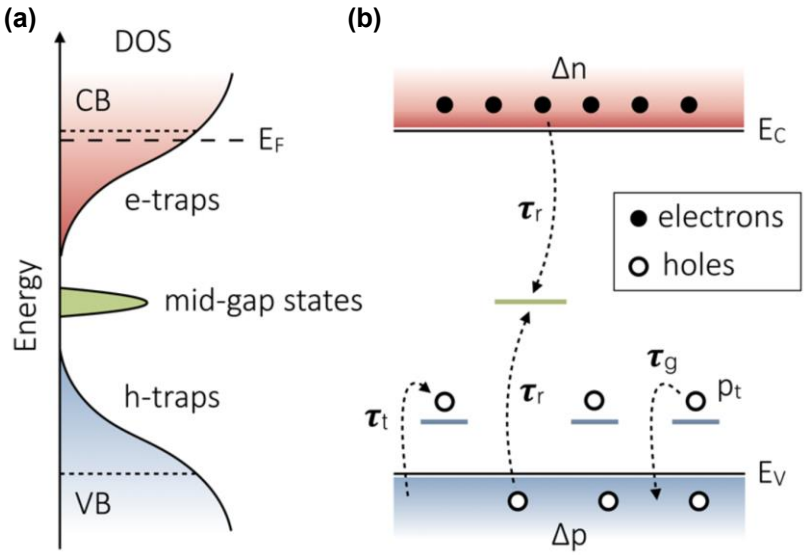

Figure 4.4 Photoconductive Effect by Hornbeck–Haynes model (a) Energy-resolved DOS in atomically thin MoS_2. CB (VB) is the conduction (valence) band. E_F, Fermi level is closed to CB if $MoSe_2$ exhibits *n*-type behavior. Band tail states are placed underneath (above) the conduction (valence) band edge that traps electron (hole) charge. The VB-DOS is assumed to be mirror-symmetric to the CB-DOS. It is assumed that the recombination happens through mid-gap states with an empirical (constant) rate $1/\tau_r$. (b) Simplified energy band diagram representing the model of the charge trapping in PC effect. The VB tail is approximated by a discrete distribution of hole traps with density P_t (occupied by p_t). $1/\tau_t$, and $1/\tau_g$ are the hole trapping and escaping rates, respectively. Figure reprinted with permission from reference 196, © 2014, American Chemical Society.

4.3.1 Photoconductive Effect

To calculate the conductivity increase due to illumination, a modified Hornbeck–Haynes model [198]–[200] (see Figure 4.4) is used as

$$\Delta\sigma = q\left(\mu_n + \mu_p\right)\Delta p + q\mu_n p_t \tag{4.2}$$

where q, μ_n, μ_p, Δp and p_t are the electron unit charge, electron and hole mobility, excess hole density in the valence band and the density of captured holes in the band tail states, respectively [196]. The conductivity of the material with the trap states is higher than that without trap states by amount of $q\mu_n p_t$. Carrier dynamics are described by the differential equations:

$$\frac{d\Delta p}{dt} = g - \frac{\Delta p}{\tau_r} + \frac{p_t}{\tau_g} - \frac{\Delta p}{\tau_t}\left(1 - \frac{p_t}{P_t}\right) \tag{4.3}$$

$$\frac{dp_t}{dt} = -\frac{p_t}{\tau_g} + \frac{\Delta p}{\tau_t}\left(1 - \frac{p_t}{P_t}\right) \tag{4.4}$$

where g (= $\eta P_{abs} / h\nu$) is the generation rate of electron-hole pairs and τ_r is carrier recombination lifetime. η and $h\nu$ are internal quantum efficiency and single photon energy, respectively. P_{abs} is the absorbed power density, given by $P_{inc}\left[1 - \left(e^{-\alpha^{\perp}d} + e^{-\alpha^{\parallel}d}\right)/2\right]$, where P_{inc}, $\alpha^{\perp}$, $\alpha^{\parallel}$, and d are power density of the incident optical illumination, absorption coefficient in the vertical/lateral direction, and thickness of channel material, respectively. P_t is the total trap density, and τ_t and τ_g and are the trapping and escaping time of holes into and from the trap states, respectively [196]. These equations can be solved by $d\Delta p/dt = dp_t/dt = 0$ for an equilibrium state, resulting in

$$\Delta p = g\tau_r \tag{4.5}$$

$$p_t = \frac{gP_t\tau_r}{g\tau_r + P_t\left(\frac{\tau_t}{\tau_g}\right)} \tag{4.6}$$

4.3.2 Photogating Effect

The PG effect is modeled with the threshold voltage shift (ΔV_{th}) due to the accumulated or trapped holes and potential barrier lowering ($\Delta\phi_b$), considering that ΔV_{th} is proportional to $\Delta\phi_b$ ($I_{ph,PG} = g_m \Delta V_{th}$) [197]. The barrier lowering can be modeled as

$$\Delta\phi_b = n\frac{k_B T}{q}\ln\left(\frac{qp}{\tau_{eff} J_{pd}}\right) \tag{4.7}$$

where k_B, T, J_{pd}, τ_{eff}, and n are the Boltzmann constant, temperature, dark hole current, effective lifetime, and a constant accounting for the saturation effect, respectively [201]. Equation (4.7) is derived from calculating the number of holes, p

$$\frac{p}{\tau_{eff}} = \frac{J_{pd}}{q} + \frac{P_{inc}\eta}{h\nu} + \frac{p_t}{\tau_g} \tag{4.8}$$

where $\frac{J_{pd}}{q}$, $\frac{P_{inc}\eta}{h\nu}$ and $\frac{p_t}{\tau_g}$ correspond to background carriers (in a dark condition), excess carriers in the valence band due to the illumination, and trapped holes in sub-gap states, respectively. For n-type transistors considered in this study, we assumed J_{pd} is less than the dark electron current density (J_{nd}) by three orders of magnitude. Considering hole accumulation, barrier lowering, and threshold voltage shift all together, the photogating current can be determined by

$$I_{ph,PG} = g_m \Delta V_{th} = \chi_{BL} g_m \frac{k_B T}{q} ln\left(1 + \frac{P_{inc}\eta q}{h\nu J_{pd}} + \frac{p_t q}{\tau_g J_{pd}}\right) \tag{4.9}$$

where χ_{BL} is barrier-lowering efficiency, the only fitting parameter for the PG effect, which is directly related to the trap density and also to the wavelength of the incident light.

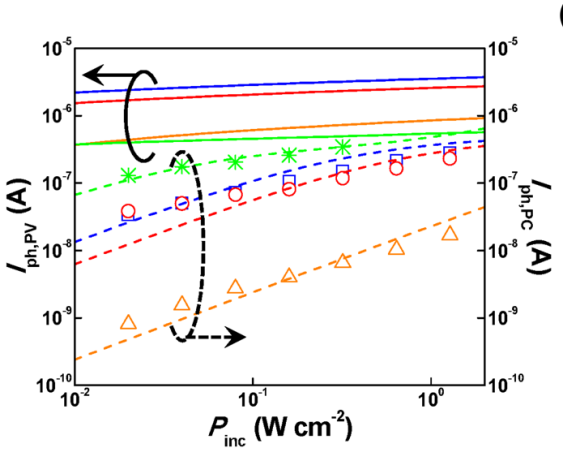

Figure 4.5 Separated $I_{ph,PG}$ (solid lines) and $I_{ph,PC}$ (dashed lines) from I_{ph} used to plot Figure 4.2(b) (the same colors are used as in Figure 4.2(b) for various wavelengths). The symbols are taken from the measurements in the OFF-states (V_{GS} = –40 V) at Figure 4.2(a) for $I_{ph,PC}$.

	P_t	τ_r	τ_t / τ_g
$MoSe_2$	5×10^{10} /cm^2	150 ps	1/1,000
MoS_2	3×10^{10} /cm^2	8 ns	1/100

Table 4.1 Fitting parameters for photoconductive current

	$MoSe_2$			MoS_2
	405 nm	638 nm	852 nm	405 nm
$\alpha^{\perp}$	28.3×10^4 /cm	1.22×10^4 /cm	4.88×10^3 /cm	26.6×10^4 /cm
$\alpha^{\parallel}$	103.4×10^4 /cm	10.3×10^4 /cm	1.37×10^4 /cm	87.1×10^4 /cm

Table 4.2 Absorption coefficient for $MoSe_2$ and MoS_2 [202].

4.3.3 Results

Based on the models developed above, we analyzed the measurement data to validate the model. First we have calculated $I_{ph,PC}$ with Equation (4.1) and plotted it in Figure 4.5 (dashed lines) by fitting τ_r, τ_t/τ_g, and P_t with experimental data (symbols; obtained from Figure 4.2 (a) in the OFF-state, $V_{GS} = -40$ V), resulting in fitting parameters shown in Table 4.1. τ_g of 10 ns and 1 ns are assumed for $MoSe_2$ and MoS_2, respectively, which will be used later to evaluate PG effect.

W/*L* is 8.3 μm / 13.1 μm for $MoSe_2$; 63 μm / 15.1 μm for MoS_2. The mobilities of 97.4 $cm^2/V \cdot s$ and 16.6 $cm^2/V \cdot s$ are extracted from the experiments and used for $MoSe_2$ and MoS_2 TFTs, respectively. The internal quantum efficiency is chosen as η = 0.5, 0.5, and 0.07 for λ_{ex} = 405, 638, and 852 nm, respectively, by fitting the measurements. Absorption coefficients (α) corresponding to the materials and the wavelength are written in Table 4.2 and thickness of channel materials is d = 60 nm for $MoSe_2$ and 40 nm for MoS_2.

Then, the measured photoresponsivity is fitted with the models in Figure 4.2(b) (dashed lines), where both $I_{ph,PC}$ and $I_{ph,PG}$ are considered ($I_{ph} = I_{ph,PC} + I_{ph,PG}$), by introducing a parameter χ_{BL} describing barrier-lowering efficiency. We have used χ_{BL} = 25, 19.5, 9 for λ_{ex} = 405, 638, 852 nm, respectively, and $g_m = 4.55 \times 10^{-7}$ S for $MoSe_2$; χ_{BL} = 2.5 at λ_{ex} = 405 nm and $g_m = 6.64 \times 10^{-7}$ S for MoS_2. The fitted values of χ_{BL} suggest that the trap density in $MoSe_2$ is significantly larger than that of MoS_2, which is consistent with P_t values determined for the PC effect above. Lastly, we obtained $I_{ph,PG}$ by subtracting $I_{ph,PC}$ from I_{ph} and plotted it in Figure 4.5 (solid lines) to compare it against $I_{ph,PC}$. Interestingly, our result indicates that, although the PC current is larger in MoS_2, the synthetic $MoSe_2$ shows a significantly larger PG effect, resulting in remarkably higher photoresponsivity in the $MoSe_2$ TFTs. Notably, $I_{ph,PG}$ is larger than $I_{ph,PC}$ by 92 times in $MoSe_2$ at P_{inc} = 20 mW/cm and λ_{ex} = 405 nm, whereas $I_{ph,PG}/I_{ph,PC}$ of MoS_2 remains much lower for the entire range of P_{inc} considered. The fitted parameters (τ_r, τ_t/τ_g, P_t, χ_{BL}) indicate that a greater number of states exists energetically deeper in the band gap region for the synthetic $MoSe_2$, resulting in shorter recombination lifetime (hence smaller $I_{ph,PC}$) and longer escaping lifetime for holes from the trap states (hence larger $I_{ph,PG}$), compared to those in natural multilayer MoS_2 phototransistors.

4.4 Conclusion

In conclusion, two key photoillumination effects were analytically modeled to understand underlying physics behind optical device characteristics of the multilayer $MoSe_2$ phototransistors. The device was fabricated by CVD under Mo-rich condition, resulting in very large photoresponsivity which is mainly due to photoconductive (PC) and photogating (PG) effects. PC effect is current increase by conductivity increase due to generated excess electron–hole pairs, which was modeled based on modified Hornbeck–Haynes model. PG effect is amplification of current due to suppression of energy barriers by trapped or accumulated holes. Both models successfully fitted on the experimentally measured photoresponsivity of the fabricated multilayer $MoSe_2$ phototransistor as function of light power intensity, and compared each other, demonstrating that PG effect is much larger than PC effect, and takes the most of part of the photogain while the difference is relatively smaller for MoS_2 case. Some parameters were fitted indicating that the large photoresponsivity of $MoSe_2$ phototransistors is due to long escaping time of holes from the trap states. The modeling analysis provided better understanding of photoillumination effects and connection between trap states induced by Mo interstitials and large optical response, which could be utilized for the further investigation by device simulation in the next chapter.

Chapter 5 Simulation for Optical Properties of $MoSe_2$ Phototransistors

5.1 Introduction

Previously, optical characteristics of $MoSe_2$ phototransistors were mathematically modeled. However, the approach has the adapted modelling schemes [196] suitable for bulk semiconductor devices, while developing a model for photoexcitation in these sub-nanometer thin devices requires the use of highly accurate quantum transport simulations. Other works have simulated monolayer MoS_2 photodetectors using a drift-diffusion transport, which disregards any quantum effects. This has been done by calculating hole accumulation though potential confinement in the valence band [203], or by solving for the electromagnetic response and carrier transport in the spatial and frequency/time domains [204].

In this chapter, we present a comprehensive numerical simulation of monolayer $MoSe_2$ phototransistors based on the quantum transport, especially, NEGF. The PC effect is included using a modified Hornbeck–Haynes [196], [205] leading to conductivity enhancement. The PG effect is implemented through a trap model which describes the capture and emission of holes with respect to trap states close to valence band, and we explain its inclusion into the NEGF simulator. When these effects are studied separately, it is found that the photogating effect is the dominant method for photoexcitation in this material. We investigate this by analyzing energy band diagrams after modulating the electrostatics though control of the gate voltage, and observing the resulting variation in the concentration of captured holes in the trap sites. Finally, we report the dependence of key photosensing figures of merit on material properties such as total trap concentration, capture cross-section, and recombination carrier lifetime.

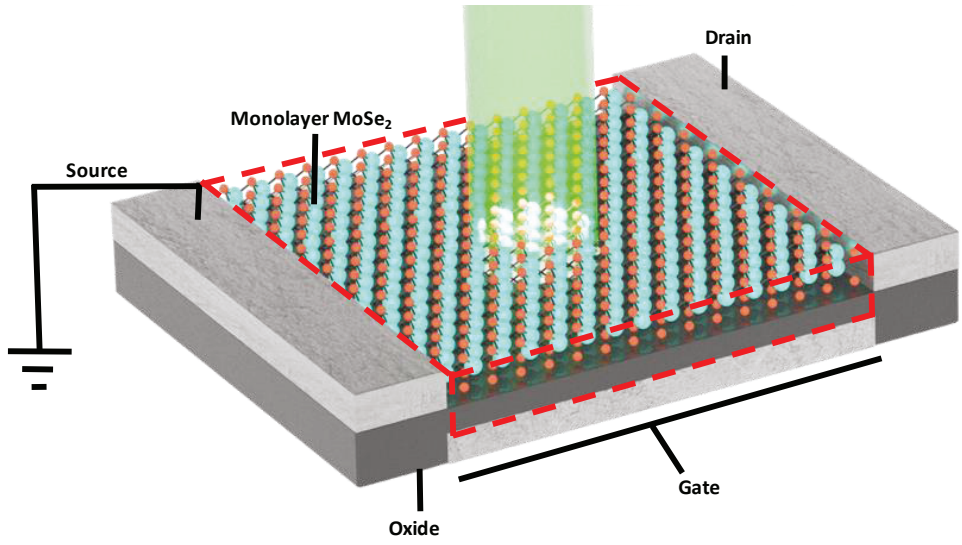

Figure 5.1 A schematic of the device geometry for a simulated $MoSe_2$ phototransistor. A region enclosed by red dashed lines is effective region simulated in this study.

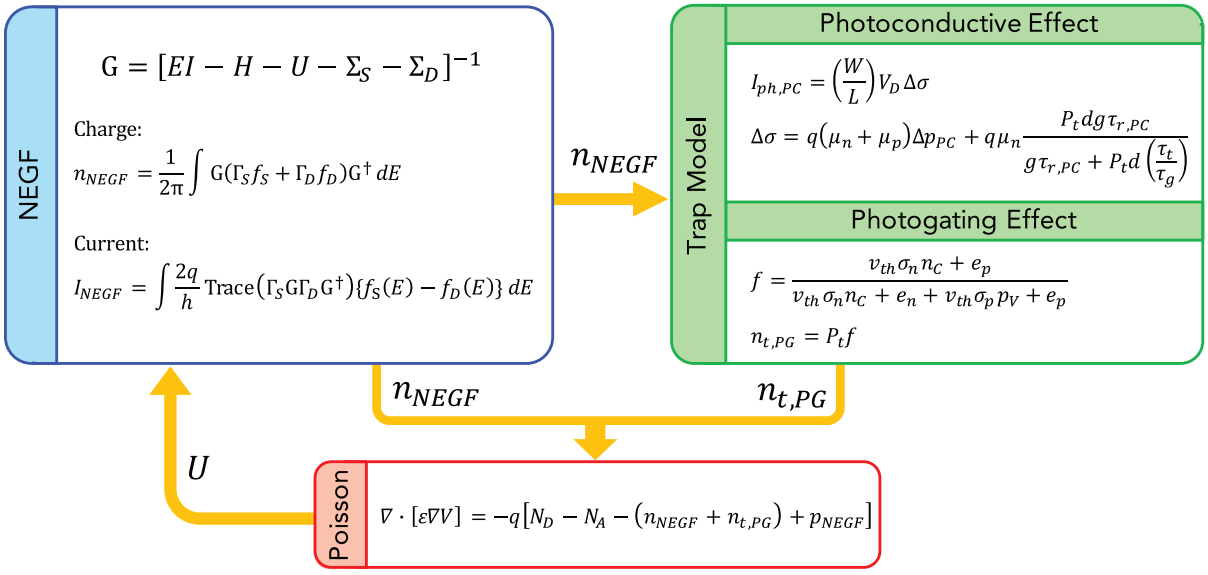

Figure 5.2 Self-consistent simulation scheme. NEGF, trap model and Poisson modules are calculated iteratively until converged.

5.2 Simulation Methodology

5.2.1 Device Simulation

Figure 5.1 exhibits a device schematic of a simulated phototransistor where the channel is monolayer $MoSe_2$ with a band gap of $E_g = 1.43$ eV. The nominal device has a single back gate with 50-nm channel length (L_{ch}) and 2.59 nm-thick SiO_2 gate oxide (dielectric constant of $\kappa_{SiO_2} = 3.9$). Source and drain are Schottky contacts with Schottky barrier height of $\Phi_{Bn} = 0.1$ eV, which is non-zero value considering significant metal-induced gap states at Schottky contact between metal and 2D materials, and not too large value due to almost linear behavior of output characteristics at low drain voltage as shown in Figure 4.1(c). Source is grounded and drain voltage is $V_D = V_{DD}$ with the power supply voltage of $V_{DD} = 0.5$ V.

The overall self-consistent simulation scheme is shown in Figure 5.2, in which three modules are connected: namely, the NEGF for carrier transport [166] (see Figure 5.2 for equations), the Poisson's equation for electrostatics, and the trap model module. Electronic properties of monolayer $MoSe_2$ are described by the Hamiltonian matrix within an effective mass approximation ($m^* = 0.5m_0$, m_0 being single electron mass). The electron concentration (n_{NEGF}) is produced in the NEGF module, but the hole concentration (p_{NEGF}) is assumed to be zero as it is negligible for an *n*-type transistor. Ballistic transport is assumed due to the relatively short channel length considered in this paper. The concentration of trapped electrons in the band gap ($n_{t,PG}$) is calculated in the trap model using the electron concentration from the NEGF. Then, both n_{NEGF} and $n_{\mathrm{t,PG}}$ are provided to the Poisson's equation to update the electrostatic potential as

$$\nabla \cdot (\varepsilon \nabla V) = -q\left[N_D - N_A - \left(n_{NEGF} + n_{t,PG}\right) + p_{NEGF}\right] \tag{5.1}$$

where ε, U, N_D, and N_A are permittivity, potential energy, doping concentrations of donors and acceptors, respectively (both N_D and N_A are zero in this study). Even under the dark condition, the total concentration of electrons should be evaluated by considering both n_{NEGF} and $n_{t,PG}$ as gap states near the valence band will be still filled by electrons. Since trapped hole concentration ($p_{t,PG}$) can be viewed as the concentration of unoccupied trap states, so it can be calculated as $p_{t,PG} = P_t - n_{t,PG}$ (P_t being total trap concentration). Therefore, the change in trapped hole concentration becomes $\Delta p_{t,PG} = -\Delta n_{t,PG}$; under the light illumination, if the trapped hole concentration increases, it is equivalent to the loss of electrons in the trap states.

5.2.2 Trap Models

As briefly explained in the introduction, in general, there are two main mechanisms that contribute to the photocurrent: PC and PG effects. Photocurrent (I_{ph}) is the increase in the total source-drain current (I_{DS}) under illumination with respect to the dark current (I_{dark}); $I_{DS} = I_{dark} + I_{ph}$. In this study, the PG effect is incorporated directly in the self-consistent NEGF-Poisson iterations (through $n_{t,PG}$) while the PC effect should be taken into account separately:

$$I_{DS} = I_{NEGF} + I_{ph,PC} \tag{5.2}$$

where $I_{\mathrm{ph,PC}}$ is photoconductive current.

5.2.2.1 Photoconductive Effect.

Photoconductive current is attributed to conductivity increase ($\Delta\sigma$) by photo-induced excess carriers, which can be calculated by

$$I_{ph,PC} = \left(\frac{1}{L_{ch}}\right) V_D \Delta\sigma, \tag{5.3}$$

and $\Delta\sigma$ is given by

$$\Delta\sigma = q\mu_n \Delta n_{PC} + q\mu_p \Delta p_{PC} \tag{5.4}$$

where μ_n, μ_p, Δn_{PC}, and Δp_{PC} are electron and hole mobility, photo-induced excess electron and hole density in the conduction and valence band, respectively. Δp_{PC} is expressed as

$$\Delta p_{PC} = g\tau_{r,PC} \tag{5.5}$$

at the steady state, where g $(= \eta P_{abs}/h\nu)$ is generation rate and $\tau_{r,PC}$ is carrier recombination lifetime. η and $h\nu$ are internal quantum efficiency and single photon energy, respectively. P_{abs} is the absorbed power density, given by $P_{inc}\left[1 - \left(e^{-\alpha^{\perp}d} + e^{-\alpha^{\parallel}d}\right)/2\right]$, where P_{inc} is incident optical power density, d is the thickness of monolayer $MoSe_2$, $a^{\perp}$ and $a^{\parallel}$ are the absorption coefficient in the vertical and lateral direction, respectively. In the presence of gap states near the valence band, charge neutrality under illumination gives rise to[196]

$$\Delta n_{PC} = \Delta p_{PC} + p_{t,PC} \tag{5.6}$$

where $p_{t,PC}$ is the trapped hole density. A modified Hornbeck–Haynes model [196], [205] is used to model $p_{t,PC}$, which approximates valence band tail by a narrow distribution of states with P_t at the trap energy E_t.[196], [205] Location of the Fermi level E_F is assumed to be far above E_t. Thus, we can obtain the trapped hole density as [196], [205]

$$p_{t,PC} = \frac{P_t d g \tau_{r,PC}}{g\tau_{r,PC} + P_t d \frac{\tau_t}{\tau_g}} \tag{5.7}$$

where τ_t and τ_g are the trapping and escaping time of holes into and from the trap states, respectively, and τ_t/τ_g ratio can be evaluated by $1/[(P_t/N_V)\exp((E_t - E_V)/kT)]$, where N_V is the effective density-of-states at the valence band edge (E_V). Finally, $I_{ph,PC}$ can be obtained by using Equation (5.3)–(5.7) along with the parameters provided in Table 5.1.

λ [nm]	η[205]	$\alpha^{\perp}$[205] [/cm]	$\alpha^{\parallel}$[205] [/cm]	$\tau_{r,PC}$[196] [ps]	$\tau_{r,PG}$[203] [μs]	μ_n, μ_p[205] [$cm^2/V \cdot s$]	P_t [$/m^3$]	$E_t - E_V$ [eV]	σ_n/σ_p [$/m^2$]
405	0.5	28.3×10^4	103.4×10^4						
638	0.5	1.22×10^4	10.3×10^4	100	1	97.4	5×10^{25}	0.3	10^{-3}
852	0.07	4.88×10^3	1.37×10^3						

Table 5.1 Material parameters used for the $MoSe_2$ phototransistor

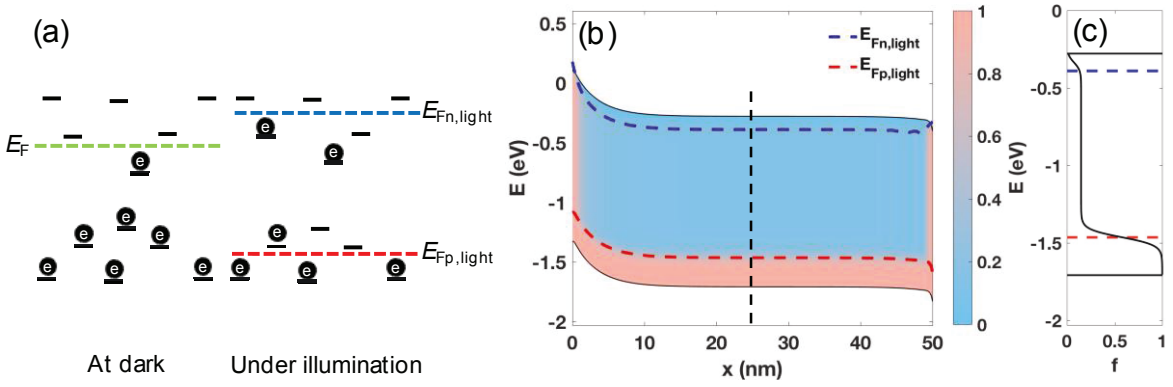

Figure 5.3 (a) Simplified energy band diagrams that illustrate occupation of electrons in the trap states at dark (left) and under illumination (right). E_F is the Fermi level under equilibrium. $F_{n,light}$ and $F_{p,light}$ are quasi-Fermi levels for electrons and holes under illumination, created due to excess carriers. (b) Contour plot of occupational function for electrons (f) at V_G = 0.5 V in the band gap region. (c)

Occupational function in the middle of the channel [at x = 25 nm, along the vertical black dashed line in (b)].

5.2.2.2 Photogating Effect

The PG effect is the potential barrier modulation due to localized or trapped charge carriers at the channel–oxide interface [203], [206], [207] or material defects in a device [205]. In the I_{DS}–V_G characteristics, the PG effect can be observed with a threshold voltage shift (ΔV_{th}) under illumination. The current increase at a given voltage is frequently approximated as $I_{ph,PG} \approx g_m \Delta V_{th}$, where g_m ($= dI_{DS}/dV_G$) is transconductance. On the contrary, in this paper, $I_{ph,PG}$ is directly evaluated by means of the quantum transport simulation, considering the trapped holes as $p_{t,PG} = P_t(1-f)$, where f is the probability of electron occupation at a given trap state.

Figure 5.3(a) illustrates the occupation of carriers in the trap states. At the dark state, most of the trap states below the E_F are filled with electrons, while those above the E_{F} are remained mostly empty (*i.e.* filled with holes). Under the illumination, the Fermi level splits into two due to the excess electrons and holes generated: quasi-Fermi level for electrons ($F_{\mathrm{n,light}}$) and holes ($F_{\mathrm{p,light}}$) (the right panel of Figure 5.3(a)). Consequently, most of trap states are empty above $E_{F_n,light}$ and filled below $E_{F_p,light}$. However, the occupation of carriers between the two quasi-Fermi levels can be affected by various factors such as carrier concentration, energy of trap states, capture cross sections, and total trap concertation. The statistics for the arbitrary distribution of traps under steady-state conditions under illumination can be derived by Shockley-Read expression [208].

To calculate concentration of electrons and holes in the trap states, electron capture (r_a), electron emission (r_b), hole capture (r_c), and hole emissions rates (r_d) are defined as [208]:

$$r_a = v_{th}\sigma_n n_C P_t(1-f) \tag{5.8}$$

$$r_b = e_n P_t f \tag{5.9}$$

$$r_c = v_{th}\sigma_p p_V P_t f \tag{5.10}$$

$$r_d = e_p P_t(1-f) \tag{5.11}$$

where v_{th}, n_C, p_V are thermal velocity, free electron concentration in the conduction band, and free hole concertation in the valence band, respectively. σ_n and σ_p are electron and hole capture cross sections, which are assumed to be independent of energy. e_n and e_p are emission rate of electrons and holes from the trap states. Under the thermal equilibrium condition, $r_a = r_b$ and $r_c = r_d$, resulting in $e_n = v_{th}\sigma_n n_0 exp\{(E_t - E_{F0})/kT\}$ and $e_p = v_{th}\sigma_p p_0 exp\{(E_{F0} - E_t)/kT\}$. n_0 and p_0 are free electron and hole concentrations under the thermal equilibrium, which can be obtained by Fermi-Dirac integral for the order of 0 since the carriers are distributed in 2D material. Those are calculated as $n_0 =$

$N_c\, ln[1 + exp\{(E_{F0} - E_C)/kT\}]$ and $p_0 = N_V\, ln[1 + exp\{(E_V - E_{F0})/kT\}]$ where N_C is the effective density-of-states at the conduction band minima (E_C). E_{F0} is thermal equilibrium Fermi level assumed to be at the mid-gap in the monolayer $MoSe_2$. Using the Eqs. (5.8)–(5.11), f is obtained as [208]:

$$f = \frac{v_{th}\sigma_n n_C + e_p}{v_{th}\sigma_n n_C + e_n + v_{th}\sigma_p p_V + e_p} \tag{5.12}$$

which describes the probability of capturing electrons at if a trap state exists at a certain energy. Free electron concentration is calculated by $n_C = n_{NEGF} + \Delta n_{ph}$, where n_{NEGF} is the electron concentration obtained from the NEGF module and $\Delta n_{ph} = g\tau_{r,PG}/d$ is the generated electron concentration. Different values of recombination lifetime are employed for PC and PG effects since lifetime is a strong function of V_G and one could be more dominant over the other at ON or OFF state.[209], [210] As aforementioned, the hole concentration is negligible at dark. Under illumination, p_V becomes $p_V \cong \Delta p_{PG} = \Delta n_{PG}$. Finally, the concentrations of captured electrons and holes are calculated by $n_{t,PG} = P_t f$ and $p_{t,PG} = P_t(1 - f)$. It should be noted that $n_{t,PG}$ and $p_{t,PG}$ are dependent of channel position x since n_{NEGF} is a strong function of x under non-equilibrium conditions (see Figure 5.3(b)).

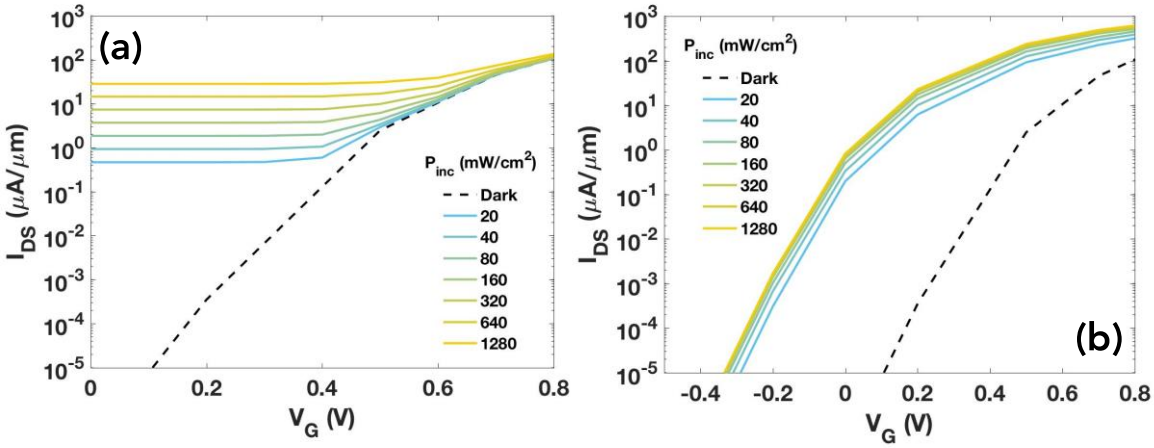

Figure 5.4 Transfer characteristics (I_{DS}–V_G) at dark (black dashed line) and under illumination (colored solid lines) with various incident optical power densities P_{inc} at a wavelength of $\lambda = 405$ nm considering (a) only the photoconductive effect and (b) only the photogating effect.

5.3 Results

Figure 5.4(a) and (b) show the simulated I_{DS}–V_G characteristics under illumination by considering the PC and the PG independently ($P_{inc} = 20$–$1{,}280$ mW/cm^2 and wavelength of $\lambda = 405$ nm). While the PC effect can be clearly seen at low gate voltages, the PG effect exhibits significant impacts on the total current at high gate voltages. Consequently, photogating current $I_{ph,PG}$ becomes significantly larger than $I_{ph,PC}$ by over 400 times at $V_G = 0.8$ V with P_{inc} = 20 mW/cm^2. In practice, $I_{ph,PC}$ and $I_{ph,PG}$ cannot be distinguished, and only the total I_{DS} can be measured regardless of the conditions of illumination and bias. Figure 5.5(a), (b), and (c) exhibit transfer characteristics of monolayer $MoSe_2$ phototransistors with $P_{inc} = 20$–$1{,}280$ mW/cm^2 for three different wavelengths $\lambda = 405, 638,$ and 852 nm, respectively. The trend is exactly same as that in the experiment [205]. In general, photocurrent increases with larger P_{inc} and shorter λ. This is because more excess carriers can be generated (larger generation rate). Similarly, shorter wavelength can result in a larger number of generated excess carriers due to the higher quantum efficiency and absorption coefficients, as listed in Table 5.1. The precise quantities could be extracted from optical light simulation [211], [212], which is beyond the scope of this study. It should be noted that significantly larger photocurrent can be achieved at high gate voltages compared to low gate voltages: $I_{ph} = 210.5$ μA/μm at $V_G = 0.8$ V; $I_{ph} = 0.47$ μA/μm at $V_G = -0.2$ V. As discussed earlier, the dominant photoillumination mechanism at a high V_G is the PG effect, the extent of which can be seen directly by plotting the threshold voltage shift (ΔV_{th}). Figure 5.5(d) shows the variation of ΔV_{th} with the power density for the devices shown in Figure 5.5(a)–(c). At $P_{\mathrm{inc}} = 20$ mW/cm^2, ΔV_{th} is –0.4 V and –0.24 V for λ = 405 nm and 638 nm, respectively. As P_{inc} increase, ΔV_{th} also gradually saturates to ΔV_{th} = –0.45 V, at which the trap states are completely filled with holes due to the large power intensity with short wavelengths (more detail will be discussed in Figure 5.6 below). For λ = 852 nm, the threshold voltage shift is significantly smaller compared with the other two cases, and it reaches only –0.3 V at $P_{inc} = 1{,}280$ mW/cm^2, indicating that there still exist rooms for the PG effect with unfilled trap states for holes to occupy.

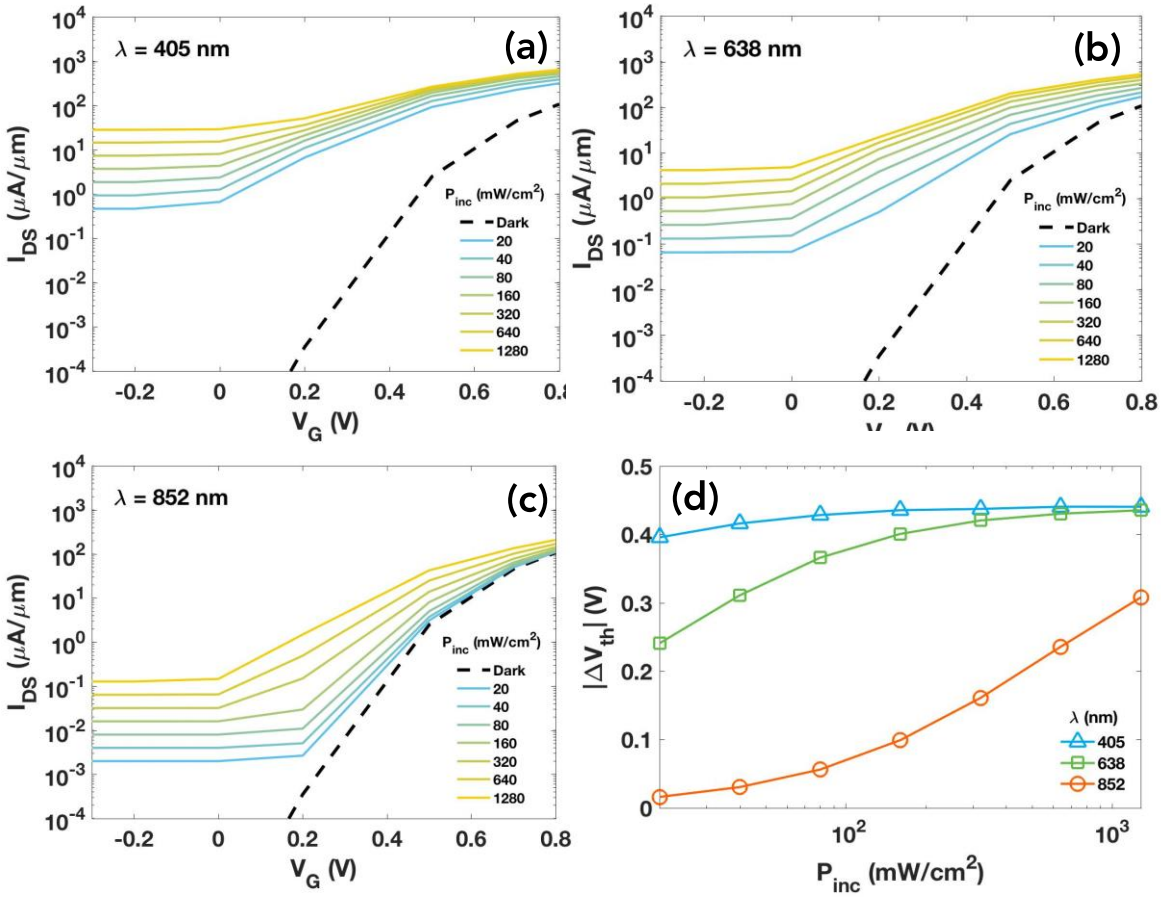

Figure 5.5 Transfer characteristics (I_{DS}–V_G) at dark (black dashed line) and under illumination (colored solid lines) with various P_{inc} at the wavelength of (a) 405 nm, (b) 638 nm and (c) 852 nm. (d) Threshold voltage shift ΔV_{th} as a function of P_{inc} for the wavelength shown in (a), (b), and (c).

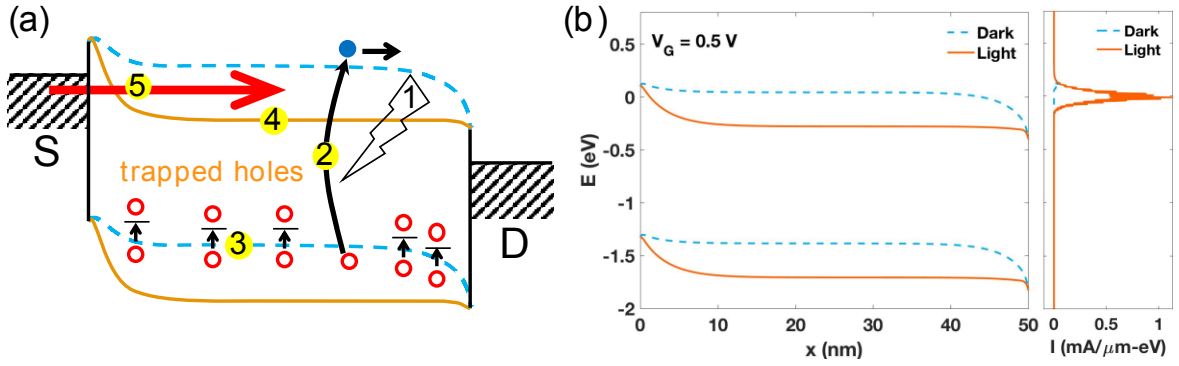

Figure 5.6 (a) A schematic illustration of the mechanism of the photogating effect. (b) (Left) Simulated energy band diagram at $V_G = 0.5$ V at dark (dashed line) and under illumination (solid line) at $P_{inc} = 20$ mW/cm^2 and $\lambda = 405$ nm. (Right) Energy-resolved current spectrum at dark (dashed) and under illumination (solid).

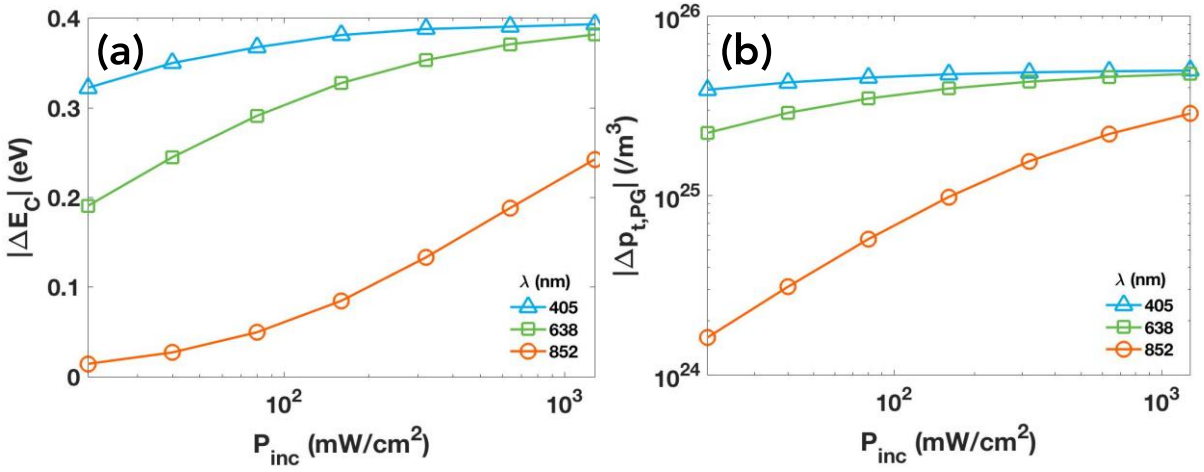

Figure 5.7 Change of (a) conduction band edge ($|\Delta E_C|$) and (b) captured hole concentration ($|\Delta p_{t,PG}|$) between the dark and the illumination states at the mid-channel at $V_G = 0.5$ V, as a function of P_{inc}, for $\lambda = 405, 638,$ and 952 nm.

Next, we will investigate underlying physics of the PG effect to develop in-depth understanding of the relation among trapped carriers, threshold voltage shift and current increase. Figure 5.6(a) illustrates the PG processes in a schematic diagram: 1) Under the illumination, photons are absorbed by the channel material. 2) Electron-hole pairs are generated, resulting in excess carriers in the conduction and the valence band. 3) Due to the trap states existing near the valence band, the excess holes are captured into trap states, 4) lowering the potential barrier in the channel region. 5) Consequently, the Schottky barrier at the source-channel junction is significantly reduced, which triggers significant electrons injection and the current increase at a given gate voltage. If we consider the full I_{DS}–V_G characteristics at dark and under illumination, the current increase can be viewed as threshold voltage shift. In Figure 5.6(b), we confirmed the PG process explained in Figure 5.6(a) using the numerical simulation. We have plotted the actual simulated energy diagram in Figure 5.6(b) at dark (dashed lines) and under illumination (solid lines) at $V_G = 0.8$ V with $P_{inc} = 20\ \mathrm{mW/cm^2}$ and $\lambda = 405$ nm, which clearly shows the barrier lowering and the consequently reduced Schottky barrier at the source-channel junction. The change of current as function of energy is also shown in the right panel of Figure 5.6(b). Therefore, the PG effect can be characterized in various ways through the variation of potential barrier (ΔE_C) or the change in captured hole concentration ($\Delta p_{t,PG}$) as well as ΔV_{th}. Figure 5.7(a) presents ΔE_C as a function of P_{inc} for λ = 405 nm, 638 nm and 852 nm. The potential barrier lowering is due to the increase of trapped holes. The difference in the concentration of the trapped holes between at dark and under illumination ($\Delta p_{t,PG} = p_{t,PG,light} - p_{t,PG,dark}$) is plotted in Figure 5.7(b) for the same P_{inc} and λ. With increasing the power density, $\Delta p_{t,PG}$ for $\lambda = 405$ nm and 638 nm are saturated to $5 \times 10^{25}/\mathrm{m^3}$, the same as total trap concentration of P_t, which indicates that trap states are completely filled by holes under illumination whereas mostly filled by electrons at dark. On the contrary, for $\lambda = 852$ nm, the trap states are only partially filled by holes at $P_{inc} = 1{,}280$ mW/cm^2. In practice, the efficiency of the PG effect (*i.e.*, ΔE_C, $\Delta p_{t,PG}$) can be affected by various factors such as gate oxide thickness and channel length as well as P_t, λ and P_{inc}.

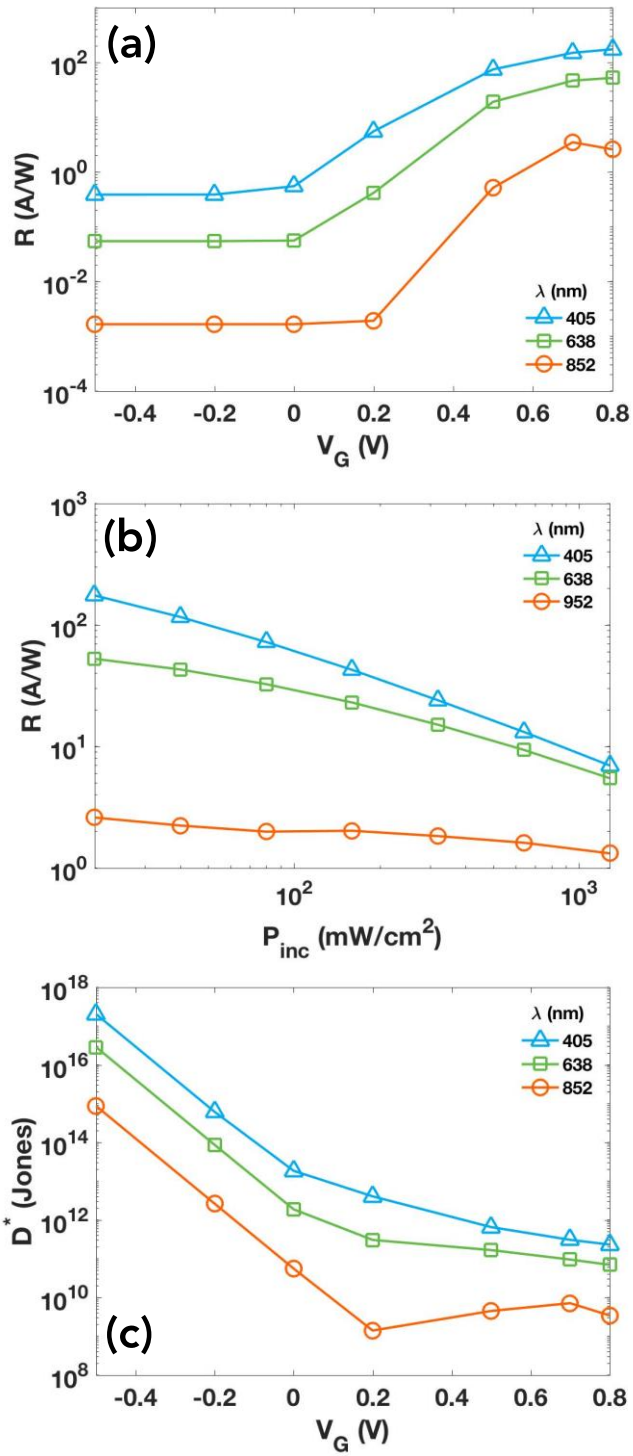

Figure 5.8 (a) Photoresponsivity (R) as function of V_G at P_{inc} = 20 mW/cm^2. (b) Dependence of R on various P_{inc} at V_G = 0.8 V. (c) Detectivity (D^*) with varying V_G at P_{inc} = 20 mW/cm^2. Wavelengths of λ = 405, 638, and 852 nm are used.

So far, we have investigated the mechanism of photoillumination effects. Next, we will examine the figure-of-merit of $MoSe_2$ photodetectors. Photoresponsivity is defined as $R = I_{ph}/P_{inc}$, which reflects the gain (I_{ph}) of the photodetectors with respect to the input (P_{inc}). Although we assume ballistic transport in this study to explore the underlying physics of photoillumination effects, here we introduce an empirical factor of 2.2×10^{-3} for current degradation. It is obtained by $\lambda_{mfp}/(\lambda_{mfp} + L_{ch,ex})$ where λ_{mfp} is mean free path of $MoSe_2$, assumed to be 28.6 nm, and $L_{ch,ex}$ is channel length of fabricated device in [205], considering possible scattering and fabrication-related non-idealities in actual devices (*e.g.*, impurities, interstitial atoms, and large dimension of the fabricated device), so that the value of R can be similar to that in the experiments [205]. Figure 5.8(a) presents R with different gate voltages for λ = 405 nm, 638 nm and 852 nm at $P_{inc} = 20\ \mathrm{mW/cm^2}$. In general, photoresponsivity is larger with shorter wavelength at a given gate bias, and can be increased by applying larger gate voltage. If the $MoSe_2$ phototransistor is operated at the ON state, R can be larger by two orders of magnitude as compared with the value at the OFF state for the same wave length. In other words, I_{ph} can be significant at the ON state, as it can be seen in Figure 5.5, due to the PG effect. Next, the same is plotted with varying power intensity in Figure 5.8(b) at the highest gate voltage, V_G = 0.8 V. In general, R is maximized at the lowest P_{inc} and decreased with increasing power intensity. This indicates that photogain by the PG effect is inefficient at high P_{inc} since most trap states are already filled, as it can be seen in Figure 5.7(b). On the other hand, at low P_{inc}, there is room for additional PG effect when $\Delta p_{t,PG} \ll P_t$ (also see Figure 5.7(b)). These results are consistent with previous reports [174], [196], [205], [210], [213], [214].

While photoresponsivity can tell the gain of phototransistors, it doesn't necessarily mean the sensitivity of photodetectors, for which I_{dark} should be considered along with R so that signal-to-noise ratio can be maximized. In this regard, specific detectivity (D^*) can be informative figure-of-merit, which is defined as $D^* = R\sqrt{L_{ch}}/\sqrt{2qI_{dark}}$, where q is single electron charge. Figure 5.8© shows the variation of D^* with V_G and λ. In general, $D^*$is larger with shorter wavelength as in R; however, it shows opposite trend with V_G as compared to that of R. At low gate voltages, D^* becomes large due to the small I_{dark}. Even though large D^* is generally preferable, it should be considered with actual signal (R or I_{ph}) and noise (I_{dark}) levels; if the signal and noise levels are too low, the detection could be hampered by the limitation of the device. Hence, the V_G should be carefully chosen for the proper operation window of photodetectors.

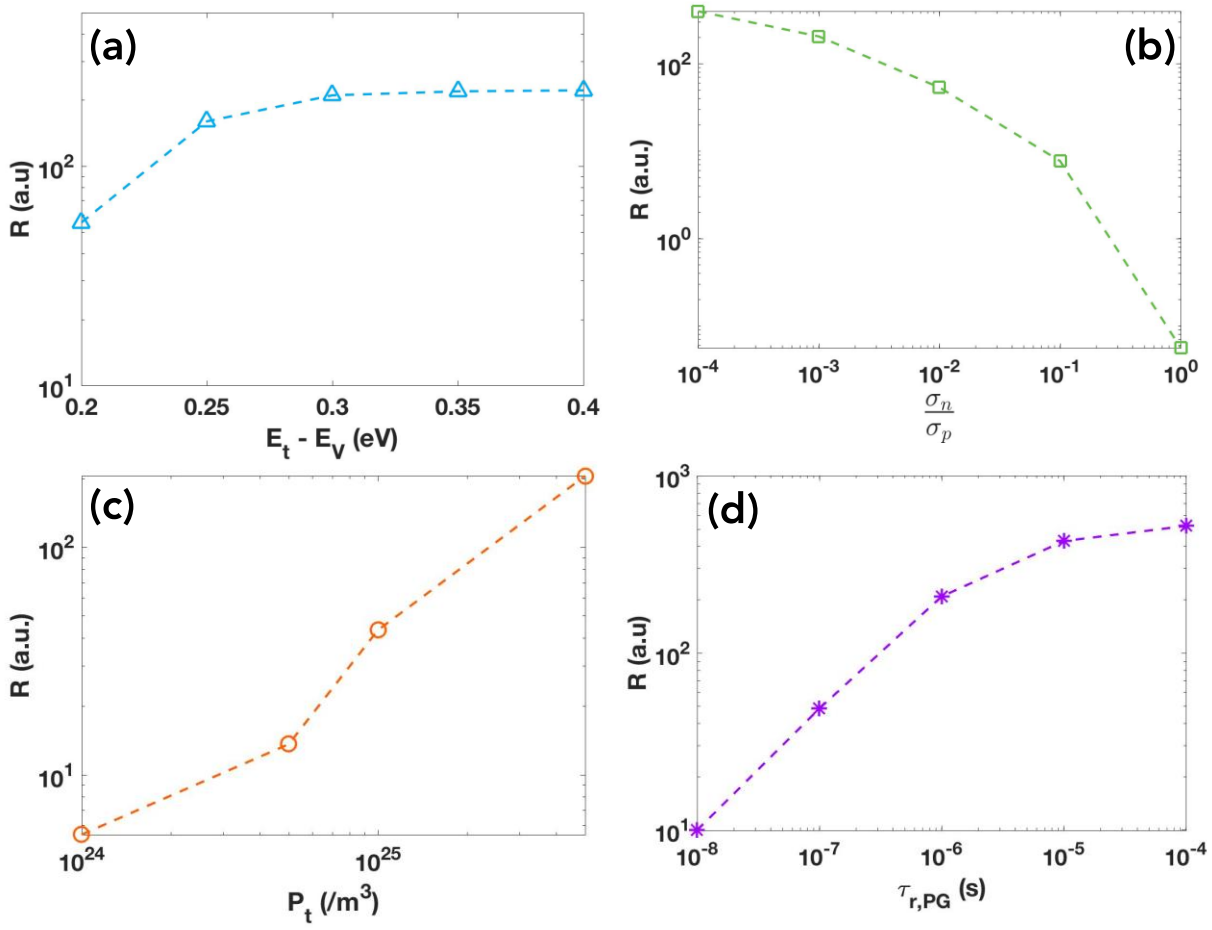

Figure 5.9 Photoresponsivity (R) as functions of (a) trap state position (E_t) with respect to the valence band edge (E_V), (b) capture cross-section ratio (σ_n/σ_p), (c) total trap concentration (P_t), and (d) recombination life time ($\tau_{r,PG}$). Nominal values of $E_t - E_V$ = 0.3 eV, σ_n/σ_p = 1e^{-3}, $P_t = 5 \times 10^{25}$ /m^3, and $\tau_{r,PG}$ = 1 μs are used. Incident power density, wavelength and gate voltage are P_{inc} = 20 mW/cm^2, λ = 405 nm, and V_G = 0.8 V, respectively.

So far, we have discussed the photoillumination effect of $MoSe_2$ phototransistors without changing the material properties, which however can vary based on experimental conditions. Therefore, we will investigate the impacts of trap energy (Figure 5.9(a)), capture cross section (Figure 5.9(b)), total trap concentration (Figure 5.9(c)), and recombination lifetime (Figure 5.9(d)) on the device performance. Figure 5.9(a) shows that R initially increases as trap states exist deeper in the band gap (i.e., as $E_t - E_V$ increases) since the deeper trap states are likely to have more number of holes than shallower states, which can also be seen from the occupational function for holes $(1 - f)$ or Figure 5.3(c). However, when $E_t - E_V \gg 0.3$ eV, the photoresponsivity will not be improved any further, which can also be understood from Figure 5.3(c) where the occupation function is not changed significantly between $F_{n,light}$ and $F_{p,light}$.

The shape of occupation function can be explained by the model introduced above. The f can be simplified as $v_{th}\sigma_p p/\left(v_{th}\sigma_n n_C + v_{th}\sigma_p p_V + e_p\right)$ because e_n is almost zero if the trap state is much closer to E_V than E_C. Under weak illumination, p_V is small, resulting in $v_{th}\sigma_p p_V \ll e_p$ and $1 - f \approx 1/\left(v_{th}\sigma_n n_C + e_p\right)$. n is not small but comparable value as much as e_p, due to small generation rate and σ_n/σ_p (default value is 10^{-3}). Then, e_p becomes sufficiently effective to control $1 - f$ by change of $E_t - E_V$, *i.e.* if $E_t - E_V$ increases, $p_{t,PG}$ increases, resulting in larger PG effect. This physically indicates that emission rate for holes out of the traps becomes weaker with increasing E_t, thereby holes stay longer there. When $e_p \ll v_{th}\sigma_n n_C$, R gradually saturates to a certain value which relies on ratio between capture cross section for electron and holes, σ_n/σ_p. Therefore, it is worth investigating dependence of R on σ_n/σ_p as shown in Figure 5.9(b). R decrease with decreasing σ_p (or increasing σ_n). It is intuitive that holes capture cross section are larger than that of electrons at a state in band gap close to valence band. However, despite of the same trap state location, $p_{t,PG}$ can decrease if cross section area captures are more likely to capture electrons into the state. Now, e_n cannot be ignored, and large $v_{th}\sigma_n n_C$ results in decreasing $1 - f$ and R. Figure 5.9(c) exhibits that PG effect becomes more powerful with increasing P_t. PG effect also depends on recombination carrier lifetime. The longer free holes stay in the energy bands, the more holes trap states can be captured, leading to PG effect as shown in in Figure 5.9(d). Shockley–Read–Hall (SRH) recombination at mid gap state is implicitly considered in the $\tau_{r,PG}$. Extremely long $\tau_{r,PG}$ have same effect as high P_{inc}, making $1 - f \approx 1$, and the state be fully occupied with holes, displaying the saturation in the Figure 5.9(d).

5.4 Conclusion

In summary, we simulated photoillumination effects in the monolayer $MoSe_2$ phototransistors. To reveal the key mechanisms of high photoresponse in the 2D materials-based phototransistors, trap model for PC and PG effects were embedded into the NEGF transport simulator. The simulation results demonstrated clear PC and PG characteristics, informing dominance of PG effect over PC effect in the device. Trend of the simulated transfer characteristics with significant threshold voltage shift was well matched with experimental observations. For further understanding of the PG effect, deep analysis from microscopic perspectives was done by plotting band diagram along with variation of energy barrier lowering and capture hole concentration depending on power and wavelength. To address overall device optical performance, photoresponsivity and specific detectivity were calculated and analyzed with respect to device and light source inputs. Finally, for improvement of the device performance, we examined the influence of material properties such as trap energy, capture cross sections, total trap concentration, and recombination lifetime on the photogain. The proposed quantum transport simulation can not only accurately predict the photoelectric performances of 2D $MoSe_2$ phototransistors but also deeply quantify and analyze the internal physical mechanisms, providing a useful platform for the manipulation and optimal design of the popular 2D photodetectors for a wide range of applications.

Chapter 6 Simulation for Optical Properties of Nano-patterned MoS_2 Phototransistors

6.1 Introduction

Even though the previous simulation method was used to analyze $MoSe_2$ phototransistors, its usage can be extended to phototransistors based on other types of channel materials. In fact, multilayer $MoSe_2$ with Mo-interstitial was applied as channel material, leading to significant PG effect, to overcome intrinsic limitation of optical properties of multilayer TMDs mainly due to indirect band gap. Following that, other materials or device engineering could be designed to strengthen the photoresponsivity or PG effect. Recently, some structural engineering of TMDs has intrigued lots of attention since those can be employed to improve the basic properties of materials [215]. Those include stacking of heterostructures [216], decoration with quantum dot [217], [218], and introduction of different alignment direction [219]. One of the attractive techniques of the structural engineering is nano-patterning. It can directly alter the band structure of materials, making it an appealing platform to adjust the optical and electrical properties of TMDs. Nanomesh-patterned multilayer MoS_2 was reported, demonstrating a large photoluminescence emission peak analogous to direct band gap monolayer MoS_2 [220]. However, underlying physics behind the uniquely patterned structure is still vague and its mechanisms for large responsivity can be theoretically uncovered.

In this chapter, material and device simulations of nano-patterned multilayer MoS_2, so-called MoS_2 nanomesh are presented to explain large photoresponsivity of indirect band gap MoS_2. Fabricated multilayer MoS_2 nanomesh phototransistors by my collaborator showed much larger photoresponsivity ($R \sim 123.7$ A/W) than that of reported direct band gap monolayer MoS_2 phototransistors, under similar incident illumination power intensities and wavelength [135], [142], [214]. In order to investigate the fundamental origin of this ultra-high photoresponsivity in our multilayer MoS_2 nanomesh phototransistors, the material structure and the device based on it were theoretically analyzed by the density functional theory (DFT), and the NEGF simulation based on multiple-trap state model, respectively.

6.2 MoS_2 Nanomesh

6.2.1 Atomistic Structure

Like Chapter 3 and Chapter 4, fabrication, characterization, and measurement of the multilayer MoS_2 nanomesh and the phototransistors were conducted by my experimental collaborators, Heekyeong Park, Young Jun Kim, Young-Hoon Kim, Young-Min Kim in Professor Sunkook Kim's group in Sungkyunkwan University. The patterned hexagonal array of hexagon holes on patterned MoS_2 was observed. To identify atomistic structure of the inside edges of the hexagonal holes in the MoS_2 nanomesh, they scrutinized them and their atomic configuration of the multilayer MoS_2 showing stacking sequences. A typical hexagonal shape of the hole in the MoS_2 nanomesh was observed. Selected area diffraction pattern (SADP) for the region of MoS_2 multilayers showed 2H-MoS_2 structure with AA' stacking configuration mixed with Mo and S atoms. By comparing corresponding atomic models, it is revealed that the hole edges mainly have a zigzag configuration of atomic columns. In their fabrication process, specific dry etching and wet etching were performed, where the different edges gradually changed to energetically stable structure. In general, MoS_2 have two edge types of zigzag and armchair [221], [222]. Most of the MoS_2 edges were formed as zigzag edges in our experiment because the zigzag structure is more energetically favorable than the armchair structure [223], [224]. Wulff construction rule [225], [226], implying that specific crystal shapes are likely built over others, relying on their surface energy minimization effect, established the expanded edges converged to a hexagonal shape. Considering the AA' stacking configuration of the MoS_2 sample, the exposed atomic terminations on every edge of the hexagonal holes are a mixture of Mo-terminated and S-terminated zigzag structure by layer.

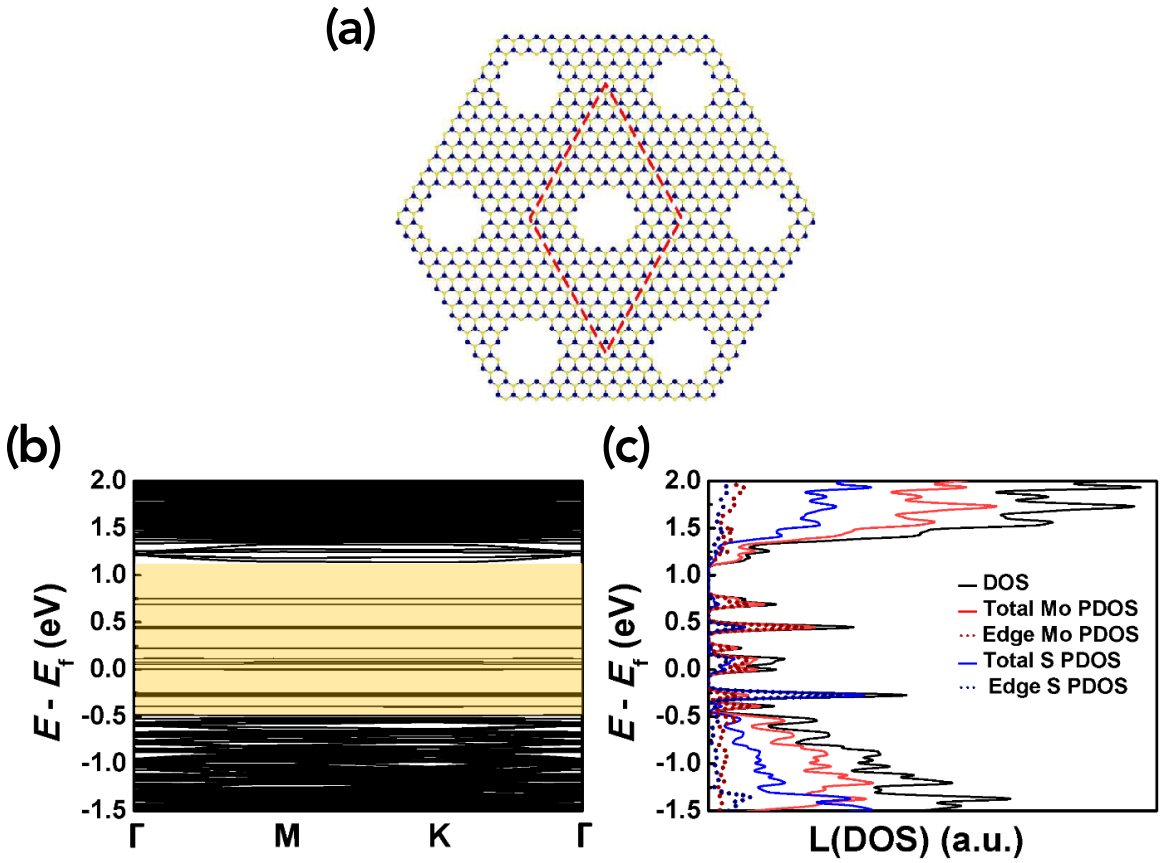

Figure 6.1 Electronic properties of MoS_2 nanomesh. (a) The crystal structure of MoS_2 nanomesh for DFT calculation (the cell considered for the DFT calculation is shown in the dashed diamond). The diameter of holes and the spacing between the holes are the same as 1.6 nm. (b) Band structure of MoS_2 nanomesh showing the formation of in-gap states (highlighted region). (c) DOS and Partial density-of-states (PDOS) of the MoS_2 nanomesh showing the contribution of edge Mo and edge S atoms on the total DOS. It is evident that the edge Mo and edge S atoms are the main contributors to the formation of the in-gap states. Total Mo and total S PDOS shows the contribution of all Mo atoms and S atoms, respectively.

6.2.2 Material Simulation

As opposed to a prefect crystal, the nanomesh structure can have an irregular band structure. To investigate its electronic states, DFT calculation was performed on the MoS_2 nanomesh, which was conducted based on plane-wave (PW) approximation using Quantum ESPRESSO. Perdew–Burke–Ernzerhof (PBE) generalized gradient approximation (GGA)-based exchange correlation function with projector augmented wave pseudopotential was used. The kinetic energy cutoff of the wavefunction was chosen to be 25 Ry. Due to the large size of simulation, monolayer MoS_2 nanomesh was simulated with a supercell containing 264 atoms (88 Mo atoms and 176 S atoms) as shown in Figure 6.1(a). The supercell has an edge length of 32 Å (with an area of 862 $Å^2$) and 15 Å of spacing distance in the out-of-plane direction to screen images interaction. Although we have used a monolayer MoS_2 nanomesh to make the simulation computationally manageable, the conclusion derived by the DFT simulation will not change for the multilayer counterpart, and both Mo-terminated and S-terminated zigzag edges were considered to match the experimental observation. Figure 6.1(b) presents the electronic structure of the MoS_2 nanomesh supercell, which exhibits a formation of in-gap states throughout the band gap as shown in the highlighted region. Partial density-of-states (PDOS) analysis (Figure 6.1(c)) clearly shows that the edge atoms are the main contributors to the in-gap states rather than the atoms far from the edges. In particular, edge Mo atoms contribute dominantly to the in-gap states near the conduction band (E_C), whereas it is a mixed contribution of edge Mo and edge S atoms near the valence band (E_V), which is in agreement with a previous report [227].

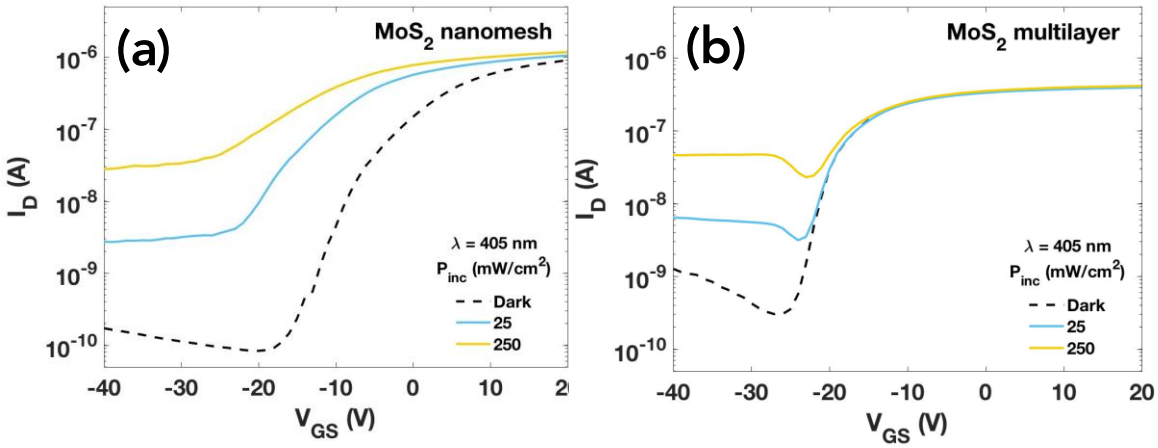

Figure 6.2 Photoresponsive characteristics of phototransistors based on (a) MoS_2 nanomesh and (b) pristine MoS_2 under illumination of λ_{ex} of 405 nm with various P_{inc}.

6.3 MoS_2 Nanomesh Phototransistors

6.3.1 Device Characterization

The existence of the in-gap states can have effect on optoelectronic properties of devices based on the materials. A multilayer MoS_2 nanomesh TFT was fabricated to investigate its photoresponsive characteristics. Source and drain contacts were deposited on the channel material with area of 34.28 cm^2. Figure 6.2(a) is measured I_D–V_{GS} characteristics under light illumination of various incident power intensities (P_{inc}) at a wavelength (λ_{ex}) of 405 nm and drain voltage (V_{DS}) of 1 V. It should be noted that increase of the OFF-state current under irradiation is significant compared to that of natural multilayer MoS_2 TFT with channel area of 56.28 um^2 (Figure 6.2(b)). The notable current enhancement could be understood by increased conductivity due to photogenerated excess carriers (PC effect). At the same time, MoS_2 nanomesh phototransistor demonstrates PG effect same as multilayer $MoSe_2$ phototransistors discussed in the Chapter 4. The photocurrent of the MoS_2 nanomesh TFT is the remarkably larger in ON-state current than pristine MoS_2 TFT counterpart. From Figure 6.2 (b) and (c), R is calculated of MoS_2 nanomesh and pristine MoS_2 TFTs with various P_{inc} and $\lambda_{ex} = 405$ and 638 nm. The maximum photoresponsivity value is 123.7 A/W which is ~330 times larger than that of pristine MoS_2 phototransistor at $P_{inc} = 8\ \mathrm{mW/cm^2}$ and $\lambda_{ex} = 405$ nm.

6.3.2 Device Simulation

6.3.2.1 Nominal Device

It can be expected that the large I_{ph}, and R of the MoS_2 nanomesh phototransistors are mainly attributed to the in-gap states. In order to develop further insight into the MoS_2 nanomesh phototransistor exhibiting excellent optical properties, quantum transport simulation was performed considering the trap states, which can capture electrons or holes. Carrier transport through the MoS_2 nanomesh phototransistor was simulated using the NEGF formalism within an effective mass approximation (m^* = 0.45 m_0; m_0 being free electron mass). For the nominal device, 50 nm-long, 6.2 Å-thick MoS_2 channel and 2.5 nm-thick SiO_2 gate dielectric were used in a bottom-gated Schottky barrier (SB) FET structure with an SB height of 0.1 eV. Power supply voltage $V_{DD} = 0.5$ V was used. Here, we have used smaller device dimensions to save simulation time; however, it will not affect key underlying physics and the conclusion of this study will remain the same. Transport equation was solved iteratively with the Poisson's equation until the self-consistent solution was achieved. It should be noted that, here we performed a ballistic transport simulation assuming an ideal MoS_2 to identify underlying physics generating the PG effect first (Figure 6.4(a)–(c)), and then, the current degradation due to scattering in the actual nanomesh structure has been treated by calibrating simulation results against experiments (Figure 6.4(d)), using a fitting parameter (current degradation factor of 8×10^{-6}).

6.3.2.2 Trap Model

Trap model for PC effect applied in the MoS_2 nanomesh phototransistors is basically same as model introduced in Chapter 5. A modified Hornbeck–Haynes model was used as $\Delta\sigma = q\mu_n\Delta n_{PC} + q\mu_p\Delta p_{PC}$, where μ_n, μ_p, Δn_{PC}, and Δp_{PC} are electron and hole mobility, excess electron and hole densities in the conduction and valence band, respectively. I have used the measured carrier mobility for both μ_n and μ_p, listed in Table 6.1. Same as Chapter 5 which has a trap state near E_V, $\Delta p_{PC} = g\tau_{r,PC}$ and $\Delta n_{PC} = \Delta n_{PC} + p_{t,PC}$, considering charge neutrality. $p_{t,PC}$ is the trapped hole density which can be calculated as $p_{t,PC} = \frac{P_t d g \tau_{r,PC}}{g\tau_{r,PC} + P_t d \tau_{t,p}/\tau_{g,p}}$, where P_t is the total trap concentration, g ($= \eta P_{abs}/h\nu$) is the generation rate of excess carriers, d is the thickness of MoS_2 nanomesh, and $\tau_{r,PC}$ is carrier recombination lifetime. η and $h\nu$ are internal quantum efficiency and single photon energy, respectively. The same internal quantum efficiency was used as Chapter 5. P_{abs} is the absorbed power density, given by $P_{inc}\left(1 - \left(e^{-a^{\perp}d} + e^{-a^{\parallel}d}\right)/2\right)$, where P_{inc} is incident power density, $a^{\perp}$ and $a^{\parallel}$ are

the absorption coefficient in the vertical and lateral direction, respectively. $\tau_{t,p}$ and $\tau_{g,p}$ are the trapping and escaping time of holes into and from the trap states, respectively, and $\tau_{t,p}/\tau_{g,p}$ ratios can be obtained by $1/\left(\frac{P_t}{N_V} exp \frac{E_t - E_V}{kT}\right)$ [196], where N_V is effective density-of-states at the conduction band edge and E_t is trap state. The same recombination lifetime was assumed as Chapter 5. Finally, photoconductive current ($I_{ph,PC}$) was obtained by $I_{ph,PC} = \frac{1}{L} V_{DS} \Delta\sigma$. The important material parameters are listed in Table 6.1. On the other hand, for PG effect in the MoS_2 nanomesh phototransistors, the identical trap model introduced in Chapter 5 was utilized. Occupational function, f, is modeled as $f = \frac{v_{th}\sigma_n n_C + e_p}{v_{th}\sigma_n n_C + e_n + v_{th}\sigma_p p_V + e_p}$, where v_{th}, n_C, p_V, σ_n, and σ_p are thermal velocity, free electron concentration in the conduction band, free hole concertation in the valence band, electron and hole capture cross sections, respectively. e_n and e_p are emission rate for electrons and holes from traps, respectively, and defined as $e_n = v_{th}\sigma_n n_0 exp\{(E_t - E_{F0})/kT\}$ and $e_p = v_{th}\sigma_p p_0 exp\{(E_{F0} - E_t)/kT\}$. n_0 and p_0 are free electron concentration at conduction band and free hole concentration at valence band under equilibrium, respectively, which can be obtained by Fermi-Dirac integral for order of 0 since the carriers are distributed in 2D material. Those are expressed as $n_0 = N_c\, ln[1 + exp\{(E_{F0} - E_C)/kT\}]$ and $p_0 = N_V\, ln[1 + exp\{(E_V - E_{F0})/kT\}]$ where E_{C} is conduction band minima and N_C is effective density-of-states at E_C. E_{F0} is thermal equilibrium Fermi level assumed to be mid-gap in the $MoSe_2$ nanomesh. n_C is obtained by $n_C = n_{inj} + \Delta n_{ph}$ where n_{NEGF} is self-consistently simulated electron concentration by NEGF simulator and $\Delta n_{ph} = g\tau_{r,PG}/d$ is generated electron concentration. Under illumination, p_V becomes close to generated hole concentration, $p_V \cong \Delta p_{PG} = \Delta n_{PG}$. Finally, concentration of captured holes is calculated by $p_{\mathrm{t,PG}} = P_{\mathrm{t}}(1 - f)$

λ [nm]	η	$\alpha^{\perp}$ [202] [/cm]	$\alpha^{\parallel}$ [202] [/cm]	$\tau_{r,PC}$ [196] [ps]	$\tau_{r,PG}$ [203] [μs]	μ_n, μ_p [$\mathrm{cm^2/V \cdot s}$]	P_t [$/\mathrm{m^3}$]
405	0.5	18.9×10^4	102.5×10^4	100	1	2.68	5×10^{25}

Table 6.1 Material parameters used for MoS_2 nanomesh phototransistor

For MoS_2 nanomesh, there are multiple trap states in the band gap. These might be different effect on device performance from in case of $MoSe_2$. Now, trap model should be modified to consider the multiple states effect. PC model in case of a trap states near E_C uses $\Delta n_{PC} = g\tau_{r,PC}$ and $\Delta p_{PC} = \Delta n_{PC} + n_{t,PC}$ for charge neutrality, assuming that Fermi level is located at the mid-level of the band gap. Density of trapped electrons in the trap states can be obtained by $n_{t,PC} = \frac{P_t d g \tau_{r,PC}}{g\tau_{r,PC} + P_t d \tau_{t,n}/\tau_{g,n}}$, where $\tau_{t,n}$ and $\tau_{g,n}$ are trapping and escaping time of electrons into and from the trap states, respectively, and $\tau_{t,n}/\tau_{g,n}$ can be calculated by $\frac{\tau_{t,n}}{\tau_{g,n}} = 1/\left(\frac{P_t}{N_C} exp \frac{E_C - E_t}{kT}\right)$ [196]. For PG effect in the MoS_2 nanomesh phototransistors, the whole model is same as one introduced in Chapter 5, except that level of E_t could be varied and even close to the conduction band. Also, number of occupational functions at the trap states could be more than one, where captured hole concentration can be expressed as

$$p_{t,PG} = \sum_i P_{t,i}(E_{t,i})\big(1 - f(E_{t,i})\big). \tag{6.1}$$

The occupational function (f) is strong function of capture cross section ratio (σ_n/σ_p), since it determines capturing rate of carriers in the defects. In the previous chapter, σ_n/σ_p was assumed to be constant which is independent of energy (see Figure 6.3(a) and (b)). However, it is intuitive that practical capture cross section for electrons is large at energy close to E_C, while capture cross section for holes is large at energy near E_V. Therefore, σ_n/σ_p is strong function of energy. This ratio is assumed to be a logistic function of energy in a logarithmic scale with maximum and minimum value of 10^3 and 10^{-3} at the conduction band and the valence band edge, respectively as shown in Figure 6.3(c) and (d). The dependence of shape of occupational function on capture cross section ratio is also shown.

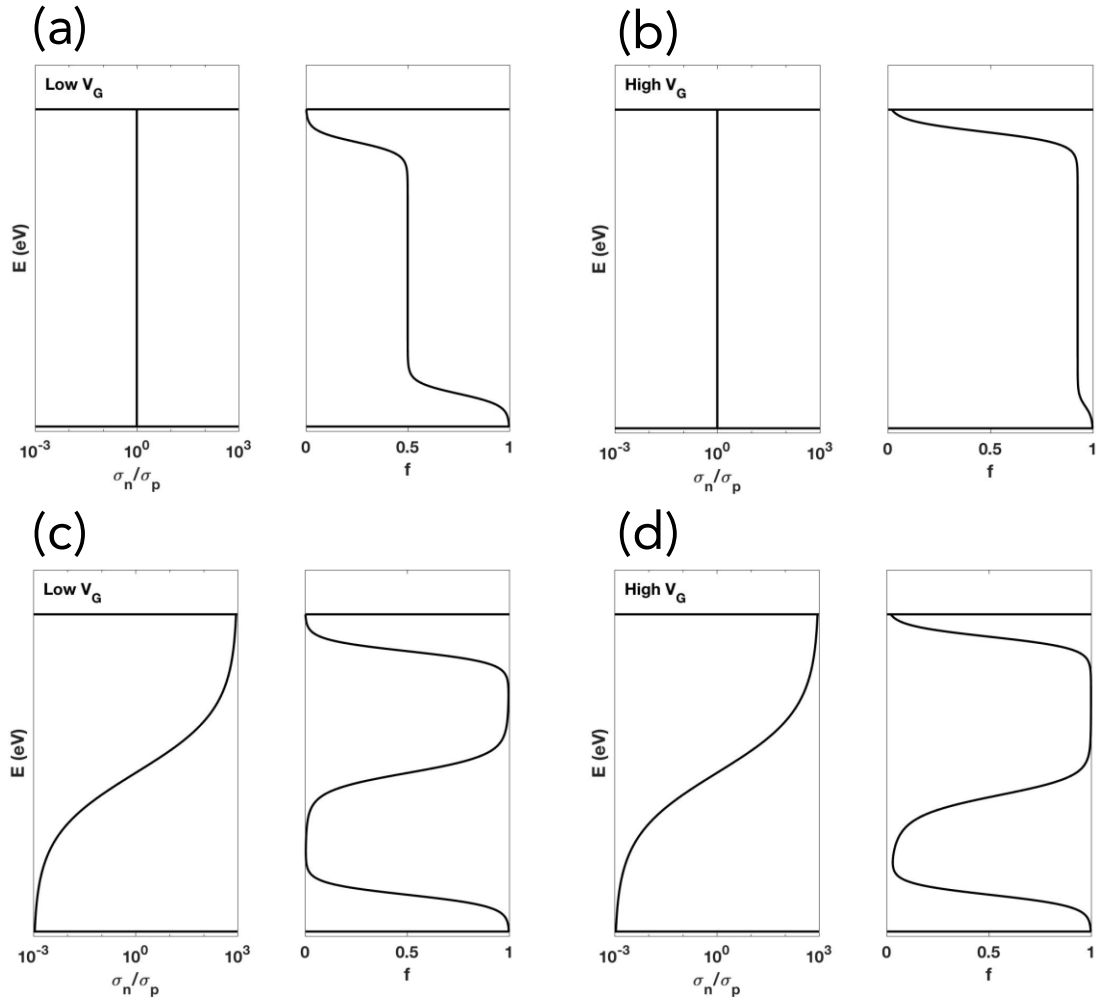

Figure 6.3 Left panels and right panels of each (a)–(d) are ratio of capture cross sections of electrons to holes (σ_n/σ_p), and occupational function (f) under light illumination, respectively. f with constant ratio ($\sigma_n/\sigma_p = 1$) at (a) low V_G and (b) high V_G, and f with varying ratio depending on energy at (c) low V_G and (d) high V_G.

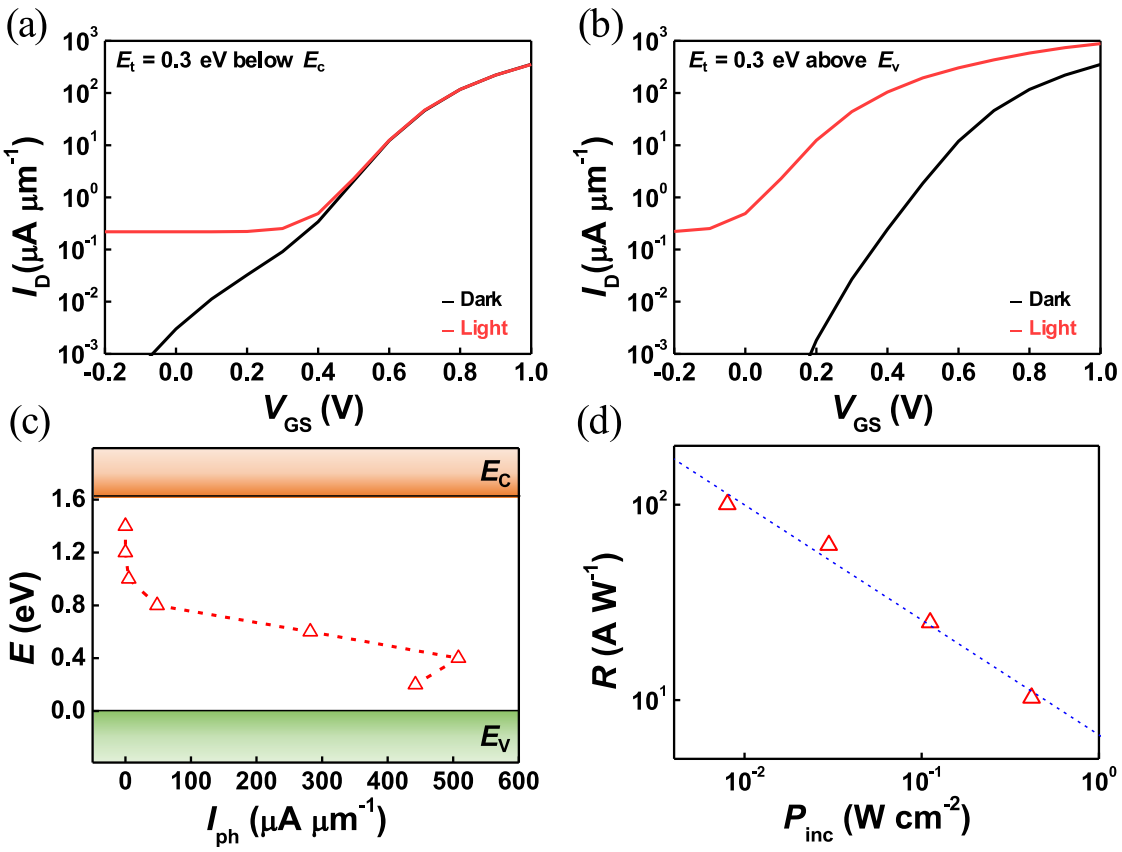

Figure 6.4 Simulation of photoresponse behaviors of the MoS_2 nanomesh phototransistor. (a) and (b) I_D–V_{GS} characteristics of MoS_2 nanomesh phototransistor assuming a single trap state (trap density of $P_t = 5 \times 10^{25}$ /m^3 near (a) E_C and (b) E_V, at dark and under illumination (λ_{ex} = 405 nm, P_{inc} = 417 mW/cm^2). (c) I_{ph} variation at different trap states (E_t) inside the band gap (E_t from 0.2 to 1.4 eV above E_V) at V_{GS} = 1 V. (d) Photoresponsivity (R) as a function of P_{inc} at λ_{ex} of 405 nm with trap states at four different energy levels. E_t = 0.3 and 0.4 eV above (below) E_V (E_C). The total trap density is kept the same as in (a)–(c) (1.25×10^{25} /m^3 each).

6.3.2.3 Results

As demonstrated by the DFT calculation in Figure 6.1(b), the MoS_2 nanomesh contains multiple-states within the band gap. However, only few states at certain energy levels might be the key contributors to the large photoresponsivity. To test this hypothesis, we have simulated I_D–V_{GS} characteristics of MoS_2 nanomesh phototransistor at dark and under illumination ($P_{inc} = 417\ \mathrm{mW/cm^2}$; $\lambda_{ex} = 405\ \mathrm{nm}$), assuming a single trap state (trap concentration of $P_t = 5 \times 10^{25}\ /\mathrm{m^3}$) near the conduction band (E_C) and the valence band (E_V) in Figure 6.4(a) and (b), respectively. A notable observation from the simulated I_D–V_{GS} curves is that, with the gap state near E_V, significant threshold voltage (V_{th}) shift can be observed (Figure 6.4(b)), while it is not the case with the trap state near E_C (Figure 6.4(a)). When V_{GS} is high, due to the large number of electrons in the conduction band, the trap state near E_C is fully filled with electrons both at dark and under illumination. On the contrary, the trap state near E_V is fully occupied by electrons at dark, but it can be partially filled with holes under illumination due to the increased hole concentration with the generated excess holes (see Figure 6.3(d)), resulting in potential barrier lowering and the PG effect. The simulated I_D–V_{GS} characteristics with the trap state near E_C or E_V (Figure 6.4(a) and (b)) manifest same trend as measured I_D–V_{GS} of pristine MoS_2 and MoS_2 nanomesh, respectively, clearly indicating that only the gap states near E_V can play an important role for PG effect, increasing the electron injection from the source significantly. To examine the overall trend with different trap states (E_t), we have calculated photocurrent (I_{ph}) by varying E_t from 0.2 eV to 1.4 eV above E_V, as shown in Figure 6.4(c), which exhibits I_{ph} being significant only when the trap states are located near the valence band ($E_t - E_V \leq 0.8$ eV). Lastly, we have plotted photoresponsivity as function of P_{inc} in Figure 6.4(d). To emulate the material property of the real MoS_2 nanomesh including multiple trap states at different E_t, here, we have considered trap states at four different energy levels ($E_t = 0.3$ and 0.4 eV above E_V and below E_C) with the trap concentration of $1.25 \times 10^{25}\ /\mathrm{m^3}$ each. Simulated photoresponsivity could exhibits the same trend as experiments (Figure 6.4(d)), indicating that our model, simulation results and analysis are good representations of the experimental observation.

6.4 Conclusion

Nano-patterning of nanomaterials demonstrated significant optical properties of materials. The nanomesh patterns on multilayer MoS_2 phototransistors achieved greater advances in photoresponsivity than normal multilayer MoS_2 phototransistors. We revealed that the exposed-zigzag edges introduce the trap states in the band gap region, especially, the trap states near E_V result on the PG effect, thus improving the performances of phototransistors. Theses advanced experimental analysis and rigorous simulations propose that nano-patterning method on TMDs will provide a novel route to develop nanomaterials for various optoelectronic applications.

Chapter 7 Conclusion

7.1 Summary

I presented analytical modeling and numerical simulation framework capable of capturing photoillumination effects of two-dimensional (2D) $MoSe_2$ phototransistors. First of all, I introduced modern trends of metallic, semiconducting, and insulating 2D materials along with its applications including photo sensors. For simulation methods, among a few simulation methods presented, quantum transport in nano-scale devices using non-equilibrium Green's function (NEGF) formalism was used for this study. Two main methods for electronic states in the NEGF; effective mass and tight-binding approximations were compared each other. To improve limitations of both approximations, I presented modified effective mass approximation to have accurate transport calculation and fast computation.

To unveil key origin of large photoresponse of fabricated $MoSe_2$ phototransistors, I quantified density-of-states in the $MoSe_2$ phototransistors through temperature-dependent analysis, revealing presence of significant amount of density-of-states in the device. I modeled two main mechanisms of photoillumination effects; photoconductive (PC) and photogating (PG) effects. PC model well explained conductivity increase due to excess generated carriers, and PG model was derived to represent injection of electrons from sourced by lowered energy barrier due to trapped holes. This successfully reproduced experimentally measured photoresponsivity of CVD-grown $MoSe_2$ phototransistors fabricated under Mo-rich condition with a few fitting parameters, informing that, due to mainly PG effect, trap states induced by the Mo-interstitial atoms significantly enhance photoresponsivity under illumination. For more precise understanding of the effects, I created a stand-alone quantum transport simulator where both effects were embedded. PC effect adapted a modified Hornbeck−Haynes model, while PG effect was realized by NEGF transport along with a trap model which can calculate occupational function of the trap state. Simulation results confirmed that PG effect is dominant over PC effect in the $MoSe_2$ phototransistor, followed by in-depth analysis of the band diagram, barrier lowering, and captured hole concentration. The results also displayed almost same trends of photoresponsivity and specific detectivity as those of the fabricated $MoSe_2$ phototransistors. According to the simulation results, further improvement can be achieved by engineering material properties. I simulated effects of the material properties on photoresponsivity, such as trap states, total trap concertation, capture cross sections, and recombination lifetime on photoresponsivity.

Also, the simulator developed for $MoSe_2$ phototransistors can be extended to explore other types of 2D material. I simulated photoillumination effects of MoS_2 nanomesh phototransistors. Band structure plotted by density functional theory (DFT) indicates that the channel material has multiple in-gap states due to intentionally patterned hexagonal arrays in the MoS_2 layers, while the CVD-grown $MoSe_2$ approximated to have single trap state close to the valence band was simulated previously. To reveal which trap states has a critical role in PG effect, phototransistors with trap state near the conduction band and the valence band were simulated and compared separately. The results showed that only high threshold voltage shift and photocurrent in the device with trap states close enough to the valence band. Lastly, a device with multiple-states in the band gap was simulated to reproduce the trend of measured photoresponsivity.

This work will significantly advance the field by generating new material performance knowledge and providing critical insights into novel sensor designs. It will address formidable challenges in 2D-material flexible photodetectors for next-generation wearable sensors, making this research highly relevant and opportune. The core knowledge and technologies developed in this project will provide advances that will help to elevate Canada's profile in the global sensor industry, growing at a compound annual growth rate of 11.8% ($123B in 2016; $240B expected in 2022) [228]. In addition, the knowledge and techniques created can be extended to other sectors, opening up new markets such as interactive gaming, mobile security and mobile healthcare systems.

7.2 Future Work

For the future study of the present work, I suggest several interesting topics as follows:

1. Phototransistors with more than one-layer $MoSe_2$ as actual fabricated multilayer $MoSe_2$ can be simulated. This can be done by tight-binding approximation considering intralayer hopping parameters. Those parameters can be extracted by *ab-initio* calculation such as DFT. Since device simulation time could be extensively long due to large size of Hamiltonian matrix, size of unit cell and number of bases used in the DFT simulation should be carefully chosen. At the same time, we can insert trap states in the electronic states to introduce Mo-interstitials in the atomistic structure to have effects of trap states on the transport calculation. This might result in leakage dark current at low gate voltage, which decrease photocurrent, so that it is worth investigating trade-off between photocurrent increase due to photoillumination effect and degradation due to trap states in the band structure.

2. Scattering can be considered in the NEGF simulation. The scattering can come from many sources: defects, phonons, and (e–e) interaction. Except for the latter, the scattering mechanisms can be included either explicitly in the Hamiltonian to account for defects, or it can be included as a perturbation self-energy in the case of electron–phonon interactions. Such scattering mechanisms complicate the model, and might require more computational resources. In addition, the e–e scattering is not negligible due to the large density of charge injected from source lead. For that, Hartree approximation might be used assuming that each electron moves independently and sees only the average field generated by all the other electrons.

3. Transient response can be simulated for optical switching performance. According to recent literatures about 2D photodetectors [134], photodetectors based on semiconducting layered materials reports a large (about 10 orders of magnitude) variance in their photoresponsivity. Regarding the response time, it appears that most of devices show response times much larger than$\sim 1 \times 10^{-4}$ ms which is response time of commercialized conventional silicon photodiode. The photoresponsivity and response time are trade-off each other since the relatively long response times are due to the presence of long-lived carriers in the trap states (in devices with responsivity above $1\ \mathrm{A/W}$). Therefore, further investigation to improve the response time maintaining large photoresponsivity should be done with transient response simulation. To do that, time-dependent density functional theory or quantum master approaches can be used.

Bibliography

[1] J. W. May, "Platinum surface LEED rings," *Surf. Sci.*, vol. 17, no. 1, pp. 267–270, 1969.

[2] A. J. Van Bommel, J. E. Crombeen, and A. Van Tooren, "LEED and Auger electron observations of the SiC (0001) surface," *Surf. Sci.*, vol. 48, no. 2, pp. 463–472, 1975.

[3] K. S. Novoselov *et al.*, "Electric field effect in atomically thin carbon films," *Science (80-.).*, vol. 306, no. 5696, pp. 666–669, 2004.

[4] James Hedberg, "Image of graphene atomic view.," 2015. [Online]. Available: http://www.jameshedberg.com/scienceGraphics.php?sort=all&id=graphene-atomic-structure-sheet.

[5] K. S. Kim *et al.*, "Large-scale pattern growth of graphene films for stretchable transparent electrodes.," *Nature*, vol. 457, no. 7230, pp. 706–710, 2009.

[6] A. Reina *et al.*, "Large area, few-layer graphene films on arbitrary substrates by chemical vapor deposition," *Nano Lett.*, vol. 9, no. 1, pp. 30–35, 2009.

[7] C. Berger *et al.*, "Electronic confinement and coherence in patterned epitaxial graphene.," *Science*, vol. 312, no. 5777, pp. 1191–1196, 2006.

[8] J. Kedzierski *et al.*, "Epitaxial graphene transistors on SiC substrates," *IEEE Trans. Electron Devices*, vol. 55, no. 8, pp. 2078–2085, 2008.

[9] P. Avouris, "Graphene: Electronic and photonic properties and devices," *Nano Lett.*, vol. 10, no. 11, pp. 4285–4294, 2010.

[10] F. Schwierz, "Graphene transistors," *Nat. Nanotechnol.*, vol. 5, no. 7, pp. 487–496, Jul. 2010.

[11] J.-H. Chen, C. Jang, S. Xiao, M. Ishigami, and M. S. Fuhrer, "Intrinsic and extrinsic performance limits of graphene devices on SiO_2," *Nat. Nanotechnol.*, vol. 3, no. 4, pp. 206–209, 2008.

[12] F. Chen, J. Xia, D. K. Ferry, and N. Tao, "Dielectric screening enhanced performance in graphene FET," *Nano Lett.*, vol. 9, no. 7, pp. 2571–2574, 2009.

[13] S. V. Morozov *et al.*, "Giant intrinsic carrier mobilities in graphene and its bilayer," *Phys. Rev. Lett.*, vol. 100, no. 1, p. 016602, 2008.

[14] A. Geim, "Graphene update," *Bulletin of the American Physical Society*, 2010. [Online].

Available: http://meetings.aps.org/link/BAPS.2010.MAR.J21.4.

[15] M. Y. Han, B. Özyilmaz, Y. Zhang, and P. Kim, "Energy band-gap engineering of graphene nanoribbons," *Phys. Rev. Lett.*, vol. 98, no. 20, pp. 1–4, 2007.

[16] P. Kim, M. Y. Han, A. F. Young, I. Meric, and K. L. Shepard, "Graphene nanoribbon devices and quantum heterojunction devices," *2009 IEEE Int. Electron Devices Meet.*, pp. 241–244, 2009.

[17] E. Rotenberg, A. Bostwick, T. Ohta, J. L. McChesney, T. Seyller, and K. Horn, "Origin of the energy bandgap in epitaxial graphene.," *Nat. Mater.*, vol. 7, no. 4, pp. 258–259, 2008.

[18] S. Y. Zhou *et al.*, "Substrate-induced band gap opening in epitaxial graphene," *Nat. Mater.*, vol. 6, no. 10, pp. 770–775, 2007.

[19] S. Kim, J. Ihm, H. J. Choi, and Y.-W. Son, "Origin of anomalous electronic structures of epitaxial graphene on silicon carbide," *Phys. Rev. Lett.*, vol. 100, no. 17, p. 176802, 2008.

[20] A. Bostwick, T. Ohta, T. Seyller, K. Horn, and E. Rotenberg, "Quasiparticle dynamics in graphene," *Nat. Phys.*, vol. 3, no. 1, pp. 36–40, 2007.

[21] X. Peng and R. Ahuja, "Symmetry breaking induced bandgap in epitaxial graphene layers on SiC," *Nano Lett.*, vol. 8, no. 12, pp. 4464–4468, 2008.

[22] E. Sano and T. Otsuji, "Theoretical evaluation of channel structure in graphene field-effect transistors," *Jpn. J. Appl. Phys.*, vol. 48, no. 4, pp. 0–5, 2009.

[23] V. M. Pereira, A. H. C. Neto, and N. M. R. Peres, "Tight-binding approach to uniaxial strain in graphene," *Phys. Rev. B*, vol. 80, no. 4, p. 045401, 2009.

[24] Z. H. Ni, T. Yu, Y. H. Lu, Y. Y. Wang, Y. P. Feng, and Z. X. Shen, "Uniaxial strain on graphene: Raman spectroscopy study and band-gap opening," *ACS Nano*, vol. 2, no. 11, pp. 2301–2305, 2008.

[25] F. Sols, F. Guinea, and A. H. C. Neto, "Coulomb blockade in graphene nanoribbons," *Phys. Rev. Lett.*, vol. 99, no. 16, p. 166803, 2007.

[26] M. Y. Han, J. C. Brant, and P. Kim, "Electron transport in disordered graphene nanoribbons," *Phys. Rev. Lett.*, vol. 104, no. 5, p. 056801, 2010.

[27] X. Li, X. Wang, L. Zhang, S. Lee, and H. Dai, "Chemically derived, ultrasmooth graphene

nanoribbon semiconductors.," *Science*, vol. 319, no. 5867, pp. 1229–1232, 2008.

[28] Z. Chen, Y.-M. Lin, M. J. Rooks, and P. Avouris, "Graphene nano-ribbon electronics," *Phys. E*, vol. 40, pp. 228–232, 2007.

[29] L. Yang, C.-H. Park, Y.-W. Son, M. L. Cohen, and S. G. Louie, "Quasiparticle energies and band gaps in graphene nanoribbons," *Phys. Rev. Lett.*, vol. 99, no. 18, p. 186801, 2007.

[30] M. Evaldsson, I. V. Zozoulenko, H. Xu, and T. Heinzel, "Edge-disorder-induced Anderson localization and conduction gap in graphene nanoribbons," *Phys. Rev. B*, vol. 78, no. 16, p. 161407, 2008.

[31] E. V. Castro *et al.*, "Biased bilayer graphene: Semiconductor with a gap tunable by the electric field effect," *Phys. Rev. Lett.*, vol. 99, no. 21, p. 216802, 2007.

[32] P. Gava, M. Lazzeri, A. M. Saitta, and F. Mauri, "Ab initio study of gap opening and screening effects in gated bilayer graphene," *Phys. Rev. B*, vol. 79, no. 16, p. 165431, 2009.

[33] T. Ohta, A. Bostwick, T. Seyller, K. Horn, and E. Rotenberg, "Controlling the electronic structure of bilayer graphene.," *Science*, vol. 313, no. 5789, pp. 951–954, 2006.

[34] Y. Zhang *et al.*, "Direct observation of a widely tunable bandgap in bilayer graphene.," *Nature*, vol. 459, no. 7248, pp. 820–823, 2009.

[35] H. Raza and E. C. Kan, "Armchair graphene nanoribbons: Electronic structure and electric-field modulation," *Phys. Rev. B*, vol. 77, no. 24, p. 245434, 2008.

[36] Q. H. Wang, K. Kalantar-Zadeh, A. Kis, J. N. Coleman, and M. S. Strano, "Electronics and optoelectronics of two-dimensional transition metal dichalcogenides.," *Nat. Nanotechnol.*, vol. 7, no. 11, pp. 699–712, Nov. 2012.

[37] B. Radisavljevic, A. Radenovic, J. Brivio, V. Giacometti, and A. Kis, "Single-layer MoS_2 transistors," *Nat. Nanotechnol.*, vol. 6, no. 3, pp. 147–150, Mar. 2011.

[38] K. S. Novoselov *et al.*, "Two-dimensional atomic crystals," *Proc. Natl. Acad. Sci. U. S. A.*, vol. 102, no. 30, pp. 10451–10453, 2005.

[39] M. M. Benameur, B. Radisavljevic, J. S. Héron, S. Sahoo, H. Berger, and a Kis, "Visibility of dichalcogenide nanolayers.," *Nanotechnology*, vol. 22, no. 12, p. 125706, 2011.

[40] J. N. Coleman *et al.*, "Two-dimensional nanosheets produced by liquid exfoliation of layered

materials.," *Science*, vol. 331, no. 6017, pp. 568–571, 2011.

[41] S. Najmaei *et al.*, "Vapour phase growth and grain boundary structure of molybdenum disulphide atomic layers," *Nat. Mater.*, vol. 12, no. 8, pp. 754–759, 2013.

[42] A. M. van der Zande *et al.*, "Grains and grain boundaries in highly crystalline monolayer molybdenum disulphide," *Nat. Mater.*, vol. 12, no. 6, pp. 554–61, 2013.

[43] A. Kuc, N. Zibouche, and T. Heine, "Influence of quantum confinement on the electronic structure of the transition metal sulfide TS_2," *Phys. Rev. B*, vol. 83, no. 24, p. 245213, 2011.

[44] K. K. Kam and A. Parklnclon ', "Detailed Photocurrent Spectroscopy of the Semiconducting Group VI Transition Metal Dichalcogenides," *J. Phys. Chem*, vol. 86, pp. 463–467, 1982.

[45] A. Splendiani *et al.*, "Emerging Photoluminescence in Monolayer MoS_2," *Nano Lett.*, vol. 10, no. 4, pp. 1271–1275, Apr. 2010.

[46] K. F. Mak, C. Lee, J. Hone, J. Shan, and T. F. Heinz, "Atomically thin MoS_2: A new direct-gap semiconductor," *Phys. Rev. Lett.*, vol. 105, no. 13, p. 136805, Sep. 2010.

[47] E. S. Kadantsev and P. Hawrylak, "Electronic structure of a single MoS_2 monolayer," *Solid State Commun.*, vol. 152, no. 10, pp. 909–913, 2012.

[48] J. Qi, X. Li, X. Qian, and J. Feng, "Bandgap engineering of rippled MoS_2 monolayer under external electric field," *Appl. Phys. Lett.*, vol. 102, no. 17, 2013.

[49] H. Rostami, A. G. Moghaddam, and R. Asgari, "Effective lattice Hamiltonian for monolayer MoS_2: Tailoring electronic structure with perpendicular electric and magnetic fields," *Phys. Rev. B - Condens. Matter Mater. Phys.*, vol. 88, no. 8, pp. 1–8, 2013.

[50] Q. Liu, L. Li, Y. Li, Z. Gao, Z. Chen, and J. Lu, "Tuning electronic structure of bilayer MoS_2 by vertical electric field: A first-principles investigation," *J. Phys. Chem. C*, vol. 116, no. 40, pp. 21556–21562, 2012.

[51] I. Kaplan-Ashiri *et al.*, "On the mechanical behavior of WS_2 nanotubes under axial tension and compression," *Proc. Natl. Acad. Sci. U. S. A.*, vol. 103, no. 3, pp. 523–528, 2006.

[52] M. Ghorbani-Asl, S. Borini, A. Kuc, and T. Heine, "Strain-dependent modulation of conductivity in single-layer transition-metal dichalcogenides," *Phys. Rev. B - Condens. Matter Mater. Phys.*, vol. 87, no. 23, pp. 1–6, 2013.

[53] S. Tongay *et al.*, "Defects activated photoluminescence in two-dimensional semiconductors: interplay between bound, charged, and free excitons," *Sci. Rep.*, vol. 3, p. 2657, 2013.

[54] M. Ghorbani-Asl, A. N. Enyashin, A. Kuc, G. Seifert, and T. Heine, "Defect-induced conductivity anisotropy in MoS_2 monolayers," *Phys. Rev. B - Condens. Matter Mater. Phys.*, vol. 88, no. 24, pp. 1–7, 2013.

[55] H. Qiu *et al.*, "Hopping transport through defect-induced localized states in molybdenum disulphide," *Nat. Commun.*, vol. 4, p. 2642, 2013.

[56] T. Cheiwchanchamnangij and W. R. L. Lambrecht, "Quasiparticle band structure calculation of monolayer, bilayer, and bulk MoS_2," *Phys. Rev. B*, vol. 85, no. 20, p. 205302, May 2012.

[57] A. R. Klots *et al.*, "Probing excitonic states in suspended two-dimensional semiconductors by photocurrent spectroscopy," *Sci. Rep.*, vol. 4, no. 1, p. 6608, 2015.

[58] H. P. Komsa and A. V. Krasheninnikov, "Effects of confinement and environment on the electronic structure and exciton binding energy of MoS_2 from first principles," *Phys. Rev. B - Condens. Matter Mater. Phys.*, vol. 86, no. 24, pp. 1–6, 2012.

[59] D. Y. Qiu, F. H. Da Jornada, and S. G. Louie, "Optical spectrum of MoS_2: Many-body effects and diversity of exciton states," *Phys. Rev. Lett.*, vol. 111, no. 21, pp. 1–5, 2013.

[60] A. Ramasubramaniam, "Large excitonic effects in monolayers of molybdenum and tungsten dichalcogenides," *Phys. Rev. B - Condens. Matter Mater. Phys.*, vol. 86, no. 11, pp. 1–6, 2012.

[61] H. Shi, H. Pan, Y. W. Zhang, and B. I. Yakobson, "Quasiparticle band structures and optical properties of strained monolayer MoS_2 and WS_2," *Phys. Rev. B - Condens. Matter Mater. Phys.*, vol. 87, no. 15, pp. 1–8, 2013.

[62] S. Cahangirov, M. Topsakal, E. Aktürk, H. Šahin, and S. Ciraci, "Two- and one-dimensional honeycomb structures of silicon and germanium," *Phys. Rev. Lett.*, vol. 102, no. 23, pp. 1–4, 2009.

[63] P. De Padova *et al.*, "Evidence of graphene-like electronic signature in silicene nanoribbons," *Appl. Phys. Lett.*, vol. 96, no. 26, pp. 1–4, 2010.

[64] C. C. Liu, H. Jiang, and Y. Yao, "Low-energy effective Hamiltonian involving spin-orbit coupling in silicene and two-dimensional germanium and tin," *Phys. Rev. B - Condens. Matter Mater. Phys.*, vol. 84, no. 19, pp. 1–11, 2011.

[65] M. Houssa, G. Pourtois, V. V. Afanas'Ev, and A. Stesmans, "Electronic properties of two-dimensional hexagonal germanium," *Appl. Phys. Lett.*, vol. 96, no. 8, pp. 1–4, 2010.

[66] S. Lebègue and O. Eriksson, "Electronic structure of two-dimensional crystals from ab initio theory," *Phys. Rev. B*, vol. 79, no. 11, p. 115409, 2009.

[67] E. Bianco, S. Butler, S. Jiang, O. D. Restrepo, W. Windl, and J. E. Goldberger, "Stability and exfoliation of germanane: A germanium graphane analogue," *ACS Nano*, vol. 7, no. 5, pp. 4414–4421, 2013.

[68] B. N. Madhushankar *et al.*, "Electronic properties of germanane field-effect transistors," *2D Mater.*, vol. 4, no. 2, 2017.

[69] P. Miró, M. Audiffred, and T. Heine, "An atlas of two-dimensional materials," *Chem. Soc. Rev.*, vol. 43, no. 18, pp. 6537–6554, 2014.

[70] F. F. Zhu *et al.*, "Epitaxial growth of two-dimensional stanene," *Nat. Mater.*, vol. 14, no. 10, pp. 1020–1025, 2015.

[71] L. Matthes and F. Bechstedt, "Influence of edge and field effects on topological states of germanene nanoribbons from self-consistent calculations," *Phys. Rev. B - Condens. Matter Mater. Phys.*, vol. 90, no. 16, pp. 1–7, 2014.

[72] Z. Ni *et al.*, "Tunable bandgap in silicene and germanene," *Nano Lett.*, vol. 12, no. 1, pp. 113–118, 2012.

[73] G. Gaddemane, W. G. Vandenberghe, and M. V. Fischetti, "Theoretical study of electron transport in silicene and germanene using full-band Monte Carlo simulations," *Int. Conf. Simul. Semicond. Process. Devices, SISPAD*, vol. 1, no. 2, pp. 353–356, 2016.

[74] L. Li *et al.*, "Black phosphorus field-effect transistors," *Nat. Nanotechnol.*, vol. 9, no. 5, pp. 372–377, 2014.

[75] A. Carvalho, M. Wang, X. Zhu, A. S. Rodin, H. Su, and A. H. Castro Neto, "Phosphorene: from theory to applications," *Nat. Rev. Mater.*, vol. 1, p. 16061, 2016.

[76] L. Pauling and M. Simonetta, "Bond Orbitals and Bond Energy in Elementary Phosphorus," *J. Chem. Phys.*, vol. 20, no. 1, p. 29, 1952.

[77] R. R. Hart, M. B. Robin, and N. A. Kuebler, "3p Orbitals, Bent Bonds, and the Electronic

Spectrum of the P4 Molecule," *J. Chem. Phys.*, vol. 42, no. 10, p. 3631, 1965.

[78] F. Hulliger, "Structural Chemistry of Layer-Type Phases," *Phys. Chem. Mater. with Layer. Struct.*, vol. 5, no. 0, p. 392, 1976.

[79] L. Cartz, S. R. Srinivasa, R. J. Riedner, J. D. Jorgensen, and T. G. Worlton, "Effect of pressure on bonding in black phosphorus," *J. Chem. Phys.*, vol. 71, no. 1979, p. 1718, 1979.

[80] A. S. Rodin, A. Carvalho, and A. H. Castro Neto, "Strain-induced gap modification in black phosphorus," *Phys. Rev. Lett.*, vol. 112, no. 17, pp. 1–5, 2014.

[81] J. Qiao, X. Kong, Z.-X. Hu, F. Yang, and W. Ji, "High-mobility transport anisotropy and linear dichroism in few-layer black phosphorus," *Nat. Commun.*, vol. 5, p. 4475, 2014.

[82] V. Tran, R. Soklaski, Y. Liang, and L. Yang, "Layer-controlled band gap and anisotropic excitons in few-layer black phosphorus," *Phys. Rev. B - Condens. Matter Mater. Phys.*, vol. 89, no. 23, pp. 1–6, 2014.

[83] Y. Liu, X. Duan, Y. Huang, and X. Duan, "Two-dimensional transistors beyond graphene and TMDCs," *Chem. Soc. Rev.*, vol. 47, no. 16, pp. 6388–6409, 2018.

[84] D. A. Bandurin *et al.*, "High electron mobility, quantum Hall effect and anomalous optical response in atomically thin InSe," *Nat. Nanotechnol.*, vol. 12, no. 3, pp. 223–227, 2017.

[85] S. Zhang *et al.*, "Two-dimensional GeS with tunable electronic properties via external electric field and strain," *Nanotechnology*, vol. 27, no. 27, 2016.

[86] Z. Q. Fan, X. W. Jiang, Z. Wei, J. W. Luo, and S. S. Li, "Tunable Electronic Structures of GeSe Nanosheets and Nanoribbons," *J. Phys. Chem. C*, vol. 121, no. 26, pp. 14373–14379, 2017.

[87] C. S. Jung *et al.*, "Red-to-Ultraviolet Emission Tuning of Two-Dimensional Gallium Sulfide/Selenide," *ACS Nano*, vol. 9, no. 10, pp. 9585–9593, 2015.

[88] X. Yuan *et al.*, "Wafer-scale arrayed p-n junctions based on few-layer epitaxial GaTe," *Nano Res.*, vol. 8, no. 10, pp. 3332–3341, 2015.

[89] V. Zólyomi, N. D. Drummond, and V. I. Fal'Ko, "Band structure and optical transitions in atomic layers of hexagonal gallium chalcogenides," *Phys. Rev. B - Condens. Matter Mater. Phys.*, vol. 87, no. 19, pp. 1–6, 2013.

[90] D. J. Late *et al.*, "GaS and GaSe ultrathin layer transistors," *Adv. Mater.*, vol. 24, no. 26, pp. 3549–3554, 2012.

[91] P. Hu, Z. Wen, L. Wang, P. Tan, and K. Xiao, "Synthesis of few-layer GaSe nanosheets for high performance photodetectors," *ACS Nano*, vol. 6, no. 7, pp. 5988–5994, 2012.

[92] I. S. Devised *et al.*, "International technology roadmap for semiconductors - 2005 (ITRS-2005). [Online]. Available: http://public.itrs.net/Common/2005/," 2005. .

[93] A. Kuc *et al.*, "High-Performance 2D p-Type Transistors Based on GaSe Layers: An Ab Initio Study," *Adv. Electron. Mater.*, vol. 3, no. 2, pp. 3–7, 2017.

[94] F. Wei, Z. Wei, G. Feng, and H. PingAn, "Atomically thin InSe: A high mobility two-dimensional material," *Sci. China*, vol. 60, no. 7, pp. 1121–1122, 2017.

[95] S. Sucharitakul *et al.*, "Intrinsic Electron Mobility Exceeding 10^3 $cm^2/(V\ s)$ in Multilayer InSe FETs," *Nano Lett.*, vol. 15, no. 6, pp. 3815–3819, 2015.

[96] W. Feng, W. Zheng, W. Cao, and P. Hu, "Back Gated Multilayer InSe Transistors with Enhanced Carrier Mobilities via the Suppression of Carrier Scattering from a Dielectric Interface," *Adv. Mater.*, vol. 26, no. 38, pp. 6587–6593, 2014.

[97] X. Cui *et al.*, "Multi-terminal transport measurements of MoS_2 using a van der Waals heterostructure device platform," *Nat. Nanotechnol.*, vol. 10, no. 6, pp. 534–540, 2015.

[98] L. Li *et al.*, "Quantum Hall effect in black phosphorus two-dimensional electron system," *Nat. Nanotechnol.*, vol. 11, no. 7, pp. 593–597, 2016.

[99] L. Huang, Z. Chen, and J. Li, "Effects of strain on the band gap and effective mass in two-dimensional monolayer GaX (X = S, Se, Te)," *RSC Adv.*, vol. 5, no. 8, pp. 5788–5794, 2015.

[100] L. Debbichi, O. Eriksson, and S. Lebègue, "Two-Dimensional Indium Selenides Compounds: An Ab Initio Study," *J. Phys. Chem. Lett.*, vol. 6, no. 15, pp. 3098–3103, 2015.

[101] E. G. Marin, D. Marian, G. Iannaccone, and G. Fiori, "First-principles simulations of FETs based on two-dimensional InSe," *IEEE Electron Device Lett.*, vol. 3106, no. c, pp. 1–4, 2018.

[102] Y. Ahn and M. Shin, "First-Principles-Based Quantum Transport Simulations of Monolayer Indium Selenide FETs in the Ballistic Limit," *IEEE Trans. Electron Devices*, vol. 64, no. 5, pp. 2129–2134, 2017.

[103] G. Giovannetti, P. A. Khomyakov, G. Brocks, P. J. Kelly, and J. Van Den Brink, "Substrate-induced band gap in graphene on hexagonal boron nitride: Ab initio density functional calculations," *Phys. Rev. B - Condens. Matter Mater. Phys.*, vol. 76, no. 7, pp. 2–5, 2007.

[104] C. R. Dean *et al.*, "Boron nitride substrates for high-quality graphene electronics," *Nat. Nanotechnol.*, vol. 5, no. 10, pp. 722–726, 2010.

[105] L. Wang *et al.*, "One-dimensional electrical contact to a two-dimensional material," *Science*, vol. 342, no. 6158, pp. 614–617, Nov. 2013.

[106] S. Das, R. Gulotty, A. V. Sumant, and A. Roelofs, "All two-dimensional, flexible, transparent, and thinnest thin film transistor," *Nano Lett.*, vol. 14, no. 5, pp. 2861–2866, 2014.

[107] Q. Ouyang *et al.*, "Two-Dimensional Transition Metal Dichalcogenide Enhanced Phase-Sensitive Plasmonic Biosensors: Theoretical Insight," *J. Phys. Chem. C*, vol. 121, pp. 6282–6289, 2017.

[108] D. Akinwande, N. Petrone, and J. Hone, "Two-dimensional flexible nanoelectronics," *Nat. Commun.*, vol. 5, p. 5678, 2014.

[109] F. Ahmed *et al.*, "High Electric Field Carrier Transport and Power Dissipation in Multilayer Black Phosphorus Field Effect Transistor with Dielectric Engineering," *Adv. Funct. Mater.*, vol. 27, no. 4, pp. 1–9, 2017.

[110] D. S. Tsai *et al.*, "Trilayered MoS_2 metal -Semiconductor-metal photodetectors: Photogain and radiation resistance," *IEEE J. Sel. Top. Quantum Electron.*, vol. 20, no. 1, 2014.

[111] D. S. Tsai *et al.*, "Few-layer MoS_2 with high broadband photogain and fast optical switching for use in harsh environments," *ACS Nano*, vol. 7, no. 5, pp. 3905–3911, 2013.

[112] Y. Ye *et al.*, "Exciton-related electroluminescence from monolayer MoS_2," *arXiv:1305.4235*, p. 12, 2013.

[113] M. R. Esmaeili-Rad and S. Salahuddin, "High performance molybdenum disulfide amorphous silicon heterojunction photodetector," *Sci. Rep.*, vol. 3, p. 2345, 2013.

[114] D. Jariwala *et al.*, "Gate-tunable carbon nanotube-MoS_2 heterojunction p-n diode," *Proc. Natl. Acad. Sci.*, vol. 110, no. 45, pp. 18076–18080, 2013.

[115] M. Bernardi, M. Palummo, and J. C. Grossman, "Extraordinary Sunlight Absorption and One

Nanometer Thick Photovoltaics Using Two-Dimensional Monolayer Materials," *Nano Lett.*, vol. 13, pp. 3664–3670, 2013.

[116] M. Fontana *et al.*, "Electron-hole transport and photovoltaic effect in gated MoS_2 Schottky junctions," *Sci. Rep.*, vol. 3, p. 1634, 2013.

[117] A. Pospischil, M. M. Furchi, and T. Mueller, "Solar-energy conversion and light emission in an atomic monolayer p-n diode.," *Nat. Nanotechnol.*, vol. 9, no. 4, pp. 257–61, 2014.

[118] W. J. Yu *et al.*, "Highly efficient gate-tunable photocurrent generation in vertical heterostructures of layered materials," *Nat. Nanotechnol.*, vol. 8, no. 12, pp. 952–958, 2013.

[119] D. Jariwala, V. Sangwan, and L. Lauhon, "Emerging device applications for semiconducting two-dimensional transition metal dichalcogenides," *ACS Nano*, vol. 8, no. 2, pp. 1102–1120, 2014.

[120] R. S. Sundaram *et al.*, "Electroluminescence in Single Layer MoS_2," *Nano Lett.*, vol. 13, no. 4, pp. 1416–1421, 2013.

[121] J. S. Ross *et al.*, "Electrically tunable excitonic light-emitting diodes based on monolayer WSe_2 p-n junctions.," *Nat. Nanotechnol.*, vol. 9, no. 4, pp. 268–72, 2014.

[122] R. Fivaz and E. Mooser, "Mobility of charge carriers in semiconducting layer structures," *Phys. Rev.*, vol. 163, no. 3, pp. 743–755, 1967.

[123] a J. Grant, T. M. Griffiths, G. D. Pitt, and a D. Yoffe, "The electrical properties and the magnitude of the indirect gap in the semiconducting transition metal dichalcogenide layer crystals," *J. Phys. C Solid State Phys.*, vol. 8, no. 1, pp. L17–L23, 1975.

[124] V. Podzorov, M. E. Gershenson, C. Kloc, R. Zeis, and E. Bucher, "High-mobility field-effect transistors based on transition metal dichalcogenides," *Appl. Phys. Lett.*, vol. 84, no. 17, pp. 3301–3303, 2004.

[125] D. Jena and A. Konar, "Enhancement of carrier mobility in semiconductor nanostructures by dielectric engineering," *Phys. Rev. Lett.*, vol. 98, no. 13, p. 136805, 2007.

[126] A. Konar, T. Fang, and D. Jena, "Effect of high-k gate dielectrics on charge transport in graphene-based field effect transistors," *Phys. Rev. B - Condens. Matter Mater. Phys.*, vol. 82, no. 11, pp. 1–7, 2010.

[127] A. K. M. K. M. Newaz, Y. S. Puzyrev, B. Wang, S. T. Pantelides, and K. I. Bolotin, "Probing charge scattering mechanisms in suspended graphene by varying its dielectric environment," *Nat. Commun.*, vol. 3, p. 734, 2012.

[128] H. Fang, S. Chuang, T. C. Chang, K. Takei, T. Takahashi, and A. Javey, "High-performance single layered WSe_2 p-FETs with chemically doped contacts," *Nano Lett.*, vol. 12, no. 7, pp. 3788–3792, 2012.

[129] H. Liu, A. T. Neal, and P. D. Ye, "Channel length scaling of MoS_2 MOSFETs," *ACS Nano*, vol. 6, no. 10, pp. 8563–8569, Oct. 2012.

[130] S. Kim *et al.*, "High-mobility and low-power thin-film transistors based on multilayer MoS_2 crystals," *Nat. Commun.*, vol. 3, no. 1011, Jan. 2012.

[131] L. Liu, S. B. Kumar, Y. Ouyang, and J. Guo, "Performance limits of monolayer transition metal dichalcogenide transistors," *IEEE Trans. Electron Devices*, vol. 58, no. 9, pp. 3042–3047, Sep. 2011.

[132] Y. Yoon, K. Ganapathi, and S. Salahuddin, "How good can monolayer MoS_2 transistors be?," *Nano Lett.*, vol. 11, no. 9, pp. 3768–3773, Sep. 2011.

[133] L. Liu, Y. Lu, and J. Guo, "On Monolayer MoS_2 Field-Effect Transistors at the Scaling Limit," *IEEE Trans. Electron Devices*, vol. 60, no. 12, pp. 4133–4139, 2013.

[134] M. Buscema *et al.*, "Photocurrent generation with two-dimensional van der Waals semiconductors," *Chem. Soc. Rev.*, vol. 44, no. 11, pp. 3691–3718, 2015.

[135] Z. Yin *et al.*, "Single-Layer MoS_2 Phototransistors," *ACS Nano*, vol. 6, no. 1, pp. 74–80, 2012.

[136] W. Choi *et al.*, "High-Detectivity Multilayer MoS_2 Phototransistors with Spectral Response from Ultraviolet to Infrared," *Adv. Mater.*, vol. 24, no. 43, pp. 5832–5836, Nov. 2012.

[137] H. S. Lee *et al.*, "MoS_2 nanosheet phototransistors with thickness-modulated optical energy gap," *Nano Lett.*, vol. 12, no. 7, pp. 3695–3700, 2012.

[138] N. Perea-Lõpez *et al.*, "Photosensor device based on few-layered WS_2 films," *Adv. Funct. Mater.*, vol. 23, no. 44, pp. 5511–5517, 2013.

[139] J. Lin, H. Li, H. Zhang, and W. Chen, "Plasmonic enhancement of photocurrent in MoS_2 field-effect-transistor," *Appl. Phys. Lett.*, vol. 102, no. 20, p. 203109, 2013.

[140] M. Buscema, M. Barkelid, V. Zwiller, H. S. J. Van Der Zant, G. A. Steele, and A. Castellanos-Gomez, "Large and tunable photothermoelectric effect in single-layer MoS_2," *Nano Lett.*, vol. 13, no. 2, pp. 358–363, 2013.

[141] C. C. Wu, D. Jariwala, V. K. Sangwan, T. J. Marks, M. C. Hersam, and L. J. Lauhon, "Elucidating the photoresponse of ultrathin MoS_2 field-effect transistors by scanning photocurrent microscopy," *J. Phys. Chem. Lett.*, vol. 4, no. 15, pp. 2508–2513, 2013.

[142] O. Lopez-Sanchez, D. Lembke, M. Kayci, A. Radenovic, and A. Kis, "Ultrasensitive photodetectors based on monolayer MoS_2," *Nat. Nanotechnol.*, vol. 8, no. 7, pp. 497–501, 2013.

[143] K. Roy *et al.*, "Graphene-MoS_2 hybrid structures for multifunctional photoresponsive memory devices," *Nat. Nanotechnol.*, vol. 8, no. 11, pp. 826–830, 2013.

[144] W. Zhang *et al.*, "Ultrahigh-gain photodetectors based on atomically thin graphene-MoS_2 heterostructures," *Sci. Rep.*, vol. 4, p. 3826, 2014.

[145] D. Sarkar, W. Liu, X. Xie, A. C. Anselmo, S. Mitragotri, and K. Banerjee, "MoS_2 field-effect transistor for next-generation label-free biosensors," *ACS Nano*, vol. 8, no. 4, pp. 3992–4003, 2014.

[146] M. J. Deen, M. W. Shinwari, J. C. Ranuárez, and D. Landheer, "Noise considerations in field-effect biosensors," *J. Appl. Phys.*, vol. 100, no. 7, 2006.

[147] H. Park *et al.*, "Label-Free and Recalibrated Multilayer MoS_2 Biosensor for Point-of-Care Diagnostics," *ACS Appl. Mater. Interfaces*, vol. 9, no. 50, pp. 43490–43497, 2017.

[148] J. Wang, "Device physics and simulation of silicon nanowire transistors," Purdue University, 2005.

[149] M. Lundstrom, *Fundamentals of Carrier Transport*. 2000.

[150] F. Assad, Z. Ren, D. Vasileska, S. Datta, and M. Lundstrom, "On the performance limits for Si MOSFET's: A theoretical study," *IEEE Trans. Electron Devices*, vol. 47, no. 1, pp. 232–240, 2000.

[151] Z. Ren, "Simulation of nanoscale MOSFETs: a scattering theory interpretation," *Superlattices Microstruct.*, vol. 27, no. 2–3, pp. 177–189, 2000.

[152] K. Banoo, J. H. Rhew, M. Lundstrom, C. W. Shu, and J. W. Jerome, "Simulating quasi-ballistic transport in Si nanotransistors," *Vlsi Des.*, vol. 13, no. 1–4, pp. 5–13, 2001.

[153] C. R. Huster, "TWO-DIMENSIONAL SCATTERING MATRIX SIMULATIONS OF SI MOSFETS," Purdue University, 2000.

[154] K. Banoo, "Direct Solution of the Boltzmann Transport Equation in Nanoscale Si Devices," Purdue University, 2000.

[155] D. Vasileska, S. M. Goodnick, and G. Klimeck, *Computational electronics: Semiclassical and quantum device modeling and simulation*. 2017.

[156] "The drift diffusion equation and its application in MOSFET modelling," *Math. Comput. Simul.*, vol. 34, no. 1, p. 87, 1992.

[157] M. G. Ancona, "Electron transport in graphene from a diffusion-drift perspective," *IEEE Trans. Electron Devices*, vol. 57, no. 3, pp. 681–689, 2010.

[158] A. Paussa, M. Geromel, P. Palestri, M. Bresciani, D. Esseni, and L. Selmi, "Simulation of graphene nanoscale RF transistors including scattering and generation/recombination mechanisms," in *Technical Digest - International Electron Devices Meeting, IEDM*, 2011.

[159] A. Y. Serov, Z. Y. Ong, M. V. Fischetti, and E. Pop, "Theoretical analysis of high-field transport in graphene on a substrate," *J. Appl. Phys.*, vol. 116, no. 3, 2014.

[160] M. P. Anantram, M. S. Lundstrom, and D. E. Nikonov, "Modeling of Nanoscale Devices," *Proc. IEEE*, vol. 96, no. 9, pp. 1511–1550, 2008.

[161] R. Venugopal, "Modeling quantum transport in nanoscale transistors," Purdue University, 2003.

[162] S. Datta, "Electrical resistance: an atomistic view," vol. 433, 2004.

[163] Jing Guo, D. Supriyo, L. Mark, and A. M. Guo, "Towards Multi-Scale Modeling of Carbon Nanotube Transistors," pp. 1–41, 2006.

[164] S. Datta, "Nanoscale device modeling: the Green's function method," *Superlattices Microstruct.*, vol. 28, no. 4, pp. 253–278, Oct. 2000.

[165] Z. Ren, "Nanoscale MOSFETs: physics, simulation and design," Purdue University, 2001.

[166] S. Datta, *Quantum Transport: Atom to Transistor*. Cambridge University Press, 2005.

[167] Z. Ren, R. Venugopal, S. Goasguen, S. Datta, and M. S. Lundstrom, "nanoMOS 2.5: A two-dimensional simulator for quantum transport in double-gate MOSFETs," *IEEE Trans. Electron Devices*, vol. 50, no. 9, pp. 1914–1925, 2003.

[168] A. Rahman, A. Ghosh, and M. Lundstrom, "Assessment of n-MOSFETs by quantum simulation," *IEEE Int. Electron Devices Meet. 2003. IEDM '03 Tech. Dig.*, pp. 19.4.1-19.4.4, 2003.

[169] G. Bin Liu, W. Y. Shan, Y. Yao, W. Yao, and D. Xiao, "Three-band tight-binding model for monolayers of group VIB-transition metal dichalcogenides," *Phys. Rev. B*, vol. 88, no. 8, p. 085433, 2013.

[170] R. Venugopal, Z. Ren, S. Datta, M. S. Lundstrom, and D. Jovanovic, "Simulating quantum transport in nanoscale transistors: Real versus mode-space approaches," *J. Appl. Phys.*, vol. 92, no. 7, pp. 3730–3739, 2002.

[171] T. Ando, A. B. Fowler, and F. Stern, "Electronic properties of two-dimensional systems," *Rev. Mod. Phys.*, vol. 54, no. 2, pp. 437–672, 1982.

[172] James R. Nagel, "Solving the generalized poisson equation using the finite-difference method (FDM)," 2012.

[173] T. Roy *et al.*, "Field-Effect Transistors Built from All Two-Dimensional Material Components," *ACS Nano*, no. 6, pp. 6259–6264, 2014.

[174] J. Kwon *et al.*, "Giant photoamplification in indirect-bandgap multilayer MoS_2 phototransistors with local bottom-gate structures," *Adv. Mater.*, vol. 27, no. 13, pp. 2224–2230, 2015.

[175] K. Natori, "Ballistic metal-oxide-semiconductor field effect transistor," *J. Appl. Phys.*, vol. 76, no. 8, pp. 4879–4890, 1994.

[176] X. Gong *et al.*, "High-Detectivity Polymer Photodetectors with Spectral Response from 300 nm to 1450 nm," *Science (80-.).*, vol. 325, no. 5948, pp. 1665–1667, 2009.

[177] H. Kwon *et al.*, "Selective and localized laser annealing effect for high-performance flexible multilayer MoS_2 thin-film transistors," *Nano Res.*, vol. 7, no. 8, pp. 1137–1145, 2014.

[178] S. Wu *et al.*, "Electrical tuning of valley magnetic moment through symmetry control in bilayer MoS_2," *Nat. Phys.*, vol. 9, no. 3, pp. 149–153, 2013.

[179] K. He, C. Poole, K. F. Mak, and J. Shan, "Experimental demonstration of continuous electronic structure tuning via strain in atomically thin MoS_2," *Nano Lett.*, vol. 13, no. 6, pp. 2931–2936, 2013.

[180] Y. Zhan, Z. Liu, S. Najmaei, P. M. Ajayan, and J. Lou, "Large-area vapor-phase growth and characterization of MoS_2 atomic layers on a SiO_2 substrate," *Small*, vol. 8, no. 7, pp. 966–971, 2012.

[181] K.-K. Liu *et al.*, "Growth of large-area and highly crystalline MoS_2 thin layers on insulating substrates," *Nano Lett.*, vol. 12, pp. 1538–1544, 2012.

[182] J. Rhyee *et al.*, "High-Mobility Transistors Based on Large-Area and Highly Crystalline CVD-Grown $MoSe_2$ Films on Insulating Substrates," *Adv. Mater.*, vol. 28, pp. 2316–2321, 2016.

[183] S. Tongay *et al.*, "Thermally Driven Crossover from Indirect toward Direct Bandgap in 2D Semiconductors: $MoSe_2$ versus MoS_2," *Nano Lett.*, vol. 12, no. 11, pp. 5576–5580, 2012.

[184] S. Larentis, B. Fallahazad, and E. Tutuc, "Field-effect transistors and intrinsic mobility in ultra-thin $MoSe_2$ layers," *Appl. Phys. Lett.*, vol. 101, no. 22, 2012.

[185] X. Wang *et al.*, "Chemical vapor deposition growth of crystalline monolayer $MoSe_2$," *ACS Nano*, vol. 8, no. 5, pp. 5125–5131, 2014.

[186] S. Das, H.-Y. Chen, A. V. Penumatcha, and J. Appenzeller, "High performance multilayer MoS_2 transistors with scandium contacts," *Nano Lett.*, vol. 13, no. 1, pp. 100–105, Jan. 2013.

[187] S. McDonnell, R. Addou, C. Buie, R. M. Wallace, and C. L. Hinkle, "Defect-dominated doping and contact resistance in MoS_2," *ACS Nano*, vol. 8, no. 3, pp. 2880–2888, Mar. 2014.

[188] C. Chen, K. Abe, H. Kumomi, and J. Kanicki, "Density of States of a-InGaZnO From Temperature-Dependent Field-Effect Studies," *IEEE Trans. Electron Devices*, vol. 56, no. 6, pp. 1177–1183, 2009.

[189] Y. Lee, J. Lee, S. Kim, and H. S. Park, "Rendering high charge density of states in ionic liquid-gated MoS_2 transistors," *J. Phys. Chem. C*, vol. 118, no. 31, pp. 18278–18282, 2014.

[190] W. S. Yun, S. W. Han, S. C. Hong, I. G. Kim, and J. D. Lee, "Thickness and strain effects on electronic structures of transition metal dichalcogenides: 2H-MX_2 semiconductors (M = Mo, W; X = S, Se, Te)," *Phys. Rev. B - Condens. Matter Mater. Phys.*, vol. 85, no. 3, 2012.

[191] R. Scheer and H. W. Schock, *Chalcogenide Photovoltaics: Physics, Technologies, and Thin Film Devices*. 2011.

[192] J. Bardeen, "Surface states and rectification at a metal semi-conductor contact," *Phys. Rev.*, vol. 71, no. 10, pp. 717–727, 1947.

[193] J. Xia *et al.*, "CVD synthesis of large-area, highly crystalline $MoSe_2$ atomic layers on diverse substrates and application to photodetectors," *Nanoscale*, vol. 6, no. 15, pp. 8949–8955, 2014.

[194] a Abderrahmane, P. J. Ko, T. V Thu, S. Ishizawa, T. Takamura, and A. Sandhu, "High photosensitivity few-layered $MoSe_2$ back-gated field-effect phototransistors," *Nanotechnology*, vol. 25, no. 36, p. 365202, 2014.

[195] C. Fan, Q. Yue, J. Yang, Z. Wei, S. Yang, and J. Li, "Low temperature electrical and photo-responsive properties of $MoSe_2$," *Appl. Phys. Lett.*, vol. 104, no. 20, 2014.

[196] M. Furchi, D. Polyushkin, A. Pospischil, and T. Mueller, "Mechanisms of Photoconductivity in Atomically Thin MoS_2," *Nano Lett.*, vol. 14, no. 11, pp. 6165–6170, 2014.

[197] Y. Takanashi, K. Takahata, and Y. Muramoto, "Characteristics of InAlAs / InGaAs High Electron Mobility Transistors Under 1.3-μm Laser Illumination," *IEEE Electron Device Lett.*, vol. 19, no. 12, pp. 472–474, 1998.

[198] J. A. Hornbeck and J. R. Haynes, "Trapping of Minority Carriers in Silicon, I. p-Type Silicon," *Phys. Rev.*, vol. 97, no. 2, pp. 311–321, 1955.

[199] H. Y. Fan, "Effect of Traps on carrier Injection in semiconductors," *Phys. Rev.*, vol. 92, no. 6, p. 1424, 1953.

[200] D. Macdonald and A. Cuevas, "Trapping of minority carriers in multicrystalline silicon," *Appl. Phys. Lett.*, vol. 74, no. 12, p. 1710, 1999.

[201] C. Y. Chen, "Theory of a modulated barrier photodiode," *Appl. Phys. Lett.*, vol. 39, no. 12, pp. 979–981, 1981.

[202] U. Ahuja, R. Joshi, D. C. Kothari, H. Tiwari, and K. Venugopalan, "Optical response of mixed molybdenum dichalcogenides for solar cell applications using the modified becke-johnson potential," *Zeitschrift fur Naturforsch. - Sect. A J. Phys. Sci.*, vol. 71, no. 3, pp. 213–224, 2016.

[203] W. Chen *et al.*, "Scaling Analysis of High Gain Monolayer MoS_2 Photodetector for Its Performance Optimization," *IEEE Trans. Electron Devices*, vol. 63, no. 4, pp. 1608–1614, 2016.

[204] G. Cao, Y. An, Q. Bao, and X. Li, "Physics and Optoelectronic Simulation of Photodetectors Based on 2D Materials," *Adv. Opt. Mater.*, vol. 1900410, pp. 1–13, 2019.

[205] S. Kim *et al.*, "Interstitial Mo-Assisted Photovoltaic Effect in Multilayer $MoSe_2$ Phototransistors," *Adv. Mater.*, vol. 30, p. 1705542, 2018.

[206] M. Visciarelli, E. Gnani, A. Gnudi, S. Reggiani, and G. Baccarani, "Impact of Traps and Strain on Optimized n- and p-Type TFETs Integrated on the Same InAs/AlGaSb Technology Platform," *IEEE Trans. Electron Devices*, vol. 64, no. 8, pp. 3108–3113, 2017.

[207] C. S. S. Sangeeth, P. Stadler, S. Schaur, N. S. Sariciftci, and R. Menon, "Interfaces and traps in petacene field-effect transistor," *J. Appl. Phys.*, vol. 108, p. 113703, 2010.

[208] J. G. Simmons and G. W. Taylor, "Nonequilibrium Steady-State Statistics and Associated Effects for insulators and S mlconductom Containing an Arbitrary Distribution of Traps," *Phys. Rev. B*, vol. 4, no. 2, 1971.

[209] N. Huo and G. Konstantatos, "Ultrasensitive all-2D MoS_2 phototransistors enabled by an out-of-plane MoS_2 PN homojunction," *Nat. Commun.*, vol. 8, no. 1, p. 572, 2017.

[210] D. Kufer and G. Konstantatos, "Highly Sensitive, Encapsulated MoS_2 Photodetector with Gate Controllable Gain and Speed," *Nano Lett.*, vol. 15, no. 11, pp. 7307–7313, 2015.

[211] A. Crocherie, J. Vaillant, and F. Hirigoyen, "Three-dimensional broadband FDTD optical simulations of CMOS image sensor," *Opt. Des. Eng. III*, vol. 7100, no. September 2008, p. 71002J, 2008.

[212] F. Hirigoyen, A. Crocherie, J. M. Vaillant, and Y. Cazaux, "FDTD-based optical simulations methodology for CMOS image sensors pixels architecture and process optimization," *Sensors, Cameras, Syst. Ind. Appl. IX*, vol. 6816, no. February 2008, p. 681609, 2008.

[213] J. O. Island, S. I. Blanter, M. Buscema, H. S. J. Van Der Zant, and A. Castellanos-Gomez, "Gate controlled photocurrent generation mechanisms in high-gain In_2Se_3 phototransistors," *Nano Lett.*, vol. 15, no. 12, pp. 7853–7858, 2015.

[214] W. Zhang, J. K. Huang, C. H. Chen, Y. H. Chang, Y. J. Cheng, and L. J. Li, "High-Gain

Phototransistors Based on a CVD MoS_2 Monolayer," *Adv. Mater.*, vol. 25, pp. 3456–3461, 2013.

[215] T. Yun *et al.*, "2D Metal Chalcogenide Nanopatterns by Block Copolymer Lithography," *Adv. Funct. Mater.*, vol. 28, no. 50, 2018.

[216] H. Xue *et al.*, "High photoresponsivity and broadband photodetection with a band-engineered $WSe_2/SnSe_2$ heterostructure," *Nanoscale*, vol. 11, no. 7, pp. 3173–3185, 2019.

[217] G. Nazir *et al.*, "Enhanced photoresponse of ZnO quantum dot-decorated MoS_2 thin films," *RSC Adv.*, vol. 7, no. 27, pp. 16890–16900, 2017.

[218] C. Chen *et al.*, "Highly responsive MoS_2 photodetectors enhanced by graphene quantum dots," *Sci. Rep.*, vol. 5, 2015.

[219] S. Qiao *et al.*, "A vertically layered MoS_2/Si heterojunction for an ultrahigh and ultrafast photoresponse photodetector," *J. Mater. Chem. C*, vol. 6, no. 13, pp. 3233–3239, 2018.

[220] T. W. Kim *et al.*, "Structural defects in a nanomesh of bulk MoS_2 using an anodic aluminum oxide template for photoluminescence efficiency enhancement," *Sci. Rep.*, vol. 8, no. 1, 2018.

[221] M. Tinoco, L. Maduro, M. Masaki, E. Okunishi, and S. Conesa-Boj, "Strain-Dependent Edge Structures in MoS_2 Layers," *Nano Lett.*, vol. 17, no. 11, pp. 7021–7026, 2017.

[222] S. Yang, D. Li, T. Zhang, Z. Tao, and J. Chen, "First-principles study of zigzag MoS_2 nanoribbon as a promising cathode material for rechargeable Mg batteries," *J. Phys. Chem. C*, vol. 116, no. 1, pp. 1307–1312, 2012.

[223] S. L. Xiao, W. Z. Yu, and S. P. Gao, "Edge preference and band gap characters of MoS_2 and WS_2 nanoribbons," *Surf. Sci.*, vol. 653, pp. 107–112, 2016.

[224] Y. Li, Z. Zhou, S. Zhang, and Z. Chen, "MoS_2 nanoribbons: High stability and unusual electronic and magnetic properties," *J. Am. Chem. Soc.*, vol. 130, no. 49, pp. 16739–16744, 2008.

[225] H. Zhou *et al.*, "Thickness-dependent patterning of MoS_2 sheets with well-oriented triangular pits by heating in air," *Nano Res.*, vol. 6, no. 10, pp. 703–711, 2013.

[226] S. M. Shinde *et al.*, "Stacking-controllable interlayer coupling and symmetric configuration of multilayered MoS_2," *NPG Asia Mater.*, vol. 10, no. 2, pp. e468–e468, 2018.

[227] L. Shao, G. Chen, H. Ye, Y. Wu, H. Niu, and Y. Zhu, "Theoretical study on electronic properties of MoS_2 antidot lattices," *J. Appl. Phys.*, vol. 116, no. 11, 2014.

[228] V. Subramanian, "Graphite: Technologies and Global Markets," 2017.